Study of the relation between blood flow and the age-dependent localisation of early atherosclerosis

by

Véronique Paule-Alberte Peiffer

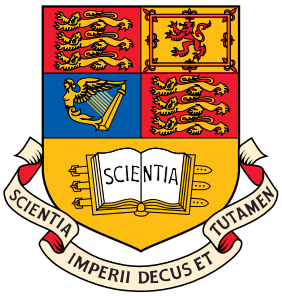

Department of Aeronautics

Imperial College London

South Kensington Campus

London SW7 2AZ

This thesis is submitted for the degree of Doctor of Philosophy of Imperial College London

2012

Declaration

I hereby declare that this submission is my own work and that it contains no material previously published or written by another person, nor material which to a substantial extent has been accepted for the award of any other degree or diploma of the university or other institute of higher learning, except where due acknowledgment has been made in the text.

Véronique Peiffer

Abstract

Atherosclerosis develops non-uniformly within the arterial system and the distribution of lesions has been observed to change with age. This thesis investigates the concept that the patchiness of the disease is related to local variations in blood flow.

Based on the insights from a systematic literature review, a novel study was designed to analyse the relation between haemodynamic factors and age-dependent atherogenesis in the thoracic aorta of rabbits. Arterial geometries were reconstructed by micro-Computed Tomography of vascular corrosion casts, with particular attention to the anatomical accuracy of the dataset. Blood flow was simulated in these geometries using a spectral/*hp* element method. Distributions of traditional shear-related metrics were calculated and both qualitatively and quantitatively compared to maps of lesion prevalence. In addition, a time-averaged transverse wall shear stress was introduced.

A geometric analysis of the dataset of rabbit thoracic aortas revealed a significant change with age in the degree of aortic taper. The geometric changes could explain age-related differences in flow characteristics, in particular in the extent of Dean-type vortical structures into the descending aorta and the strength of a dorsal streak of high shear. The comparative analysis of shear and lesion distributions did not unequivocally support the theory that lesions occur in regions of low shear. The novel haemodynamic metric, in combination with current metrics, enabled an improved identification of zones of multi-directional disturbed flow.

In conclusion, this thesis adds to the understanding of the relation between blood flow and early atherosclerosis, and provides tools for use in future studies.

Acknowledgments

A number of people and institutions have played essential roles in enabling the research presented here. I would like to thank them gratefully for their help and support.

The first words of thanks go to Prof. Spencer Sherwin and Prof. Peter Weinberg, who have been excellent supervisors for me. They have given me the freedom to explore, while at the same time providing me with crucial guidance and advice to work towards a coherent story.

I would like to extend my appreciation to the students, postdocs, research fellows and faculty members from the departments of Aeronautics and Bioengineering who contributed directly to this PhD research by sharing their knowledge and skills. Special thanks go to Dr. Ana Plata and Dr. Peter Vincent (who ensured I could start this project under the best possible conditions and also afterwards took time to discuss my work), Mr. Ethan Rowland and Dr. Anthony Hunt (who spent many days in the lab with me), Dr. Zahra Mohri, Dr. Lindsey Clarke, Mr. Peter Sowinski, Dr. Emma Bailey, Dr. Eleni Bazigou and Miss Julia Shih (who also assisted with the lab work), Dr. Donal Taylor, Dr. Julien Hoessler and Dr. Chris Cantwell (who gave me helpful tips on the computational side), and last but not least Dr. Anil Bharath, Dr. Jordi Alastruey and Prof. Kim Parker (for the insightful discussions).

I thank the Imperial College High Performance Computing Service for use of their computational resources. I would also like to express my sincere gratitude to Dr. Mariano Vázquez for hosting my visit to the Barcelona Computer Center, the HPC-Europa2 Transnational Access Programme for making this visit possible, and Prof. Ian Marshall, Dr. Maurits Jansen and Dr. Patrick Hadoke from the University

of Edinburgh for their collaboration on an exciting project.

It has been a privilege being funded by the British Heart Foundation Centre of Research Excellence at Imperial College London, which is managed by a great team. This has given me the opportunity to broaden my knowledge during a PhD training programme and informal journal clubs. In addition, I would like to acknowledge the financial support from the Imperial College Trust and the Old Centralians' Trust for participation in international conferences.

I have had a great time in London, thanks to the many supportive people around me. In particular, I would like to thank Donal, Cath, Ethan, Chris, Raul and Alister for all the time we spent together in office L57, the Sherwin and Weinberg research groups for the enjoyable lunches and inspiring meetings, Sietse and Eugene for joining me in Hyde Park runs and music rehearsals, Amalia, Eugene and Daria for spontaneous flat dinners and cosy nights-in, and not forgetting Joana, Amalia, Silvia and Barbara for their warm friendship.

Finally, I am indebted to my family and to Moïse. My parents have always encouraged me to do what I like and I greatly appreciate their unwavering love and genuine interest in what I do. Also the numerous FaceTime, Skype and Viber sessions with Moïse have been an indispensable support to me; I could not thank him enough for being there for me.

I dedicate this thesis to my sister and the newborn Richard, my gorgeous godson.

Véronique Peiffer

London, September 2012

Contents

List of Figures

List of Tables

Nomenclature

List of abbreviations

AA	Aortic arch
ApoE-/-	Apolipoprotein E knock-out
BCT	Brachiocephalic trunk
CA	Convective acceleration
CF	Centrifugal force
CFD	Computational fluid dynamics
CFL	Courant-Friedrichs-Lewy condition
Co	Coriolis force
CT	Computed tomography
CVD	Cardiovascular disease
De	Dean number
ICA	Internal carotid artery
IV	Intravenously
IVUS	Intravascular ultrasound
LCCA	Left common carotid artery
LDL	Low-density lipoprotein
Ldlr-/-	LDL receptor knock-out
LSA	Left subclavian artery
LVA	Left vertebral artery
MRI	Magnetic resonance imaging
NZW	New Zealand White

OSI	Oscillatory shear index
PBS	Phosphate buffered saline
PG	Pressure gradient
PVC	Polyvinyl chloride
RCCA	Right common carotid artery
Re	Reynolds number
RRT	Relative residence time
SD	Standard deviation
SEM	Standard error of the mean
TAWSS	Time-averaged wall shear stress
TF	Torsional force
TV	Threshold value
transWSS	Time-averaged transverse WSS
US	Ultrasound
VF	Viscous force
WHO	World Health Organization
Wo	Womersley parameter
WSS	Wall shear stress

List of symbols

α_q, β_q, γ_0	Weights for mixed explicit-implicit integration
Δt	Time step
$\overset{\leftrightarrow}{\delta}$	Unit tensor
$\partial\Omega$	Boundary of the computational domain
θ_B	Circumferential angle measured from **B**
κ	Curvature
μ	Dynamic viscosity
μ_5	Mean of 5 pixel values
ν	Kinematic viscosity

ρ	Blood density
σ_5	Standard deviation of 5 pixel values
τ	Torsion
$\overset{\leftrightarrow}{\tau}$	Stress tensor
$\boldsymbol{\tau}_w$	Wall shear stress vector
Φ_i	Trial or expansion function
ϕ	Angle used in the definition of the Germano coordinate system
ϕ_p^e	Local expansion mode
Ω	Computational domain
$\boldsymbol{\Omega}$	Axis of rotation
Ω^e	Elemental computational domain
$\overset{\leftrightarrow}{\Omega}_{\nabla \mathbf{u}}$	Antisymmetric part of the velocity gradient tensor $\nabla \mathbf{u}$
$\bar{\Omega}_j$	Element constructed from the vertices $\bar{\mathbf{P}}_i^j$ and $\mathbf{P}_i$
ω	Oscillation frequency
ω_s	Axial vorticity

A_0	Cross-sectional area at the aortic root
A_i	Cross-sectional area of branch i in an arterial branching geometry
$\bar{A}_j$	Face area of element $\bar{\Omega}_j$
$\mathbf{B}$	Unit binormal vector of the Germano coordinate system
C	Centre of curvature
$\mathbf{C}_{ijk}$	Centroid
D	Local diameter
D_0	Hydraulic diameter at the aortic root
D_{final}	Cast diameter after resin setting
D_{initial}	Cast diameter before resin setting
d_{peak}	Radial offset of the peak axial velocity
$\mathbb{E}$	Differential problem
$\mathbf{f}$	Body forces
f_{br}	Percentage of the flow going to the branches in an arterial

	branching geometry
f_i^p	Blending function
h	Parameter used in the definition of $\mathbf{\Omega}$
J_e, J_i, J_p	Orders of integration
$\mathbf{K_i^p}$	Orthogonal projection of point $\mathbf{P_i}$ onto the line defined by $\mathbf{P_p}$ and $\mathbf{N^p}$
L	Length
l_{dec}	Decorrelation length
$\mathcal{M}$	Coarse straight-sided surface mesh
$\bar{\mathcal{M}}$	High-definition straight-sided surface mesh
m	Number of rows in a map
$\mathbf{N}$	Unit normal vector of the Germano coordinate system
$\mathbf{N^p}$	Phong normal at point $\mathbf{P_p}$
N_{br}	Number of branches in an arterial branching geometry
N_{dof}	Number of degrees of freedom
N_{el}	Number of elements
$\mathbf{N}_i$	Vertex normal
$\bar{\mathbf{N}}_j$	Face normal of element $\bar{\Omega}_j$
N_{v}	Number of element vertices
n	Number of columns in a map
$\mathbf{n}$	Vector normal to the vessel wall
n_{smp}	Number of random samples
n_{sur}	Number of repetitions of the surrogate data analysis
P	P-value
P_0	Luminal perimeter at the aortic root
$\mathbf{P}_i$	Vertex or point
$\bar{\mathbf{P}}_i^j$	Vertices in $\bar{\mathcal{M}}$ closest to vertex $\mathbf{P}_i$
P_o	Polynomial order
$\mathbf{P_p}$	Arbitrary point in a triangle
$\hat{\mathbf{P}}_\mathbf{p}$	Phong projection of point $\mathbf{P_p}$
p	Pressure

Q	Volume flow rate
$\mathbf{Q}_i^{\mathbf{p}}$	Intersection of S_i and the line defined by $\mathbf{P_p}$ and $\mathbf{N^p}$
R	Residual
$\mathbf{R}$	Location of a cross-section
R_c	Radius of curvature
$\mathrm{Re}_{\mathrm{in}}$	Reynolds number at the aortic inlet
r^2	Coefficient of determination
r_i	Radius of branch i in an arterial branching geometry
r_i^{bar}	Barycentric coordinate
r_{Pears}	Pearson's correlation coefficient
$\overset{\leftrightarrow}{S}$	Rate of strain tensor
$\overset{\leftrightarrow}{S}_{\nabla \mathbf{u}}$	Symmetric part of the velocity gradient tensor $\nabla \mathbf{u}$
S_i	Sphere through point $\mathbf{P_i}$
(s, r, θ)	Axes of the Germano coordinate system
s_{map}	Number of pixels in a map
s_{smp}	Sample size
T	Cardiac cycle period
$\mathbf{T}$	Unit tangent vector of the Germano coordinate system
t	Time
U_{red}	Reduced velocity
u	Unknowns
$\mathbf{u}$	Velocity vector
u^δ	Approximation to unknowns u
u^0	Solution selected to satisfying initial and boundary conditions
u_0	Average inlet flow velocity at the aortic root
u_1	Average speed in branch with radius r_i
$\hat{u}_i$	Unknown coefficient to Φ_i
$\hat{u}_p^e$	Unknown coefficient to ϕ_p^e
v_j	Test or weight function
$\mathrm{WSS}_{s,\mathrm{peak}}$	Maximum axial WSS
(x, y, z)	Axes of the Cartesian coordinate system

$\mathbf{x}$	Spatial position
x_{cnt}	Central pixel value
Z	Sample Z-score

Chapter 1

Introduction

Cardiovascular disease, a collective noun for a number of disorders of the heart and blood vessels, is the number one cause of death globally: an estimated 30 % of all deaths in 2008 were due to cardiovascular disease and it is projected to remain the major killer until at least 2030 (WHO, 2011). In view of reducing the social and economic burden cardiovascular disease presents, the World Health Organization, amongst others, urges for initiatives aimed at prevention and control of the disease. A good understanding of the factors involved in the onset and progression of cardiovascular disease is essential in this light.

Since cardiovascular disease is very often the consequence of an underlying condition called atherosclerosis, this thesis takes the view that the unravelling of atherosclerosis can provide the key to the design of new prevention, diagnosis and treatment strategies for cardiovascular disease. This first chapter provides a general introduction to the topic.

Section 1.1 explains the basic mechanisms involved in atherosclerosis and indicates what aspects of the disease are not yet understood. It will emerge that blood flow is believed to play an important role in the development of atherosclerosis. Section 1.2 therefore introduces the field of haemodynamics. Outstanding issues in the understanding of atherosclerosis will define the research aims of the thesis, which are stated in section 1.3. Finally, in section 1.4 the thesis structure is laid out and the content of each chapter is summarised.

1.1 Atherosclerosis

1.1.1 From atherosclerosis to cardiovascular event

According to the dominant insudation theory, which is schematically illustrated in figure 1.1(a), low-density lipoproteins (LDL) that are circulating within the blood can enter the arterial wall (Anitschkow, 1933; Hansson et al., 2006). The LDL concentration in the intima, which is the interior layer of the arterial wall, increases with increasing plasma concentrations. Within the intima the LDL particles are modified to the inflammatory form oxidised LDL. The presence of oxidised LDL causes endothelial cell[1] activation, a process comprising functional and morphological cell changes including increased expression of leukocyte adhesion molecules (Bijl, 2003). Raised glucose levels, as observed in diabetic patients, enhance this effect (Bui et al., 2009).

Monocytes in particular adhere to the adhesion molecules and subsequently penetrate the endothelial surface guided by chemokinetic stimuli. Once in the intima, the monocytes differentiate into macrophages, take up the available oxidised LDL and mediate the modification of LDL; cholesterol is formed. If the cholesterol production exceeds the cells' export capabilities, macrophages turn into lipid-laden foam cells, resulting in an *initial atherosclerotic lesion*. The cascade of events is illustrated in figure 1.1(b). When one or more layers of foam cells are present, a *fatty streak* has developed. These early lesions do not affect the flow of blood in the artery and are therefore clinically silent (Stary, 1992).

Lesions progress into advanced atheromatous plaques when extracellular lipids, left behind by dying macrophages, pool together into a lipid core. A *fibrotic cap*, composed of smooth muscle cells and collagen, may delineate the region between the lipid core and the endothelial cell layer. Some advanced lesions become mineralised (calcified lesions), while some others consist almost entirely of scar collagen (fibrotic lesions). If the advanced plaque significantly reduces the luminal cross-section, clinical symptoms such as stable or effort angina (for plaques in coronary arteries) can

[1]The endothelium is the collection of cells which line the interior surface of blood vessels.

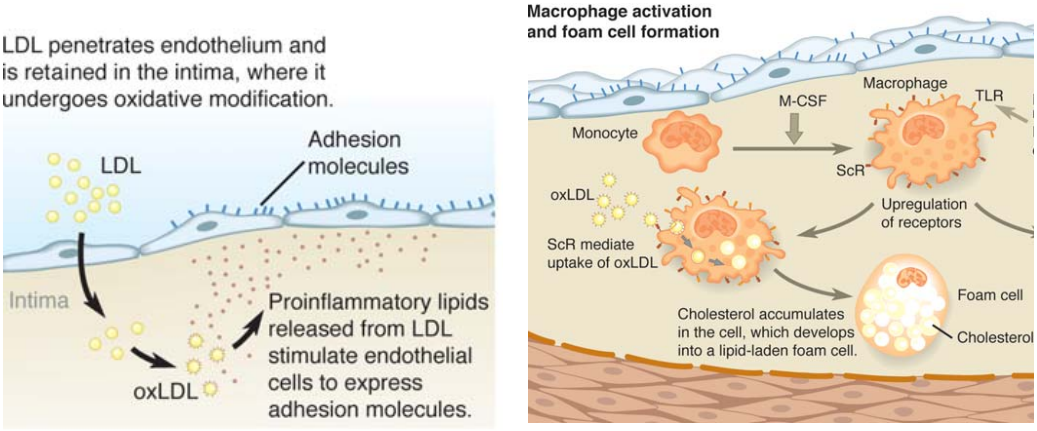

(a) Endothelial activation (b) Macrophage activation

Figure 1.1: The onset of atherosclerosis is characterised by lipid accumulation in the intima. Atherogenesis comprises of endothelial (a) and macrophage activation (b). After Hansson et al. (2006).

occur (Stary, 1992).

When a plaque erodes or fissures, the contents of the lipid core come into contact with the circulating blood, resulting in the formation of a blood clot or thrombus. This thrombotic material can build up over the plaque, or detach to form an embolus. The latter can lead to acute cardiovascular events such as myocardial infarction, if blood supply to the heart is impeded, or stroke, if the brain runs short of blood supply. Since plaques with a large lipid core but only thin fibrotic cap are more prone to rupture, they are referred to as *vulnerable* plaques (Shah, 2009).

1.1.2 Disease with a focal nature

1.1.2.1 Apparent paradox

According to the World Health Organization, the most important behavioural risk factors for cardiovascular disease are an unhealthy diet, physical inactivity, tobacco use and excessive alcohol consumption. Effects of these risk factors may show up in individuals as metabolic risk factors such as hypertension, diabetes mellitus, hypercholesterolaemia and obesity. Other determinants of cardiovascular disease include poverty, stress and family history (WHO, 2011). A common characteristic of the

listed risk factors is their systemic nature: they affect the whole body, implying a uniform effect on the entire vascular system.

This contrasts with the development of atherosclerosis which is non-uniform within the arterial system, as was already noted in the nineteenth century (von Rindfleisch, 1872). The prevalence of atherosclerotic lesions varies both between and within vessels. In particular, lesions develop predominantly in large and medium-sized central arteries, such as the aorta and carotid, vertebral and coronary arteries (Mitchell and Schwartz, 1965). The periphery is much less affected, and veins and the pulmonary circuit are unaffected under normal conditions. Within vessels, the prevalence of lesions varies particularly around branch openings (or *ostia*) and in regions of high curvature (von Rindfleisch, 1872). Detailed lesion maps have been obtained for the most atherosclerosis-prone regions of the human arterial system, including the aorta (Sinzinger et al., 1980; Cornhill et al., 1990; Sloop et al., 1998), carotid bifurcation (Ku et al., 1985) and coronary arteries (Svindland, 1983).

As in humans, atherosclerosis develops non-uniformly within the arterial system of animals. Lesion distributions have been studied in a range of mouse strains (McGillicuddy et al., 2001; Maeda et al., 2007) and in minipigs (Cornhill et al., 1985), but most extensively in rabbits (Cornhill and Roach, 1976; Zeindler et al., 1989; Cremers et al., 2011). Whereas in human studies of disease localisation the most atherosclerosis-prone regions were investigated, in animals the focus was often on the aorta, in order to better understand the distribution in the vicinity of branch openings. This vessel features an almost regularly arranged sequence of intercostal branch ostia, followed by a range of larger side branches and abdominal branches, before bifurcating into two iliac arteries. The aorta of a rabbit with its major branches is shown in figure 1.2.

The focal nature of atherosclerosis demonstrates that its development is not only affected by the well-known systemic risk factors, but also by local factors. The influence of these local risk factors must be powerful: the protected regions can remain essentially free of disease even when disease-prone sites have developed it to

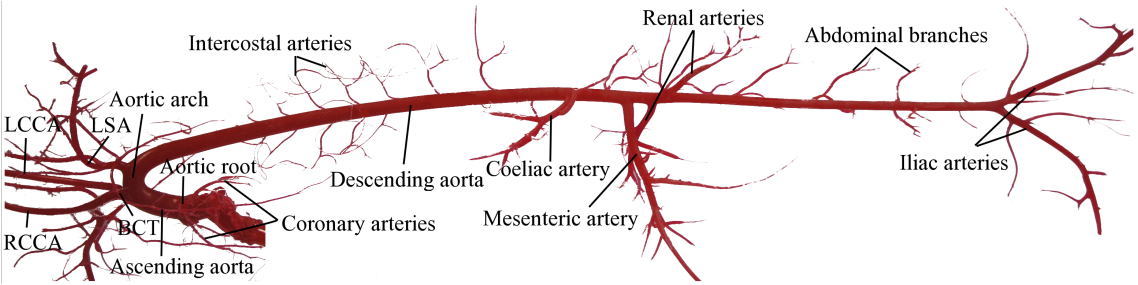

Figure 1.2: The aorta of a rabbit, with its major branches (LCCA: left common carotid artery; RCCA: right common carotid artery; LSA: left subclavian artery; BCT: brachiocephalic trunk).

a life-threatening extent, making the search for local risk factors a worthwhile cause (Weinberg, 2004).

1.1.2.2 Hypothesised mechanisms

If we can understand why some blood vessels seem naturally protected against cardiovascular disease, we can apply this knowledge to identify arteries that are at risk and design more effective treatment strategies. A variety of mechanisms explaining the spatial heterogeneity of atherosclerosis have been hypothesised. Already in the nineteenth century von Rindfleisch (1872) argued: "... there are many grounds for thinking that a mechanical irritation of the vascular wall may be at least one of the causes to which the morbid changes are due. For these are chiefly found at such points as are exposed to the full stress and impact of the blood ...". We now recognise that two factors in particular may vary from one location in the vascular tree to another:

- Blood flow and its effects on the arterial wall;
- Arterial wall properties.

Blood flow could play a role in the atherogenic process through two different mechanisms. On the one hand, spatial differences in blood flow characteristics lead to differences in the state of mixing of the blood. Since the rate of transendothelial LDL transport increases with increasing endothelial exposure to LDL

(Nielsen, 1996), these differences in mixing could be responsible for the patchiness of atherosclerosis (Vincent et al., 2010).

On the other hand, the varying blood flow characteristics result in a non-uniform distribution of the mechanical forces exerted by the flowing blood on the vessel wall (Asakura and Karino, 1990; Kazakidi et al., 2009). The stresses on the vessel wall can be decomposed into pressure, normal to the vessel wall, and shear stress, tangential to the vessel wall[2]. Both components have been suggested to be involved in atherosclerosis. Pressure-related theories include the effect on arterial permeability of increased static pressure from turbulence (Wesolowski et al., 1965) and Bernoulli-type reductions in static pressure (Texon, 1986). Although in absolute terms pressure dominates over shear stress, with pressures being several orders higher than shear stress magnitudes, in the relative sense local variations in shear stress are dominant over local variations in pressure. It has therefore been argued that shear stress plays the major role in the focal development of atherosclerosis. The nature of this role, however, has been the subject of debate since the late 1960s. While Fry (1969) suggested that high flow rates lead to endothelial damage and a subsequent pathological response, Caro et al. (1971) stated that low wall shear stress (WSS) may inhibit or disturb local mass transfer and instigate atherosclerosis. In the 1980s flow reversal was indicated as a key factor in the atherogenic process (Ku et al., 1985). The low/oscillatory shear theory is currently viewed as the consensus hypothesis.

Spatial differences in the *properties of the arterial wall* could also be the driving mechanism for the focal nature of atherosclerotic disease. It has been speculated that increased collagen production, resulting from pulsatile wall stretch owing to the pulse pressure, may induce vessel wall injury, and also intramural stresses have been suggested to correlate with the disease distribution (Thubrikar et al., 1990). In addition, differences in wall permeability might lead to variations in transport of proteins and other blood components (Sebkhi and Weinberg, 1994, 1996; Forster and Weinberg, 1997; Ewins et al., 2002; Staughton and Weinberg, 2004).

[2]The wall shear stress is more formally introduced in section 1.2.2.

It is not unlikely that changes in *blood flow* and *arterial wall properties* interact with each other. Local differences in the properties of the arterial wall might influence blood flow characteristics; think for example of how changes in wall stiffness can affect blood flow. The reverse reasoning holds equally well; wall stresses resulting from blood flow might modify the behaviour of endothelial cells, thereby changing the wall permeability.

1.1.3 Age-dependency of lesion patterns

1.1.3.1 Apparent paradox

Understanding the distribution of atherosclerotic lesions in the vicinity of branch ostia, which are preferred targets of the disease, may eventually lead to the development of new diagnostic tools and treatment strategies. Lesions around various branches were mapped by different research groups, but interestingly the distributions were not always consistent.

Caro et al. (1971) found that the region downstream of branch openings in the aorta of humans shows least signs of disease, and also Sloop et al. (1998) reported cases in which lesions developed predominantly at the upstream side of ostia. However, Sinzinger et al. (1980) could not confirm this observation and concluded that lesions preferentially occurred downstream of ostia. This apparent paradox, strengthened by the fact that these studies all used human subjects, could be solved when taking the age of the subjects into account (Weinberg, 2004). Athero-prone regions move from downstream of branch ostia in young humans (Sinzinger et al., 1980) to more lateral and upstream locations in adults (Sloop et al., 1998).

Since animals are often used in studies of atherogenesis, Weinberg (2002) investigated if a similar shift occurred in other species. Although there was no evidence for a change from a downstream to an upstream distribution with age in pigeons (Richards and Weinberg, 2000), the distribution did switch in rabbits. In immature rabbits lesions predominantly occur downstream of the branches and are often constrained to an arrowhead-shaped area below the ostium (Barnes and Weinberg,

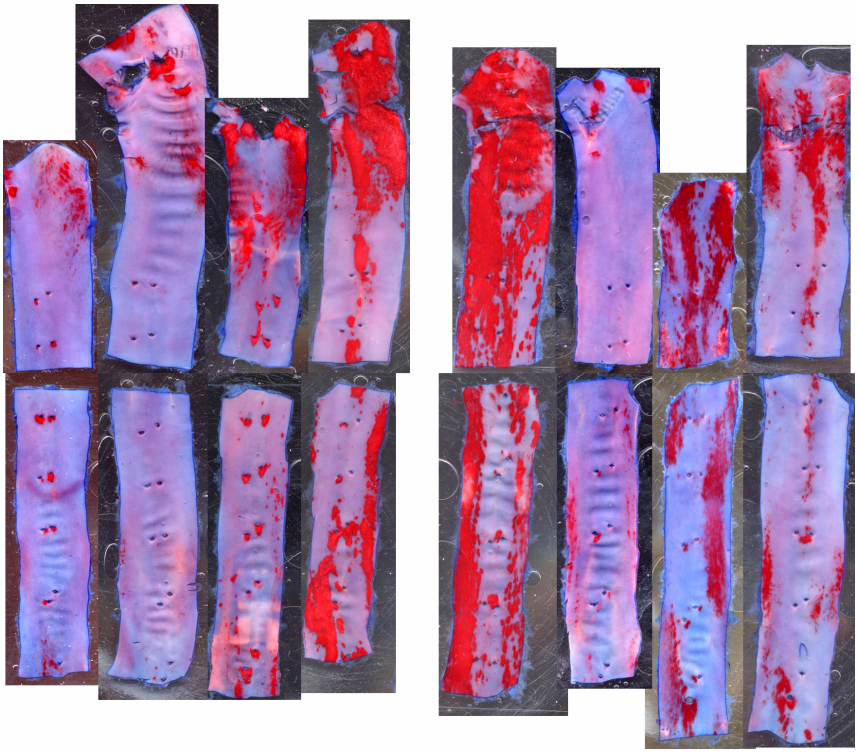

Figure 1.3: Lesion patterns in the descending thoracic aortas of 4 immature (left) and 4 mature (right) cholesterol-fed rabbits. The luminal surface of each segment, opened ventrally, is shown *en face*. (The aortas are divided at the third pair of intercostal ostia, which was removed for a different study.) This is a subset of the data from Cremers et al. (2011), showing cases that were most different from each other.

1998, 1999; Forster et al., 1996; Weinberg, 2002). With ageing the most lesion-prone zones move laterally (Barnes and Weinberg, 1998, 1999, 2001).

Cremers et al. (2011) performed an extensive study of age-related changes in the localisation of early atherosclerotic lesions in the descending aorta of hypercholesterolaemic rabbits. Figure 1.3 shows a subset of their results. The study confirmed that early lesions predominantly develop in a triangular region downstream of aortic branch orifices in immature rabbits, while this region is largely spared of lesions in mature rabbits[3]. Furthermore, they found that lesions occur as longitudinal or spiral stripes away from branches, and that this pattern is more obvious in mature than in immature vessels.

[3]Rabbits are sexually mature around 6 months of age (Berger et al., 1982).

1.1.3.2 Hypothesised mechanisms

As was argued in section 1.1.2.2, differences in arterial wall properties and/or blood flow characteristics are thought to be responsible for the focal nature of atherosclerosis. Changes with age in the focal distribution provide an additional challenge for theories of atherogenesis. It is interesting to investigate if differences in arterial wall properties or blood flow are age-dependent, for this would considerably strengthen the evidence. A few studies have been devoted to the unravelling of this apparent paradox.

Studies which have investigated potential changes with age in *arterial wall properties*, have often focused on intercostal branching regions in the aorta of rabbits. In particular, mass transport through the endothelium has been compared for immature and mature animals. Age-related changes in albumin uptake, as a model for LDL uptake, have been observed (Sebkhi and Weinberg, 1994, 1996; Forster and Weinberg, 1997; Ewins et al., 2002; Staughton and Weinberg, 2004). A more accurate picture of variations in mass transport could be obtained by imaging the full aorta using *en face* confocal microscopy.

If, as these studies suggest, arterial wall uptake changes with age, the question still remains why this is the case. A potential answer to this problem could once more be that also *blood flow characteristics* change with age. This hypothesis was investigated by Bond et al. (2011), who examined endothelial cell and nuclear elongation in aortas of young and old rabbits. Under the assumption that these parameters are shear-dependent (Flaherty et al., 1972), their data suggested a positive correlation of WSS with lesion prevalence, in contrast to the current low/oscillatory shear consensus which was introduced in section 1.1.2.2. However, it can be argued that nuclear morphology reflects factors other than WSS. For example, endothelial cells elongate in response to cyclic stretch as well as shear (Zhao et al., 1995), and the elongatory effect of shear can be amplified by flow pulsatility (Helmlinger et al., 1991).

1.1.4 Animal models of atherosclerosis

A range of species have been used to further our understanding of atherosclerosis, from mice (Nakashima et al., 1994) and rabbits (Cremers et al., 2011) to dogs (Fry, 1968) and pigs (Koskinas et al., 2010). High-fat diets are often administered to induce or accelerate the disease process. For example, spontaneous lesion formation in rabbits is rare (Barnes and Weinberg, 1998, 2001), but lesions can be induced by a cholesterol-enhanced diet (Forster et al., 1996; Barnes and Weinberg, 1999). Mice can be genetically modified to develop well-advanced and widely-distributed lesions on Western or normal mouse diets, while avoiding prolonged administration of high-cholesterol diets with toxic additives (McGillicuddy et al., 2001). Commonly used murine models of atherosclerosis have apolipoprotein E (ApoE-/-) or low density lipoprotein receptor (Ldlr-/-) null mutations. Smaller laboratory animals are particularly popular because of their relatively low cost of purchase and maintenance, ease of breeding and the relatively rapid progression of atherosclerosis in these animals (Getz and Reardon, 2012).

Although animal models of atherosclerosis are certainly useful, it is important to keep in mind that pathologic mechanisms may differ between species. This applies to smaller laboratory animals in particular. Allometric arguments show that haemodynamic parameters, such as the heart rate and local Reynolds numbers (defined in section 1.2.1), depend on body mass and are hence different in small animals compared to humans (Weinberg and Ethier, 2007). However, these parameters are thought to influence atherogenesis, as will be argued in the thesis presented here.

1.2 Haemodynamics

It follows from section 1.1 that local differences in blood flow provide at least one possible mechanism that could explain the focal nature of atherosclerotic disease. With this explanatory potential in mind, a large number of research groups have studied haemodynamics, the dynamics of the flow in blood vessels. This section introduces some concepts which are essential in the field of haemodynamics.

1.2.1 The Navier-Stokes equations

The motion of fluids is governed by the continuity equation, which describes conservation of mass, and the Navier-Stokes equations, which describe conservation of momentum:

$$\frac{\partial \rho}{\partial t} + \nabla \cdot (\rho \mathbf{u}) = 0 \tag{1.1}$$

$$\rho\Big(\frac{\partial \mathbf{u}}{\partial t} + \mathbf{u} \cdot \nabla \mathbf{u}\Big) = \nabla \cdot \overset{\leftrightarrow}{\tau} + \mathbf{f} \tag{1.2}$$

with

$$\overset{\leftrightarrow}{\tau} = -p \overset{\leftrightarrow}{\delta} + 2\mu \overset{\leftrightarrow}{S}$$

$$\overset{\leftrightarrow}{S} = \frac{1}{2}\Big(\nabla \mathbf{u} + (\nabla \mathbf{u})^T\Big) - \frac{1}{3}\Big(\nabla \cdot \mathbf{u}\Big) \overset{\leftrightarrow}{\delta}$$

where ρ represents the density of the fluid, t the time, $\mathbf{u}$ the velocity vector, $\overset{\leftrightarrow}{\tau}$ the stress tensor, $\mathbf{f}$ the body forces, p the pressure, $\overset{\leftrightarrow}{\delta}$ the unit tensor, μ the dynamic viscosity and $\overset{\leftrightarrow}{S}$ the rate of strain tensor.

The equations can be simplified for blood flow. Firstly, at physiologically realistic flow velocities blood can be considered as an incompressible fluid (constant ρ). Moreover, at high shear rates it is reasonable to assume that blood acts as a Newtonian fluid, i.e. μ is constant (Johnston et al., 2006)[4]. Finally, the effect of body forces can be neglected. The governing equations can therefore be reduced to:

$$\nabla \cdot \mathbf{u} = 0 \quad \text{in } \Omega \tag{1.3}$$

$$\frac{\partial \mathbf{u}}{\partial t} + \mathbf{u} \cdot \nabla \mathbf{u} = -\frac{1}{\rho}\nabla p + \nu \nabla^2 \mathbf{u} \quad \text{in } \Omega \tag{1.4}$$

where Ω represents the vascular geometry in which the blood flows and $\nu = \mu/\rho$ is the kinematic viscosity. The left-hand side of equation (1.4) contains a time-dependent contribution and a non-linear convective term, while the right-hand side contains a pressure and a viscous, diffusive term.

[4]In regions of slow flow, the use of a Newtonian approximation in combination with the shear-thinning behaviour of the blood results in a slight underestimation of the WSS (Johnston et al., 2004).

A final assumption that was implicitly made here is that blood may be treated as a homogeneous fluid, which is justified by the orders of magnitude difference in the length scales of large arteries such as the aorta versus red blood cells. Steinman (2011) noted that this presumes that the length scales of the flow features are similarly large, an implicit assumption that may well be violated under conditions of pathological flow.

The set of equations (1.3)-(1.4) is complemented by corresponding boundary conditions, which directly or indirectly prescribe the solution on the boundary $\partial\Omega$. In general, this boundary is not fixed as arterial walls can move and deform throughout the cardiac cycle. Initial conditions describe the flow field at $t = 0$. The solution to this complex problem dictates the velocity and pressure of the flowing blood, but a generic analytic solution is not available.

The Navier-Stokes equation can be non-dimensionalised using characteristic reference magnitudes for the velocity u_0, length D_0 and time T:

$$\frac{1}{U_{\text{red}}}\frac{\partial \mathbf{u}^*}{\partial t^*} + \mathbf{u}^* \cdot \nabla^* \mathbf{u}^* = -\nabla^* p^* + \frac{1}{\text{Re}}(\nabla^*)^2 \mathbf{u}^* \tag{1.5}$$

where the asterik indicates the non-dimensional form of the variables. Two non-dimensional parameters emerge: the Reynolds number Re and the reduced velocity U_{red}.

The Reynolds number Re is defined as:

$$\text{Re} = \frac{\rho u_0 D_0}{\mu} \tag{1.6}$$

and is a measure of the ratio of inertial forces (ρu_0^2) to viscous forces ($\mu u_0 / D_0$). For high Re flows, inertial forces are dominant; the flow becomes turbulent when Re exceeds a critical value. Viscous forces are significant only at low Re; this is called laminar flow. Although blood flow is mostly laminar, instabilities and transition to turbulence may occur under certain conditions, for example in severe stenoses (Sherwin and Blackburn, 2005). Allometric arguments show that Re is dependent on animal size (Weinberg and Ethier, 2007), making turbulent effects more likely in larger animals. Given the focus on flow in rabbit aortas, the work presented here is limited to the investigation of laminar flow conditions.

The second dimensionless parameter in the non-dimensional Navier-Stokes equations is the reduced velocity, which is defined as:

$$U_{\text{red}} = \frac{u_0 T}{D_0} \tag{1.7}$$

For harmonic pulsatile flows the use of the Womersley parameter Wo is often preferred (Womersley, 1955). This parameter is defined as:

$$\text{Wo} = \frac{D_0}{2}\sqrt{\frac{\omega}{\nu}} \tag{1.8}$$

where $\omega(=1/\text{T})$ represents the frequency of the oscillation. Wo relates to the reduced velocity through the following expression:

$$U_{\text{red}} = \frac{\pi}{2}\frac{Re}{\text{Wo}^2} \tag{1.9}$$

The use of this parameter is explained in section 1.2.3.1.

1.2.2 Wall shear stress and related parameters

The wall shear stress vector $\boldsymbol{\tau}_w$ is the tangential force per unit area exerted by the flowing blood onto the vessel wall. For a Newtonian fluid, shear stress is proportional to the gradient of the velocity (shear rate), and $\boldsymbol{\tau}_w$ is consequently defined by:

$$\boldsymbol{\tau}_w = \Big[\mu(\nabla \mathbf{u}) \cdot \mathbf{n}\Big]_{\text{wall}} \tag{1.10}$$

where $\mathbf{n}$ represents the vector normal to the vessel wall. Since blood flow is pulsatile, $\boldsymbol{\tau}_w$ is both space- and time-dependent. Various metrics related to $\boldsymbol{\tau}_w$ have been shown to influence endothelial cell behaviour (Flaherty et al., 1972; LaMack et al., 2010; Chakraborty et al., 2012). In a steady-state sense the magnitude of $\boldsymbol{\tau}_w$ (WSS) has been considered to be physiologically relevant. Time-integrated metrics that have been used extensively to characterise the flow field are the time-averaged wall shear stress (TAWSS), the oscillatory shear index (OSI) and the relative residence

time (RRT):

$$\mathrm{TAWSS} = \frac{1}{T}\int_0^T |\boldsymbol{\tau}_w| \mathrm{d}t \tag{1.11}$$

$$\mathrm{OSI} = \frac{1}{2}\left(1 - \frac{\left|\int_0^T \boldsymbol{\tau}_w \mathrm{d}t\right|}{\int_0^T |\boldsymbol{\tau}_w| \mathrm{d}t}\right) \tag{1.12}$$

$$\mathrm{RRT} \sim \frac{1}{\mathrm{TAWSS}\big(1 - 2\mathrm{OSI}\big)} \tag{1.13}$$

The TAWSS can be regarded as the time-integrated version of the WSS magnitude and is insensitive to the direction of the WSS vector. The OSI, which was originally defined in a two-dimensional sense (Ku et al., 1985) and only later extended to the three-dimensional case (He and Ku, 1996), is a measure for the oscillatory character of the flow. The RRT, finally, expresses the importance of the residence time of solutes and formed elements of the blood in the neighbourhood of vascular endothelium (Himburg et al., 2004). It is a relative concept, because all non-adherent particles in the flow are moving and therefore have zero effective residence time at any location.

1.2.3 Flow in idealised geometries

Arteries have three-dimensional tortuous geometries and the dynamics of the flowing blood inside them can be highly complex. Many research groups have used simplified models to gain a better understanding of the relevant flow mechanics (Friedman et al., 1975; Lou and Yang, 1992; Kazakidi et al., 2009). The current section gives a few examples to illustrate the basic fluid dynamic principles.

1.2.3.1 Straight pipe

Steady-state flow Laminar flow in a long straight pipe is known as Poiseuille flow and has a parabolic axial velocity profile. This can be understood from the following reasoning. When a flow with uniform velocity enters a rigid-walled cylinder, the velocity profile is originally plug-like, as is illustrated in figure 1.4(a). Since the flow has to conform to the no-slip condition, which states that the velocity at the wall is zero relative to the wall, a viscous boundary layer will start to grow; the near-wall

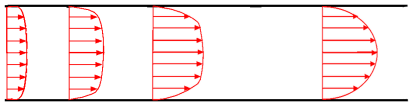

(a) Straight pipe

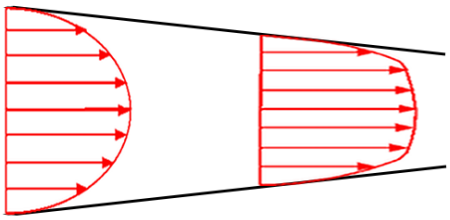

(b) Tapered pipe

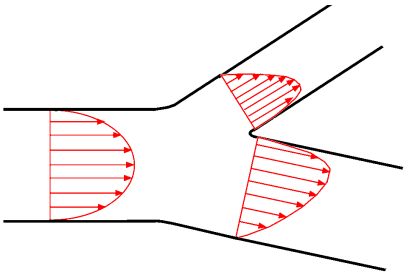

(c) Bifurcation

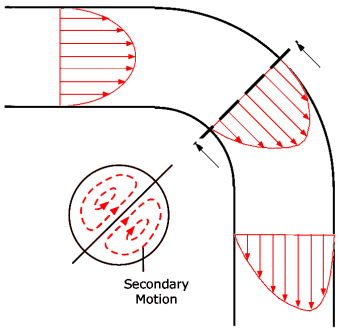

(d) Curved pipe

Figure 1.4: Illustrations of velocity profiles for steady laminar flow in 4 idealised geometries. In (a) a uniform velocity profile is assumed at the pipe inlet, while in (b)-(d) the inlet velocity profile is parabolic.

fluid progressively decelerates, while the flow near the axis of the tube accelerates to conserve the flow rate (equation (1.3)). After a certain entrance length, estimated at $0.03\mathrm{Re}D_0$ (Parker and Caro, 1993), the flow reaches its fully-developed state with a constant parabolic velocity profile and zero in-plane flow (due to axisymmetry). The WSS, which is originally elevated, gradually reduces and becomes equal to:

$$\mathrm{WSS}_{\text{fully-developed}} = \frac{32\mu Q}{\pi D^3} \tag{1.14}$$

where Q is the volume flow rate through the pipe and D the local pipe diameter.

Pulsatile flow Due to the contractions of the heart, blood flow in arteries is pulsatile. For low frequencies, the flow can be considered quasi-steady: the velocity preserves its parabolic profile throughout the cardiac cycle. However, for higher frequencies a quasi-steady assumption is no longer justifiable. The Womersley parameter Wo, which was introduced in section 1.2.1, is used to evaluate how the profile will change. The quasi-steady behaviour occurs for $\mathrm{Wo} < 1$. When Wo is large (> 10), the velocity profile flattens; there is not enough time in the cycle for the velocity profile to develop. For larger Wo, the maximum velocity no longer remains on the axis of the pipe throughout the cycle. Whereas the near-wall fluid, which has a low velocity and hence low momentum, remains in phase with the driving pressure gradient, the fluid closer to the axis with higher velocity does not.

1.2.3.2 Tapered pipe

Fully-developed flow in a tapered pipe is called Jeffery-Hamel flow (Jeffery, 1915; Hamel, 1916). Due to conservation of mass (equation (1.3)) the average axial velocity in a tapered pipe varies as $1/D^2$. The axial velocity profile is more blunt compared to the parabolic profile in a straight pipe. This is illustrated in figure 1.4(b). The flow also has a radial in-plane component, pointing towards the axis of the pipe. The WSS in a converging tapered pipe increases along the pipe in line with the increasing average velocity and, due to the blunted velocity profile, the WSS will be higher than the value determined by equation (1.14) at any cross-section.

1.2.3.3 Bifurcation

Figure 1.4(c) illustrates that, when flow from a straight pipe with a fully-developed profile encounters a bifurcation, the velocity profile will no longer be parabolic downstream of the bifurcation. The blood arriving at the flow divider hits the inner walls of the bifurcation, resulting in a region of high WSS, while the outer walls are exposed to low WSS. At high initial velocities and sharp bifurcation angles the flow may even separate along the outer walls; a recirculation zone has developed.

The velocity profile in the daughter branches is skewed towards the inner wall, as is illustrated in figure 1.4(c). New boundary layers develop and, after a certain entrance length, a Poiseuille flow type re-establishes in both daughter branches.

1.2.3.4 Pipe with curvature and torsion

The curvature and torsion of a pipe describe the 3D bending of the pipe and twisting of its plane of curvature respectively. The influence of curvature on fluid flow in a pipe can be characterised by the Dean number De, which is defined here as:

$$\mathrm{De} = \mathrm{Re}\sqrt{\frac{D_0}{2R_c}} \tag{1.15}$$

where R_c represents the radius of curvature, or $\kappa = 1/R_c$ the curvature of the pipe. Note that different definitions of De are in use (Dean, 1927, 1928). For a straight pipe De is zero, and De increases with increasing curvature.

The physics of fluid motion in pipes with curvature and torsion is detailed in Alastruey et al. (2012). The introduction of curvature gives rise to centrifugal forces, which point away from the centre of curvature. Interaction between the centrifugal forces and an in-plane pressure gradient gives rise to secondary motion, as is illustrated in figure 1.4(d). At the start of the bend, the in-plane pressure gradient is centripetal (toward the centre of curvature) and smaller than the centrifugal force in the core flow, and circumferential and greater than the centrifugal force near the wall. The resulting convective acceleration is centrifugal in the core flow and has a spiral pattern near the lateral walls. Moving downstream, both regions of spiral convective acceleration are gradually transformed into two regions of radial convective

acceleration, generating circular secondary motions. The pair of counter-rotating vortices that form, are called Dean vortices.

A curvature-dependent Coriolis force accelerates the fluid particles with a centripetal velocity and decelerates fluid particles with a centrifugal velocity, shaping the velocity profile from circular (parabolic) to crescent shapes. As a consequence the peak velocity is displaced toward the outer curvature of the pipe, as is shown in figure 1.4(d). Because of the skewed velocity profile, WSS is higher along the outer curvature of the pipe and lower along the inner wall.

Geometries with non-zero torsion are intrinsically non-planar. The introduction of torsion breaks the symmetry of the Dean vortex pair, either by making one vortex more dominant or by completely obliterating the second vortex, depending on the values of De and torsion-related parameters (Doorly and Sherwin, 2009).

1.2.4 Flow in arteries

The vascular system is an assembly of bifurcating arteries with varying curvature, torsion and cross-section. All fluid dynamic effects explained in section 1.2.3 are therefore present and can interact with each other. In addition, arteries are not necessarily circular in cross-section. The hydraulic diameter is often used to describe non-circular shapes. This parameter is defined as:

$$\mathrm{D}_0 = \frac{4A_0}{P_0} \tag{1.16}$$

where A_0 represents the area and P_0 the perimeter of the cross-section. For a circular cross-section, the hydraulic diameter is equal to the diameter.

Calculation of the WSS in arteries requires accurate velocity measurements close to the wall to estimate the near-wall shear rate. This can be done *in vivo* (Jones et al., 1992; Irace et al., 2011) or *in vitro* using experimental set-ups (Caro et al., 1971; Ahmed and Giddens, 1984). However, even with state-of-the-art equipment, velocity measurements are not very well resolved (Steinman, 2004), although recent improvements in MRI techniques are likely to instigate its use for *in vivo* WSS measurements (Stalder et al., 2008). To overcome difficulties in velocity measurements,

WSS was often estimated by assuming simplified laws for the velocity profile, such as Poiseuille flow (Simon and Levenson, 1990). Since the complex flow in arteries is difficult, often even impossible to capture using such laws, this strategy does not always lead to accurate results.

This justifies the need for alternative ways to assess blood flow characteristics and WSS. Computational fluid dynamics (CFD) is widely used in the field of bioengineering to compute arterial WSS (Friedman et al., 1975; Cheer et al., 1998; Knight et al., 2010; Hoi et al., 2011). Numerical methods are employed to approximate the equations for fluid flow since an analytic solution is not available except in simple cases. CFD has the advantage of providing three-dimensional flow fields, enabling the calculation of haemodynamic factors such as WSS on the entire arterial wall. For the rabbit aorta, CFD has been used to study flow in an idealised model of a single intercostal artery branching off the thoracic aorta (Kazakidi et al., 2009, 2011) and in a geometrically accurate model of one (mature) rabbit thoracic aorta (Vincent et al., 2011), but has not yet been applied to evaluate age-related changes in blood flow characteristics.

1.3 Research aims

The thesis presented here aims to further our understanding of atherosclerosis, the condition underlying most cardiovascular diseases, as a first step towards the design of new prevention, diagnosis and treatment strategies of cardiovascular disease. Given the localisation of atherosclerotic lesions in branching regions and curved vessels, the thesis works from the hypothesis that the initiation of atherosclerosis is flow-dependent. The ultimate goal is to identify haemodynamic markers that are involved in the atherogenic process and act as local risk factors.

Recognising the vast amount of literature on the relation between blood flow and atherogenesis, the first research aim of the thesis is to evaluate the evidence for a correlation between early atherosclerosis and WSS. The findings of this systematic review are the starting point for the design of a novel study investigating the

relation between blood flow and age-dependent atherogenesis in the rabbit aorta. Since blood flow characteristics are heavily dependent on vascular geometry, a second research aim is to identify age-related changes in the geometry of the rabbit aorta. The reliable reconstruction of the subject-specific rabbit aorta is important for this analysis. Thirdly, blood flow is simulated in the individual geometries using computational fluid dynamic tools, and age-related differences in flow features are analysed. Finally, the potential of haemodynamic metrics to predict the distribution of atherosclerotic lesions in the rabbit aorta is assessed. The fourth research aim is to assess the explanatory potential of traditionally used metrics, while the fifth research aim is to develop and assess new tools to characterise physiologically relevant flow features.

The research aims of the thesis presented here can be summarised as follows:

1. To understand the current view on the relation between blood flow and atherogenesis;
2. To identify age-related changes in the geometry of the rabbit aorta;
3. To identify age-related changes in blood flow characteristics in the rabbit aorta;
4. To assess the potential of traditional haemodynamic metrics to predict the distribution of atherosclerotic lesions in the rabbit aorta;
5. To develop and assess new tools for the characterisation of physiologically relevant flow features.

1.4 Outline

At the core of this thesis is a comparative study of age-related changes in lesion distribution and blood flow characteristics in the aorta of rabbits. The work is presented in a series of chapters; chapters 2 to 6 each address one of the research aims introduced in section 1.3. The study design is schematically illustrated in figure 1.5.

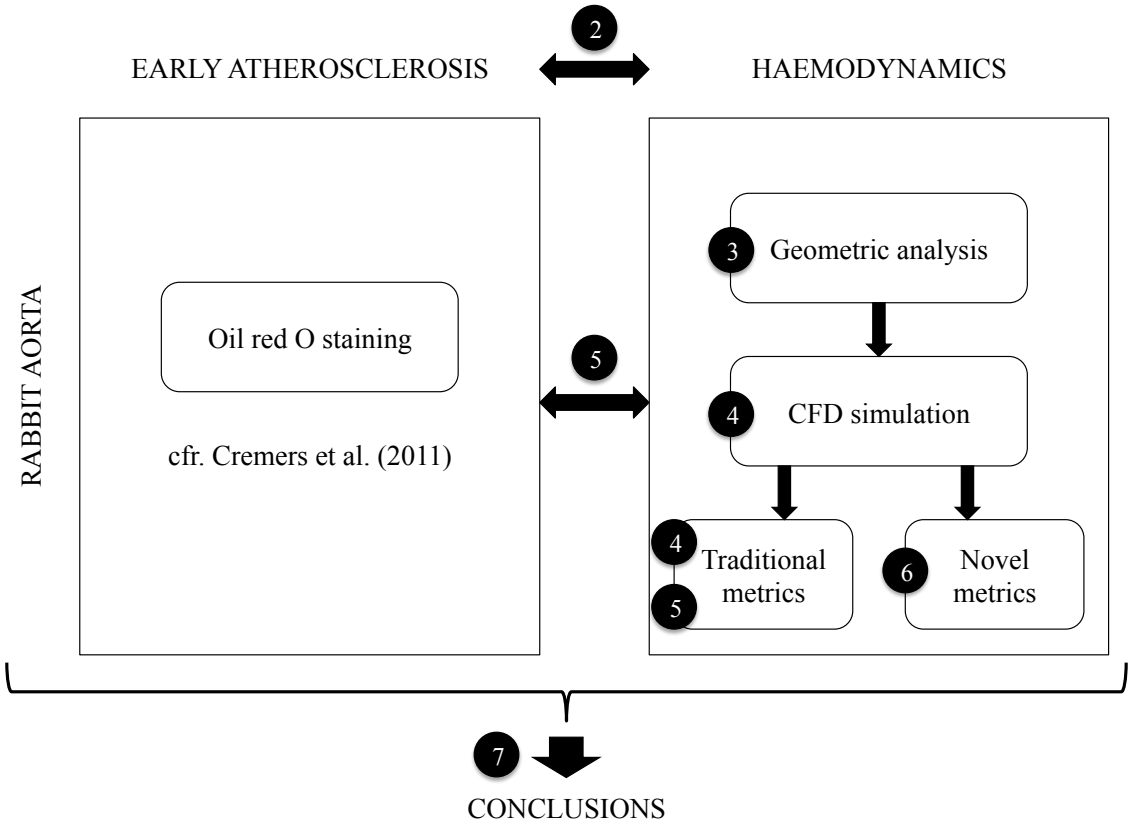

Figure 1.5: Outline of the thesis presented here. The numbers in black circles indicate the chapters in which each part of the study is detailed.

Since the concept that blood flow plays a role in early atherosclerosis has been around for more than a century (von Rindfleisch, 1872), chapter 2 presents a review of articles investigating this relationship. To increase the rigour of the review, it is conducted in the systematic fashion used for assessing clinical trials. The methods used to compare distributions of atherosclerotic disease with flow-related parameters are discussed in detail, and conclusions are drawn on the current status of our knowledge regarding the character of the relation between early atherosclerosis and blood flow.

Chapter 3 presents a geometric analysis of the rabbit aorta, as a first step towards the integrated haemodynamic study. Advantages and drawbacks of techniques for geometry acquisition are discussed and a dataset of aortic geometries of immature and mature rabbits is presented. In line with the second research aim, age-related differences in the aortic geometries are investigated. Finally, the accuracy of the dataset is analysed and potential consequences for the conclusions of the geometric analysis are assessed.

Chapter 4 first introduces the numerical methods used as part of the thesis presented here to simulate blood flow in vascular geometries. These methods are then applied to the rabbit aortic dataset obtained in the previous chapter, and distributions of flow-related parameters such as the WSS are calculated. Simulations of flow in idealised geometries are used to gain a better understanding of the governing flow features and age-related differences in the anatomically representative geometries.

The comparative study culminates in chapter 5, in which the patterns of WSS are compared to distributions of atherosclerotic lesion prevalence in immature and mature rabbit aortas from the literature. This is done first qualitatively, and afterwards a statistical technique is designed and applied to quantitatively correlate the distribution maps.

Chapter 6 investigates the haemodynamic results from a different angle: the chapter questions if metrics traditionally used in the field of haemodynamics can correctly identify different flow fields. Novel ways to better characterise disturbed

flows are introduced and applied to the pulsatile flow in idealised and anatomically realistic geometries. The physiological relevance of these techniques are also discussed.

Research conclusions are presented in chapter 7, together with suggestions for further work.

Chapter 2

Atherogenesis and blood flow: a systematic review

The non-uniform distribution of atherosclerotic lesions in the arterial system had been noted and attributed to variation in blood flow characteristics as early as the nineteenth century (von Rindfleisch, 1872). Today, the concept that local haemodynamic factors account for the patchiness of the disease has become almost universally accepted by researchers in the field (Steinman, 2004). This acceptance emerged after a period of several decades during which the nature of the flow features that drive atherogenesis was the subject of considerable debate. While Fry (1969) suggested that high WSS leads to endothelial damage and a subsequent pathological response, Caro et al. (1971) proposed that high WSS was protective, lesions instead occurring in regions of low WSS. In the 1980s flow reversal was identified as another key factor, and the OSI was introduced by Ku et al. (1985) to quantify it. This index has the time-averaged magnitude of wall shear stress in the denominator, so high OSI tends to be associated with a low mean shear; the low and oscillatory shear theories have become fused to some extent.

Other haemodynamic theories, which have attracted less attention, involve increased static pressure from turbulence (Wesolowski et al., 1965), Bernoulli-type reductions in static pressure (Texon et al., 1965), fluctuations of pressure in conjunction with moderate shear stress (Blackshear et al., 1982), small excursions of

WSS during the cardiac cycle (Friedman et al., 1981), high harmonic content of variations in WSS (Himburg and Friedman, 2006), steep spatial gradients in WSS (Lei et al., 1995) and multidirectional shear (McMillan, 1985).

In their review of fluid dynamics at arterial bifurcations, Lou and Yang (1992) noted, "The theory of low shear stress prevails at the moment, although the correlation between high-atherosclerosis probability areas and expected regions of low wall shear stress is far from perfect. It is, therefore, not prudent to accept one theory over another." Twenty years later, the low and/or oscillatory WSS hypothesis has become the consensus mechanism for the initiation of atherosclerosis (Cecchi et al., 2011). Some studies even rely on the theory for the development or assessment of potential diagnostic or treatment strategies (Sawchuk et al., 1999; Redaelli et al., 2004). This chapter aims to ascertain if the literature really does justify the consensus. A literature review was conducted in a systematic fashion. Since, as highlighted in section 1.2.4, CFD-based methods currently provide the most reliable WSS estimates, articles that compared CFD-derived metrics with lesion distributions were identified. Their methods and findings were assessed to gauge the strength of the evidence for the consensus view of the relationship between WSS and atherosclerosis.

Section 2.1 presents criteria for in- or exclusion of articles in the review. An overview of the literature search is provided in section 2.2. Findings are presented in section 2.3, and critically assessed in section 2.4.

2.1 Inclusion and exclusion criteria

A systematic search was conducted on the PubMed database (`pubmed.com`). The search was restricted to primary research articles published online before 21 March 2012. Articles were selected if at least one keyword from each of the following three groups appeared in their abstract and/or title:

- athero, atheroma, atheromata, atheromatous, atherosclerosis, atherosclerotic, atherogenesis, atherogenic, intima-media thickness, intimal thickness, wall thickness;

- shear;
- CFD, computational, computation, compute, computed, computing, numerical, calculation, calculate, calculated, calculating, simulation, simulate, simulated, simulating.

The abstracts of these articles were evaluated against a set of inclusion and exclusion criteria. To be included, compliance with the following criteria was required:

- The presented work was an original contribution;
- CFD was used to simulate blood flow in one or more vascular geometries;
- At least one of the vascular geometries used as an input for the CFD analysis was anatomically realistic. A geometry was considered anatomically realistic if it was based on measurements or images, represented a sufficiently extended vascular region and included all the features necessary to capture the physiologically relevant 3D flow dynamics;
- The localisation of atherosclerotic lesions in the region of interest was based on the distribution of an established marker of the disease, presented either as an original contribution in the article, in a companion paper from the same group, or in a cited article from a different research group. In all cases, the species used for the disease localisation study and CFD analysis had to match;
- The patterns of shear-related parameters in the region of interest were shown or described in detail, and compared with the localisation of disease in the same region;
- The relation between blood flow and the initiation of atherosclerosis was discussed.

If compliance with these criteria could not be determined from the abstract, the article was hand-searched.

Explicitly excluded from the review were:

- Studies that performed CFD on severely stenosed geometries and compared the resulting WSS maps with the spatial distribution of occlusion in these geometries. With such advanced disease, it cannot be assumed that variations in shear are a cause rather than an effect of the lesion;

- Studies in which the geometries for the CFD analysis were obtained after angioplasty or endarterectomy in the region of interest, since these techniques cannot guarantee an accurate reproduction of the original "healthy" vascular geometry;

- Studies in which a stent, cuff, graft or other foreign object was introduced in the region of interest, since contact with the foreign material or stresses induced by the presence of the object may trigger mechanisms unrelated to normal atherogenesis; studies in which the geometry of the vascular region of interest was itself surgically altered, e.g. by anastomosis, were also discarded since effects related to the surgery may act as confounding factors;

- Studies in which the disease was mechanically induced, e.g. by denudation of the endothelium. Although these studies may help us understand the progression of the disease, they do not replicate the normal initial stages of the disease process;

- Studies in which gene expression, white blood cell density or LDL permeability were used as surrogates for lesions, since these properties are not established markers of the disease.

2.2 The available literature

A flow chart of the literature search is shown in figure 2.1. The initial search produced 406 articles, spanning 37 years of research. Excluding reviews and articles that did not concern atherosclerosis or its relation to blood flow left 360 articles. 231 of those used CFD to simulate blood flow and calculated WSS in one or more vascular geometries. Many papers that were excluded in this step calculated WSS

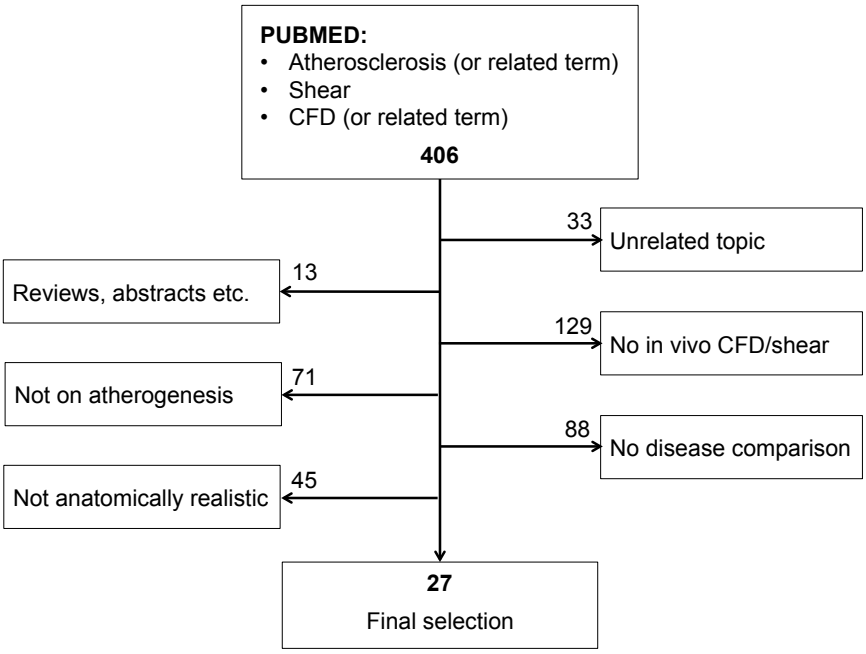

Figure 2.1: Flow chart of the search strategy for the selection of articles to be included in the review.

from velocity measurements, often by assuming fully developed (Poiseuille) flow. Some of the excluded articles focused on CFD in relation to *in vitro* experiments, rather than providing an insight into the *in vivo* haemodynamics. Another 159 papers were discarded because they did not compare their CFD results in detail with the localisation of atherosclerotic lesions in the relevant species, or did not relate their results to the initial stages of the disease. 45 articles were dismissed because the geometries employed in the CFD analysis were considered to lack anatomical details that could be relevant to the 3D flow dynamics. (A paper by Krams et al. (1997) was not rejected even though results were presented for a vascular region that had undergone angioplasty, because the authors noted that their conclusions remained unchanged when only the vessel segment upstream of the angioplasty was analysed.)

The remaining 27 articles were included; they originated from 15 different institutions (based on the affiliation of the corresponding author). A full list is provided in table 2.2. Besides human blood vessels, porcine, rabbit and murine models were

Table 2.1: Species and vascular regions of interest in the final selection of articles.

Species / Vessel	Human	Porcine	Rabbit	Murine
Coronary arteries	12	4	-	-
Carotid bifurcation	5	-	-	-
Aorta	1	-	2	2
ICA	1	-	-	-

used (table 2.1). Coronary arteries were the most popular region of interest, but the carotid bifurcation, aorta and internal carotid artery were also studied. In the animal studies, interventions were often required to initiate or accelerate the disease process: all animals were cholesterol-fed, mice had an ApoE-/- or Ldlr-/- mutation, and in one case the flow conditions were modified by surgical induction of aortic valve regurgitation (Hoi et al., 2011).

Most of the selected articles presented the localisation of the disease as an original contribution; in two cases this aspect was published separately (with at least one author in common with the article in the selection; Zhu et al. (2009) - Maeda et al. (2007); Hoi et al. (2011) - Zhou et al. (2010); and four articles compared their CFD results with disease distributions reported by other research groups (Perktold and Resch (1990), Perktold et al. (1991) - De Syo (1990); Taylor et al. (1998) - Cornhill et al. (1990); Suo et al. (2008) - Svindland (1983)). Buchanan et al. (1999, 2003) referred to previous work from their own (Herrmann et al., 1994; Malinauskas et al., 1995) and other (Zeindler et al., 1989) research groups but, because of the last exclusion criterion, only the comparison with the lesion distribution of Zeindler et al. (1989) is reviewed here.

2.3 Findings

Section 2.3.1 uncritically presents the results for the association between blood flow and atherosclerosis given in the reviewed articles. Subsequent sections also consider the methods that were used to obtain this evidence. Since different research

Table 2.2: Final selection of articles: references in chronological order, together with the affiliation of the corresponding author (or first author if no corresponding author was indicated) at the time of publication, species and vascular region of interest.

Reference	**Affiliation**	**Vessel**	**Species**
Perktold and Resch (1990)	Technical University Graz	Carotid	Human
Perktold et al. (1991)	Technical University Graz	Carotid	Human
Krams et al. (1997)	Thoraxcenter Erasmus MC	Coronary	Human
Taylor et al. (1998)	Stanford University	Aorta	Human
Buchanan et al. (1999)	North Carolina State University	Aorta	Rabbit
Steinman et al. (2002)	John P. Robarts Research Institute	Carotid	Human
Goubergrits et al. (2002)	Humboldt University Berlin	Carotid	Human
Wentzel et al. (2003)	Thoraxcenter Erasmus MC	Coronary	Human
Buchanan et al. (2003)	North Carolina State University	Aorta	Rabbit
Joshi et al. (2004)	University of Toronto	Coronary	Human
Wentzel et al. (2005)	Thoraxcenter Erasmus MC	Coronary	Human
Gijsen et al. (2007)	Thoraxcenter Erasmus MC	Coronary	Human
Augst et al. (2007)	Imperial College London	Carotid	Human
Chatzizisis et al. (2008)	Harvard Medical School	Coronary	Porcine
Suo et al. (2008)	Georgia Institute of Technology	Coronary	Human
Olgac et al. (2008)	ETH Zürich	Coronary	Human
Olgac et al. (2009)	ETH Zürich	Coronary	Human
Zhu et al. (2009)	Duke University	Aorta	Murine
van der Giessen et al. (2010)	Thoraxcenter Erasmus MC	Coronary	Human
Koskinas et al. (2010)	Harvard Medical School	Coronary	Porcine
Knight et al. (2010)	ETH Zürich	Coronary	Human
Hoi et al. (2011)	University of Toronto	Aorta	Murine
Chatzizisis et al. (2011)	Harvard Medical School	Coronary	Porcine
Samady et al. (2011)	Emory University School of Medicine	Coronary	Human
Siogkas et al. (2011)	Biomedical Research Institute, Ioannina	Coronary	Porcine
Zhang et al. (2012)	Beihang University	ICA	Human
Rikhtegar et al. (2012)	ETH Zürich	Coronary	Human

groups applied different levels of data reduction, section 2.3.2 investigates how data-processing methodologies differed between articles. Given the high sensitivity of blood flow to geometric changes, section 2.3.3 details at what stage of the disease process blood flow was characterised. Finally, section 2.3.4 gives an overview of the different techniques used to assess disease location. In each of these three sections, implications for the evidence concerning the role of blood flow in early atherosclerosis are discussed.

2.3.1 Many but not all articles interpret their results as supporting the low/oscillatory shear theory

2.3.1.1 Studies of steady flow

Based on the investigation of steady-state flow, a total of nine papers (33.3%) concluded that their results confirm the theory that low WSS promotes atherogenesis:

- Krams et al. (1997) and Wentzel et al. (2003, 2005) reported an inverse correlation between wall thickness and (steady) WSS;
- Goubergrits et al. (2002) saw a good visual correlation between locations of fibrous plaques and regions of low WSS;
- Chatzizisis et al. (2008) found that fibroatheromata and intermediate lesions develop in vascular segments with lower baseline WSS than segments with minimal lesions;
- Koskinas et al. (2010) observed a greater increase in maximum intima-medial thickness in vascular segments with low baseline WSS compared to vascular segments with high baseline WSS;
- Although Olgac et al. (2008) focused on the relation between atherosclerosis and LDL concentration, they reported a region of low WSS coincided with the location of a plaque;

- Siogkas et al. (2011) noted the largest plaque formation in a region of low WSS;

- Chatzizisis et al. (2011) found that lipid accumulation was enhanced in segments with low baseline WSS.

In contrast, a quantitative comparison by Gijsen et al. (2007) did not result in an overall relationship between WSS and wall thickness, and van der Giessen et al. (2010) could not establish a correlation between WSS and plaque thickness in a mildly diseased artery.

2.3.1.2 Studies of time-varying flow

The first papers which reported on time-varying flow, by Perktold and Resch (1990) and Perktold et al. (1991), concluded that the observed locations of atherosclerotic plaques correlated with the extent and location of a recirculation zone (and accompanying low shear regions) occurring during part of the cardiac cycle. However, most research groups who studied time-dependent dynamics focused their investigations on *time-integrated* effects.

Articles which discuss their results in terms of time-averaged wall shear stress (TAWSS), defined as the temporal average of the magnitude of the wall shear stress vector, are discussed first. Afterwards the focus is on articles which also considered other time-integrated, shear-derived metrics.

Time-averaged wall shear stress Three papers (11.1%) concluded that low TAWSS co-located with atherosclerosis or that its magnitude correlated inversely with its rate of progression:

- Suo et al. (2008) concluded that low TAWSS was co-located with an increased incidence of lesions,

- Zhu et al. (2009) compared TAWSS magnitudes in two mouse strains and found lower values in the strain having greater athero-susceptibility,

- Samady et al. (2011) found that plaque area increased over time in vascular segments with low TAWSS, but decreased in intermediate- and high-TAWSS segments.

In contrast to these articles, one study did not support the low TAWSS theory: Joshi et al. (2004) could not find a significant correlation between intimal thickness and WSS or TAWSS in 3 out of 4 arteries.

Other shear-derived metrics The OSI, first proposed by Ku et al. (1985) to characterise flow pulsatility and later generalised to three-dimensional flow (He and Ku, 1996), was computed alongside TAWSS in many of the reviewed papers, in order to investigate the influence of the oscillatory character of the blood flow on atherogenesis.

The conclusions for TAWSS and OSI were in agreement in four papers (14.8%), but there was inconsistency between the papers about whether these indices correlated with markers of early atherosclerosis:

- Taylor et al. (1998) and Buchanan et al. (1999, 2003) noted that regions of low TAWSS and high OSI both coincide with a high probability-of-occurrence of early atherosclerotic lesions;

- Although Olgac et al. (2009) focused on the relation between atherosclerosis and LDL concentration, they reported a region of low TAWSS and high OSI coincided with the location of a plaque;

- Steinman et al. (2002) could not find a quantitative general relationship between TAWSS or OSI and wall thickness.

In other cases the conclusions for TAWSS and OSI disagreed, or at least were not in strong agreement:

- Augst et al. (2007) computed TAWSS, OSI and wall shear stress angle gradients (WSSAG). They reported a significant relationship between WSS or WSSAG and intima-medial thickness in the common carotid artery immediately

Table 2.3: Overview of the various conclusions presented by the articles which satisfied all criteria of the systematic search.

Theory	**Correlation**	**No correlation**
Low steady WSS	9	2
Low instantaneous WSS	2	0
Low TAWSS	3	1
TAWSS and OSI	4	1
TAWSS or OSI or RRT	4	1

proximal to the carotid bifurcation, but not in the carotid sinus. Intima-medial thickness was unrelated to OSI in both regions;

- Hoi et al. (2011) concluded that the OSI and the RRT could explain changes in plaque distribution as a result of changes in flow conditions whilst TAWSS could not;

- According to Zhang et al. (2012), both TAWSS- and OSI-based risk factors were good predictors of subsequent stenosis, but the OSI-based risk factor was more effective;

- Knight et al. (2010) and Rikhtegar et al. (2012) found that the largest number of plaque locations could be predicted using a low TAWSS threshold, but that the OSI and RRT produced fewer false negatives.

Table 2.3 provides an overview of the conclusions presented in the selected articles. Most stated that their results were in agreement with the low/oscillatory shear theory, but five (18.5%) could not find a significant overall relationship between a flow-related metric and early atherosclerosis (Steinman et al., 2002; Joshi et al., 2004; Gijsen et al., 2007; Augst et al., 2007; van der Giessen et al., 2010).

2.3.2 Different and sometimes conflicting levels of data reduction were required to reach a conclusion

2.3.2.1 Descriptive analysis

In the two earliest papers that satisfied all selection criteria, by Perktold and Resch (1990) and Perktold et al. (1991), the comparison of flow and disease was essentially descriptive: differences in plaque location in carotid bifurcations with different bifurcation angles (De Syo, 1990) could be explained by differences in the extent and location of a recirculation zone. Such an analysis does not provide any statistical evidence for the relation between WSS and atherogenesis. De Syo et al. (2005) later presented a slightly more quantitative argument.

2.3.2.2 Visual comparison of maps

Many articles provided maps of flow-related parameters and of disease indicators (or explicitly referred to figures in companion papers for the latter), and then visually compared these distributions (Taylor et al., 1998; Goubergrits et al., 2002; Buchanan et al., 1999, 2003; Gijsen et al., 2007; Olgac et al., 2008, 2009; Suo et al., 2008; Zhu et al., 2009; van der Giessen et al., 2010; Hoi et al., 2011). This approach generally led to a conclusion in favour of the low/oscillatory shear theory. In many cases, however, not all the information available in these maps was used:

- Goubergrits et al. (2002) reported a good correlation between locations of wall alteration and regions of low WSS but their maps show a far from perfect agreement; plaques can also be seen in regions of high WSS (e.g. figure 1 - flow dividers of 7L and 22R), and many low WSS regions appear plaque-free (e.g. figure 1 - 1R);

- The images in Buchanan et al. (1999, 2003) also suggest that a one-to-one correlation does not exist. A spatial coincidence of low TAWSS and high OSI with early atherosclerotic lesions was noted, but (for example) a patch of lesions upstream of the coeliac branch seems to correspond to a region of high TAWSS and low OSI;

- Although Hoi et al. (2011) advocated the use of RRT as a surrogate marker of atherosclerosis, they conceded this metric failed to predict the absence of plaques in the proximal descending thoracic aorta of Lldr-/- mice;
- It should also be noted that in the study of Suo et al. (2008), the labelling of branches was inadvertently transposed in one map but not in the other (personal communication); clearly the degree of correlation needs re-examination.

It cannot be overemphasised that approaches which single out some observations whilst disregarding others may oversimplify the relation between flow and disease.

2.3.2.3 Point-by-point comparison

Quantitative point-by-point comparison is a more rigorous form of analysis. Steinman et al. (2002), Joshi et al. (2004), Wentzel et al. (2005), Gijsen et al. (2007) and Augst et al. (2007) performed point-wise comparisons of WSS with intimal, intima-medial or wall thickness. Spatial resolution varied from summary measures for each 1.5 mm-wide rectangular patch (Augst et al., 2007) to one data point per node on the surface of the finite element mesh (Steinman et al., 2002). Importantly, none of these studies found a significant correlation.

2.3.2.4 Axial averaging

A study by Wentzel et al. (2005) was one of those in which a point-by-point comparison did not yield the expected inverse relationship between wall thickness and WSS. The authors went on to average the data in the axial direction. They argued that this approach should be used in studies (such as theirs) where WSS is computed for the geometry of the diseased vessel but used to explain the initiation of disease, since it will reduce the effect of variations in luminal shape or size which would not have occurred in the disease-free vessel. An inverse relation between WSS and disease was obtained.

This technique also resulted in a significant inverse WSS-intimal thickness relation for Krams et al. (1997), but not for van der Giessen et al. (2010). In a related

technique, Joshi et al. (2004) eliminated axial variation by normalising the data per cross-section; as already noted, they found a significant inverse WSS-intimal thickness correlation in only one out of four cases.

2.3.2.5 Circumferential averaging

Although Wentzel et al. (2003) advised against the use of circumferential averaging of the data, since it obscures curvature-induced circumferential variations in WSS, Chatzizisis et al. (2008), Koskinas et al. (2010) and Samady et al. (2011) obtained a significant inverse correlation using this technique.

2.3.2.6 Selective analysis

A number of articles limited their analysis to a subset of the data. Details of their exclusion criteria are crucial in determining the implications of this selectivity. The pre-selection was based either on geometrical features or on values of shear- or disease-metrics.

- Augst et al. (2007) only measured intima-medial thickness along the posterior wall of the carotid bifurcation, and their analysis was therefore limited to this region. It is unclear if this would have influenced the results;
- Wentzel et al. (2003, 2005), Chatzizisis et al. (2008, 2011) and Koskinas et al. (2010) excluded data from regions of branching;
- Zhang et al. (2012) visually preselected locations of low TAWSS and high OSI, and then performed a more quantitative analysis on the subset;
- Chatzizisis et al. (2008, 2011) and Koskinas et al. (2010) analysed only segments with uniform intima-medial thickness and WSS.

In these cases, the pre-selection will have restricted variation in shear stress or in disease severity and may therefore have obscured important aspects of the relation between WSS and disease.

2.3.2.7 Thresholding

Although most articles did not specify a threshold below or above which a haemodynamic factor was believed to promote atherosclerotic disease, five articles presented their haemodynamic results in such a categorical sense. (Note this is different from the approach of Zhang et al. (2012), described above, who used thresholding to include or exclude data, rather than for the analysis itself.)

- Koskinas et al. (2010), who studied flow in porcine coronary arteries, fixed the WSS threshold at 1.2 Pa, a value previously used in a study of flow in human coronaries (Stone et al., 2007). However, since allometric arguments show that WSS depends strongly on body weight (Weinberg and Ethier, 2007), it may be unwise to use the same WSS threshold across species;

- In a second paper by the same group Chatzizisis et al. (2011), once again using porcine coronary arteries, a slightly different threshold (1 Pa) was chosen;

- Samady et al. (2011), in a study in human coronary arteries, defined "low TAWSS" as < 1 Pa and "high TAWSS" as ≥ 2.5 Pa, with "intermediate TAWSS" in between, on the basis of "previous cell culture, experimental, and human data".

The concern with such studies is that the significance of the result could depend on the choice of threshold, and that no strong *a priori* case exists for any particular value. A better approach might be that of Knight et al. (2010) and Rikhtegar et al. (2012) who dichotomised haemodynamic variables by balancing the number of correctly predicted plaque locations and false positives for ten patients. This is a sensible approach if no other information is available to estimate the threshold level.

To summarise, straightforward point-by-point comparisons did not yield the expected results. Although averaging did tend to produce significant results, averaging techniques advised against by some groups were essential for others' analyses. Preselection of data may have restricted the range of shears and disease severities that were considered and hence have limited the validity of the conclusions. Thresholding

of haemodynamic parameters needs to be based on objective criteria; furthermore, the categorical approach and the continuum approach represent different interpretations of the low shear theory - only mechanistic studies can determine which (if either) is correct.

2.3.3 Blood flow was assessed at different stages in the disease process

Small changes in geometry can induce significant alteration of WSS (Cheer et al., 1998; Vincent et al., 2011). The validity of studies which investigate arterial blood flow therefore depends on the anatomical fidelity of the reconstructed vascular geometry.

2.3.3.1 Subject-specific studies

Single geometry per subject Studies of human vessels have often used the same geometry for the assessment of disease and for the computation of WSS. Obviously, lesions have to be present in the segment in order to allow such an investigation. In some cases, the geometry was obtained from individuals who were free of cardiovascular symptoms or, *post mortem*, from individuals whose primary cause of death was not cardiac-related (Steinman et al., 2002; Joshi et al., 2004; Augst et al., 2007). On the other hand, many studies used subjects with known atherosclerosis, such as patients who went to clinic with a lesion requiring physiological evaluation or treatment (Krams et al., 1997; Goubergrits et al., 2002; Wentzel et al., 2003, 2005; Gijsen et al., 2007; van der Giessen et al., 2010).

In studies of this type, there is an explicit or implicit reliance on compensatory remodelling (Zarins et al., 1987) to ensure that the presence of lesions did not alter the disease-free geometry (Feldman et al., 2006). In the absence of compensatory remodelling, this approach could obscure an inverse correlation between early atherosclerosis and WSS since a narrowed lumen leads to an increase in velocity (for the same flow rate).

Virtual plaque removal The concept of removing plaques virtually from diseased geometries is attractive. Olgac et al. (2008, 2009), Knight et al. (2010) and Rikhtegar et al. (2012) used an image-based approach for virtual plaque removal but acknowledged the potential for under- or overestimating the size of the healthy lumen. They also pointed out that a validation study would not be trivial, with one of the challenges being the registration and establishment of point-to-point correspondence in datasets acquired several years apart, possibly on different scanners.

Longitudinal studies Samady et al. (2011) were the only authors in the final selection to report a longitudinal study in human subjects: they rescanned each person 6 months after the first examination. However, this study focused on progression rather than initiation of disease: the baseline geometries were taken from patients rather than healthy volunteers. Longitudinal studies are easier in animals, but again the focus has been on progression rather than initiation (Chatzizisis et al., 2008, 2011; Koskinas et al., 2010).

2.3.3.2 Multiple group studies

A different option is to abandon the patient- or animal-specific approach. Instead, the lesion distribution is assessed in a group of diseased vessels, blood flow is simulated in geometries obtained from a group of healthy vessels, and the comparison is performed between group means. Each group needs to have a large enough size to make inter-subject variation unimportant. In most of these studies, however, the haemodynamic group was limited to just one geometry (Perktold and Resch, 1990; Perktold et al., 1991; Taylor et al., 1998; Buchanan et al., 1999, 2003; Suo et al., 2008; Hoi et al., 2011); only Zhu et al. (2009), using mice, performed a full statistical comparison.

In summary, there have been no longitudinal studies that examined the initiation of disease in people. Instead, researchers have focused on progression, or have made assumptions about the nature of vascular remodelling, about how to remove lesions virtually, or about inter-subject variation. The high sensitivity of WSS to geometry

makes the validity of these assumptions critical. All five studies that failed to find a relation between flow metrics and early lesions used the diseased geometry for flow mapping. However, not all studies using this technique failed to find a relation.

2.3.4 Disease localisation was assessed at different stages in the disease process

Atherosclerosis was mapped through the identification of one or more of its constituents or by measuring geometric anomalies in wall and/or luminal dimensions. Some studies investigated the likelihood that lesions will occur at a particular level of WSS whereas others investigated the severity of the disease in relation to shear.

2.3.4.1 Disease assessment based on lesion composition

Lipid staining Recognising that the onset of atherosclerosis is characterised by lipid accumulation in the inner wall (Anitschkow, 1933), a number of research groups made use of lipid staining with oil red O or Sudan IV to identify the earliest stages of the disease. This technique was applied in the studies of Taylor et al. (1998), Goubergrits et al. (2002), Suo et al. (2008), Chatzizisis et al. (2008, 2011) and Hoi et al. (2011) or their companion studies. However, it has been argued that not all fatty streaks identified using this technique, turn into atheromatous plaques.

Calcium scoring As the disease progresses, other plaque components appear. Olgac et al. (2008, 2009), Knight et al. (2010) and Rikhtegar et al. (2012) focused on the calcium content of the wall, which they obtained by Computed Tomography (CT). Disadvantages of this method are that it cannot locate non-calcified plaques and that the calcified areas may not exactly match the locations where the disease was initiated because of the continuous interaction between flow and the development of the disease. In addition, calcification without atherosclerosis is possible; confirmation of automatically identified plaques by an experienced clinician, as was carried out in the studies by Knight et al. (2010) and Rikhtegar et al. (2012), is therefore important.

2.3.4.2 Disease assessment based on geometric changes

The companion papers of Perktold and Resch (1990), Perktold et al. (1991) and Buchanan et al. (1999, 2003) focused on luminal narrowing, identified by surgical observation or from vascular casts, respectively. However, early wall thickening might be invisible to these techniques, due to compensatory remodelling. Hence, a large number of the selected articles opted to use intimal, intima-medial or wall thickness as a measure of disease. Joshi et al. (2004), Zhu et al. (2009) and Chatzizisis et al. (2011) or their companion papers made use of *post mortem* preparations, sometimes in combination with histological stains such as Verhoff elastic-trichrome to assess thickness.

Imaging techniques such as Magnetic Resonance (MRI; Steinman et al. (2002); Zhang et al. (2012)), ultrasound (US; Augst et al. (2007)) and intravascular ultrasound (IVUS; Krams et al. (1997); Wentzel et al. (2003, 2005); Gijsen et al. (2007); Chatzizisis et al. (2008); van der Giessen et al. (2010); Koskinas et al. (2010); Samady et al. (2011); Siogkas et al. (2011)) can be used for the same purpose *in vivo*, allowing subject-specific studies of the relation with flow. There are disadvantages, however. With intima-medial and wall thickness, it is not possible to distinguish between intimal thickening due to atherosclerosis and medial thickening in response to elevated blood pressure (Augst et al., 2007). Adaptive intimal thickening unrelated to atherosclerosis and medial thinning under lesions may also cause problems.

2.3.4.3 Probability-of-occurrence versus plaque severity

Studies of the relation between flow and disease have variously investigated whether or not atherosclerotic lesions occur in certain haemodynamic environments (Buchanan et al., 1999, 2003; Goubergrits et al., 2002; Olgac et al., 2008, 2009; Hoi et al., 2011; Siogkas et al., 2011), or how likely it is to find lesions in these regions (Taylor et al., 1998; Suo et al., 2008; Knight et al., 2010; Zhang et al., 2012), or have interpreted the low/oscillatory shear theory in a dose-dependent way by asking whether disease is more advanced in these regions (Krams et al., 1997; Steinman et al., 2002;

Wentzel et al., 2003, 2005; Joshi et al., 2004; Gijsen et al., 2007; Augst et al., 2007; Chatzizisis et al., 2008, 2011; van der Giessen et al., 2010; Koskinas et al., 2010; Zhu et al., 2009; Samady et al., 2011).

For completeness it should be noted that an additional category of articles have addressed a slightly different question by asking if certain haemodynamic conditions can protect against the disease (Knight et al., 2010; Rikhtegar et al., 2012).

In summary, a variety of techniques were used to assess the localisation of atherosclerotic disease. Whereas lipid staining will have picked up early signs of atherosclerosis, this is not the case for approaches involving calcium scoring or luminal narrowing. Moreover, measurements of intimal, intima-medial and wall thickness cannot specifically identify intimal thickening due to atherosclerosis; the five articles which did not find a correlation between WSS and atherogenesis used these methods, although some articles using these methods (e.g. Krams et al. (1997) and Wentzel et al. (2003, 2005)) did find a relation. Finally, it is not clear if the low/oscillatory shear theory should be interpreted in terms of the frequency or severity of disease, or whether both measures are satisfactory.

2.4 Discussion

The low shear stress theory was heterodox when first proposed. It challenged the prevailing high shear stress theory, which appeared to account for the pattern of disease observed in various non-human species and which was associated with the intuitively-appealing mechanistic hypothesis that high shear stress damages the endothelium, allowing excessive entry of plasma lipoproteins into the wall.

The involvement of oscillatory shear emerged from the studies of Ku et al. (1985), who examined lesion distributions in *post mortem* human arteries and used laser Doppler anemometry to measure velocity profiles in anatomically-accurate models of those arteries. Indeed, the relation between intimal thickness and OSI was much stronger than that between intimal thickness and mean shear. Today the

low/oscillatory shear theory is widely regarded as having been established, and it is contrary views that are regarded as heterodox.

The present systematic review considers whether the evidence justifies that consensus. It has focused on studies that employed CFD to assess patterns of wall shear because these are currently the most reliable methods. (Recent improvements in the accuracy of flow measurement by MRI (Stalder et al., 2008) and other techniques (Poelma et al., 2012) may change this in the near future.)

Despite the robust methodology, it is not impossible that some relevant papers were overlooked. Nevertheless, reliable conclusions can be drawn from those that were reviewed. First, not all studies supported the low/oscillatory shear theory. Second, some found the same relation to disease for low WSS and OSI, but others did not. Third, although many claim that their results do support the low/oscillatory shear theory, they interpret the theory in different ways: a variety of metrics have been used to represent the disease distribution; they have been compared to a range of haemodynamic factors; data reduction techniques used by different research groups contradict each other and limit the range of shears or disease severities under consideration; and WSS has been treated as a continuous or a categorical variable. The theory may very well be true but - taken together - the evidence for it is less clear-cut than might at first appear.

The five studies that failed to find a significant relation between low WSS and disease are naturally of particular interest. They all used a single geometry to assess both disease severity and flow, and they all used wall thickness-related metrics as an index of disease severity. It is tempting to discount them on these grounds, but other studies using these methods did find a correlation. It could equally be claimed that these five are methodologically the best studies because they used a quantitative, point-by-point comparison between the two variables, thus avoiding subjective visual assessment, cherry picking of particular shear or lesion areas, or unwarranted averaging.

A number of issues will need to be addressed by future studies in order to improve

and refine the existing evidence.

2.4.1 Are we capturing the relevant flow metrics?

Do the conventional metrics - WSS, TAWSS, OSI and RRT - capture physiologically-relevant features of the flow? And do they quantify the essence of the expression *disturbed flow* that is so commonly used in the biological literature? Or should we explore other parameters, such as the directional oscillatory shear index suggested by Chakraborty et al. (2012)? The use of *in vitro* models investigating the response of endothelial cells to various flow conditions (Potter et al., 2011; Chakraborty et al., 2012) and *in vivo* models with modified flow conditions (Cheng et al., 2006; Hoi et al., 2011) can provide valuable insights into this issue.

A number of authors have suggested an indirect link between flow and disease that depends on flow affecting fluid-phase mass transport of solutes (oxygen, LDL) near the wall, rather than direct effects of flow on the wall itself (Ma et al., 1997; Olgac et al., 2008, 2009, 2011). WSS and transport are related, but idealised models show that their patterns need not be identical (Coppola and Caro, 2008; Van Doormaal and Ethier, 2010).

2.4.2 What level of data reduction is required and justifiable?

The use of different levels of data reduction complicates the evaluation of the evidence for shear-related theories of atherosclerosis. Since the nature of the relation between early atherosclerosis and blood flow is still not fully understood, authors should make it possible for readers to evaluate results after minimal processing, for example by providing figures that allow a visual comparison, even when statistics are applied only to reduced measures.

Point-by-point comparisons represent an ideal. Nevertheless, there remain limits to the spatial resolution that can be attained. In particular, cross-correlation

between adjacent data points must be minimised to prevent over estimation of statistical significance. Errors in image registration are also limiting.

2.4.3 Are subject-specific studies introducing errors?

Studies of the effects of WSS on the initiation of atherosclerosis should compute flows using geometries that represent the disease-free vessel. However, the large effect that small changes in geometry can have on WSS patterns suggests that haemodynamic theories of disease are best investigated in a subject-specific manner. Currently, these two requirements are hard to reconcile: they require either that effects of disease on geometry are negated naturally (by compensatory remodelling) or removed artificially (by hard-to-validate "virtual" techniques), or that longitudinal studies are carried out over periods of years.

These problems could be resolved by the development of techniques that allow disease to be mapped at a stage before intimal thickening occurs, and by methods that could ethically be used in such minimally-affected subjects. Until such techniques are available, it may be more appropriate to drop the subject-specific approach and instead use different study groups: a diseased one for the assessment of lesion patterns and a disease-free one for the assessment of flow. The essential requirement of sufficiently large samples in the haemodynamic group has been fulfilled in only one study of those reviewed, and in none of those that considered human vessels.

2.4.4 Have all disease distributions been considered?

What is not readily apparent from the articles discussed in this review is that disease distributions reported in the literature sometimes seem mutually contradictory from a haemodynamic point of view. This for instance led to the original debate between the high and low shear theories: Fry (1969) observed aortic lesions at the downstream margin of side branches, a site that Caro et al. (1971) found to be spared of disease. As both theories assumed that this site is characterised by high WSS, the debate concerned the distribution of lesions rather than the characteristics of blood flow.

Since the high shear theory was predicated on the distribution seen in animal models while the low shear theory was based on a study in human *post mortem* specimens, the discrepancy was attributed to differences in plasma cholesterol levels (Caro et al., 1971; Getz and Reardon, 2012). However, it has emerged that lesion patterns change with age in rabbit and human aortas, and in a parallel way (Weinberg, 2002); the discrepancy might better be explained by such changes. Lesions can also show different patterns in one species at a single age. In the mouse, they occur upstream of branches originating in the aortic arch, all around branches of the thoracic aorta, and downstream of branches in the abdominal aorta (McGillicuddy et al., 2001; Nakashima et al., 1994).

The different patterns provide an additional challenge for haemodynamic theories of atherogenesis, as do a number of unexpected experimental observations. For example, occluding a renal artery, which should essentially abolish its effect on aortic WSS, did not affect the lesions seen downstream of the branch ostium in cholesterol-fed rabbits (Roach and Fletcher, 1976); these can instead be suppressed by placing a cuff around the aorta, to prevent its normal cyclical stretch (Thubrikar et al., 1990).

2.5 Conclusion

Low and/or oscillatory wall shear stress is widely assumed to play a causal role in the initiation and development of atherosclerosis. However, a systematic review of papers which compare the localisation of atherosclerotic lesions with the distribution of haemodynamic indicators, shows that, although many articles claim their results conform to the theory, it has been interpreted in different ways. A range of metrics have been used to characterise the distribution of disease, and they have been compared to a range of haemodynamic factors. Several studies, including all of those making systematic point-by-point comparisons of shear and disease, failed to find the expected relation. The various pre- and post-processing techniques used by different groups to reduce the level of complexity are often mutually incompatible. Finally, such studies have investigated only a subset of the known patterns

of disease. Taken together, the evidence for the low/oscillatory shear theory is less robust than commonly assumed. Further longitudinal studies starting from the healthy state, or the collection of average flow metrics derived from large numbers of healthy vessels, both in conjunction with point-by-point comparisons using appropriate statistical techniques, are necessary to improve our understanding of the relation between atherogenesis and blood flow.

Chapter 3

Geometric analysis of the rabbit aorta and association with age

Small changes in vascular geometry can considerably affect the characteristics of blood flow and resulting distributions of WSS (Cheer et al., 1998; Vincent et al., 2011). When studying the relationship between atherosclerotic disease and WSS by means of CFD, geometric accuracy of the vascular geometries in which the simulations are performed is therefore crucially important. Since this thesis involves the analysis of blood flow in thoracic aortas of immature and mature rabbits, the current chapter presents the development of a dataset of anatomically realistic immature and mature rabbit thoracic aortic geometries. Geometric differences between the two age groups are analysed, and the accuracy of the dataset and resulting findings are investigated.

Section 3.1 starts with an overview of techniques that can be used to acquire three-dimensional vascular geometries. The methods used as part of the work presented here to capture the aortic geometry of immature and mature rabbits are detailed in section 3.2. Section 3.3 subsequently compares the aortic geometries of the two age groups, since differences may affect the governing flow dynamics in the respective age groups. Section 3.4 discusses the results, assesses the advantages and drawbacks of the applied reconstruction technique and suggests ways to evaluate or address potential deficiencies. Finally, section 3.5 investigates artefacts which may

affect the geometric accuracy of the reconstruction approach adopted for this thesis.

3.1 Acquisition of 3D vascular geometry: overview

Methods for acquiring vascular geometries can be subdivided into two categories:

- *In vivo* imaging;
- *Post mortem* techniques.

Popular *in vivo* imaging modalities yielding structural and morphological information are computed tomography (CT), which exploits differences in absorption of X-rays to characterise tissues, ultrasound (US), which uses high-frequency sound waves to view soft tissues, and magnetic resonance imaging (MRI), which uses a magnetic field to align the nuclear magnetisation of hydrogen atoms in the body (Giordana, 2004). *In vivo* imaging by CT is considered inherently dangerous due to the subject's exposure to radiation, which increases the risk of cancer. While US can be done non-invasively, the invasive Intra-Vascular variant (IVUS), for which the US probe is inserted in the vessel of interest via a catheter, yields higher-resolution images of less superficial vessels such as coronary arteries. (Using this technique imaging of the pullback, e.g. by angiography, is required to obtain 3D information.) MRI is also non-invasive, but is very costly (Giordana, 2004).

Post-mortem techniques for vessel reconstruction include pressure fixation, which terminates any ongoing biochemical reactions while maintaining the physiological pressure, and *in situ* vascular casting, which involves the injection of a curing material into the subject's vascular system. The *post mortem* preparation is subsequently scanned to obtain an *in silico* model. As pressure fixation does not perfectly fix the dimensions of the blood vessels, casting is generally preferred (Moore et al., 1999). However, a cast is not necessarily an exact representation of the vascular geometry either, since its dimensions can be affected by inappropriate transmural pressures, active changes in vessel dimension due to cellular elements and shrinkage of the casting material (Kratky et al., 1989).

Although at first sight *in vivo* techniques seem preferable since they allow follow-up (Moore et al., 1999; Vandeghinste et al., 2011) and do not suffer from effects such as resin shrinkage, *in vivo* methods too have disadvantages. Firstly, the obtained resolution is limited because of interference from surrounding tissues and artefacts caused by subject movement (due to the long scanning times), breathing and the heartbeat. Moore et al. (1999) used voxels with in-plane dimensions of 312.5 µm and an out-of-plane dimension of 1000 µm for their *in vivo* MR images, whereas their *post-mortem* preparations were reconstructed using CT with isometric voxels of 100 to 200 µm. Pro- and retrospective cardiac and respiratory gating have been used to enhance image quality (Vandeghinste et al., 2011).

The image contrast is generally worse with *in vivo* compared to *ex vivo* scanning. The use of contrast agents can improve the quality of the scans, but the required volume of contrast agent can be very large in physiological terms, especially in the case of small laboratory animals, leading to hypervolaemia, stretch of the vessels and hence unrealistic geometric models. As an example, Vandeghinste et al. (2011) noted that the minimal dose of CT contrast agent (Fenestra VC-131, Advanced Research Technologies Inc., Saint Laurent, Canada) needed to obtain sufficient contrast accounted for 25% extra blood volume in mice. Finally, in animals, the use of anaesthesia introduces (unknown) changes in blood pressure and vessel resistance (Lukasik and Gillies, 2003). In the knowledge that blood pressure fluctuations of 44 mmHg cause aortic diameter changes of 11.3% in healthy adults (Yap et al., 2008), anaesthetising a subject will undoubtedly affect its arterial dimensions.

In conclusion, none of the currently available methods for 3D vascular reconstruction is perfect. In the work presented here, the casting approach was chosen to acquire the aortic geometry of immature and mature rabbits. In addition, the accuracy of the casting technique was investigated in detail (section 3.5).

3.2 Methods

The aortic geometries of immature and mature rabbits were reconstructed by micro-CT of vascular corrosion casts, and the characteristics of the two age groups were subsequently compared. This section details the approach for vascular reconstruction and describes the methods for geometric characterisation and comparison.

3.2.1 Animals

A total of seven immature and six mature male New Zealand white rabbits (HSDIF strain; Harlan, Bicester, Oxford, UK) were used in this study, but results from only five immature and five mature rabbits were included in the geometric analysis, for reasons detailed below. These numbers include the mature animal for which flow data were presented by Vincent et al. (2011). Ages and weights of the individual animals are listed in table 3.1. All animal procedures complied with the Animals (Scientific Procedures) Act 1986 and were approved by the local ethical review panel of Imperial College London.

3.2.2 Vascular corrosion casting

Each rabbit received heparin (2000 USP units, intravenously/IV) and was subsequently euthanised with an overdose of sodium pentobarbitone (Euthatal; Rhône Mérieux, Harlow, Essex, UK, 0.8 ml/kg, IV). After placing the animal in a supine position, the thorax was opened midline along the sternum and the pericardium was perforated. A cannula, connected to a 50 ml syringe and a manometer, was inserted in the left ventricle of the heart and the arterial system was flushed through with 0.9% w/v saline. A Batson's #17 methyl methacrylate resin mixture (Polysciences, Inc.) of the following composition was prepared:

- 2x50 ml monomer base solution
- 20 ml catalyst
- 12 drops of promoter

Table 3.1: Details of the subjects used for vascular corrosion casting, voxel sizes of the corresponding micro-CT scans and hydraulic diameter D_0 at the aortic root, with mean±SD for each age group. Age is expressed in weeks (w) or months (m). Cast AAEH081013 was taken from (Vincent et al., 2011).

Rabbit ID (short)	**Rabbit ID (long)**	**Age group**	**Age**	**Weight (kg)**	**Voxel size (µm)**	D_0 **(mm)**
A	VPADP100209	Immature	11.1 w	1.83	44.7	3.35
B	VPADP100324a	Immature	9.9 w	1.85	48.6	3.97
C	VPADP100426b	Immature	11.3 w	1.83	48.6	3.42
D	VPADP110713a	Immature	9.3 w	1.58	47.9	3.44
E	VPADP100324b	Immature	9.9 w	2.02	49.8	5.62
Immature			10.3 ± 0.860 w	1.82 ± 0.157	47.9 ± 1.93	3.96 ± 0.960
F	AAEH081013	Mature	18 m	3.25	55.2	5.84
G	VPADP091210	Mature	9.5 m	3.24	47.7	4.32
H	AAEH091110	Mature	7.6 m	3.85	49.3	4.47
I	VPADP091214	Mature	9.1 m	3.76	53.3	4.94
J	VPADP100713	Mature	8.7 m	4.27	49.6	6.59
Mature			10.58 ± 4.21 m	3.67 ± 0.436	51.0 ± 3.11	5.24 ± 0.963

A small amount of pigment was added to give the resin a deep red colour. After 35 minutes of intermittent stirring the resin mixture was hand injected through the cannula into the vascular system. The infusion pressure was kept at 90 mmHg for immature and 100 mmHg for mature rabbits, corresponding to mean physiological blood pressures for these age groups (Owen, 1986). During the procedure tap water was trickled into the chest cavity to provide cooling for the exothermic reaction. Resin was injected until it was no longer possible to inject any more resin or up to a maximum of 100 ml, after which the cannula was clamped. The cast was then left to cure overnight. After curing, the rabbit was submerged in a 25% w/w KOH bath to corrode for a period of 2 weeks. The cast was subsequently rinsed with water. If a large number of bone particles remained on the cast, the cast was sprinkled with a 20% HCl solution and left for a minimum of 4 hours, and subsequently rinsed with water. Otherwise, remaining bone particles were removed manually. The cast was washed with a strong alkaline detergent (Decon 90, Decon Laboratories Ltd) and rinsed again with water. Two casts were rejected because the injection pressure could not be maintained, and a third cast because of the presence of a large air bubble on the luminal surface of the descending aorta. Larger veins and distal arteries were removed from the cast so as to make the specimen fit into a ⌀9 cm cardboard tube. This was done using a range of cutting tools and a Dremel 400 Series (cut-off wheel 22 × 0.06 mm). Finally, the cast was washed once more with water.

3.2.3 Micro-CT scanning

Each cast was mounted in a ⌀9 cm cardboard holder and scanned using a Metris X-Tek HMX-ST CT Scanner (Natural History Museum, London), with the aorta approximately in line with the rotation axis of the scanning manipulator. The ascending aorta, the aortic arch with at least its first generation of branches and the descending thoracic aorta with at least five intercostal branch pairs were selected as the region of interest. A voxel size of 50 µm was targeted, since a close-up scan of an intercostal branching region at half this voxel size did not reveal any smaller

geometric details. The exact voxel dimensions for each cast can be found in table 3.1. Each scan produced 3142 projections of the region of interest. The scan data were reconstructed using CT-Pro (Nikon Metrology, Tring, UK), with automatic calculation of the centre of rotation, and extracted as DICOM files using VGStudio Max 2.1 (Volume Graphics GmbH, Heidelberg, Germany). This resulted in a stack of approx. 2000 DICOM images with 2000×2000 pixels. Each stack corresponded to approx. 9 GB of data.

3.2.4 Image segmentation

After cropping to the region of interest, the image stacks were thresholded according to the following protocol. For four images in each stack, distributed evenly along the stack, grey values on a line intersecting a vessel of interest were plotted using ImageJ, a Java-based image processing software (Rasband, 1997-2011). An example is shown in figure 3.1. For all eight edges the middle grey value was determined. The average of these values was selected as the threshold value for the complete image stack. Note that in general, the transition region covered approx. 2 to 4 pixels (approx. 100-200 µm), determining the spatial resolution of the image.

Once the threshold value was determined, the DICOM images were segmented using Amira 5.2.2 (Visage Imaging, Inc.). Only the region including the ascending aorta, the aortic arch with at least its first generation of branches and the descending thoracic aorta with five intercostal branch pairs was retained. (Note that in some cases only a single intercostal artery was present instead of the most proximal intercostal pair.) Artefacts introduced during the casting procedure, such as the presence of bubbles and bone particles, were corrected at this stage by changing the fate of the corresponding voxels.

In order to assess the accuracy of the thresholding method, a phantom with known bore dimensions ($\varnothing 2.00 \pm 0.02$ mm) was scanned together with a cast that was made from the same resin mixture batch. After reconstruction of the phantom using the thresholding protocol and a marching cube algorithm (Lorensen and Cline, 1987) with constrained smoothing (Amira 5.2.2; Visage Imaging, Inc.), the bore diameter

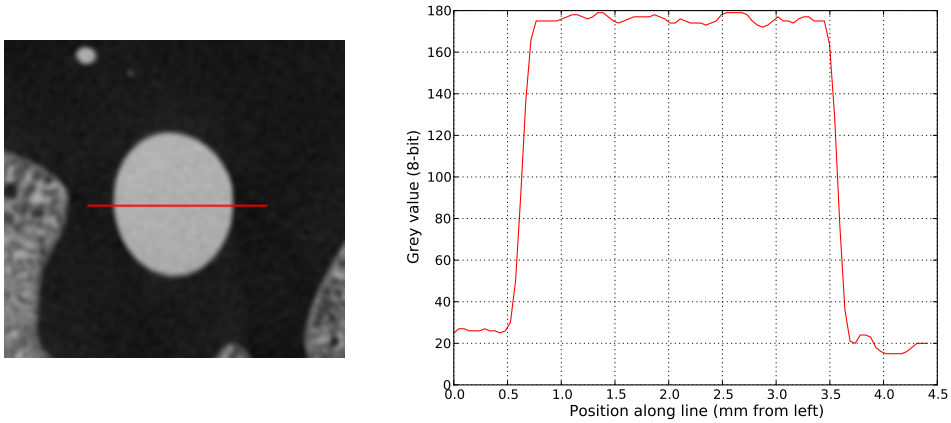

(a) (b)

Figure 3.1: Determining the segmentation threshold value: (a) Close-up of an aortic cross-section in a DICOM image obtained from scanning a vascular corrosion cast; (b) plot of the grey values along the line indicated in (a).

was estimated at 1.984 mm. Measurements were performed using Rhinoceros 4.0 (Robert McNeel & Associates, Seattle, USA). As the error (16 µm) is smaller than the voxel size of the 3D image (approx. 50 µm for each scan, table 3.1), the test suggests that the thresholding method does not introduce any errors. However, scanning artefacts influence grey values locally and might therefore still benefit from a locally varying rather than global threshold value.

Sensitivity of the cast dimensions to the threshold choice was further estimated by computing and comparing the hydraulic diameters of vessel segments for a range of threshold values. Three vessel segments of the cast denoted VPADP100209 were selected:

- Segment 1: the aortic segment between the fifth and sixth intercostal pairs;
- Segment 2: a segment of the left common carotid artery;
- Segment 3: a segment of the left superior intercostal artery.

Note that the segments are sorted by decreasing mean hydraulic diameter. The value of the threshold was varied within a range (TV1 = 13915 to TV4 = 14715) around

Table 3.2: Sensitivity of the absolute hydraulic diameter of cast vessels to the threshold value used for segmentation. The hydraulic diameter calculated using the original threshold TV was compared to the hydraulic diameter calculated using the threshold values TV1-TV4. For each segment the table gives the number of slices in which the difference between both diameters is larger than 50 µm, together with the total number of slices in that segment. The locations of the segments are listed in the text.

Segment ID	**TV1**	**TV2**	**TV3**	**TV4**
1	4/145	0/145	0/145	5/145
2	0/96	0/96	0/96	0/96
3	0/29	0/29	0/29	0/29

Table 3.3: Sensitivity of the relative hydraulic diameter of cast vessels to the threshold value used for segmentation. The hydraulic diameter calculated using the original threshold TV was compared to the hydraulic diameter calculated using the threshold values TV1-TV4. For each segment the table gives mean (maximum) differences as a percentage of the original hydraulic diameter. The locations of the segments are listed in the text.

Segment ID	**TV1**	**TV2**	**TV3**	**TV4**
1	0.48% (1.7%)	0.30% (1.5%)	0.38% (1.3%)	0.49% (1.9%)
2	0.96% (3.6%)	0.58% (2.5%)	0.61% (3.2%)	0.88% (3.6%)
3	0.17% (0.61%)	0.10% (0.37%)	0.10% (0.37%)	0.16% (0.74%)

the original threshold value TV (= 14315) corresponding to the uncertainty resulting from the threshold value calculation. The results are summarised in tables 3.2 and 3.3. Table 3.2 shows that the deviation in diameter outweighed the uncertainty introduced by the voxel size only seldomly. Table 3.3 shows that the relative changes in diameter due to variations in the actual threshold were limited and are therefore unlikely to affect WSS patterns.

3.2.5 *In silico* reconstruction

The thresholded luminal surface was extracted using the modified marching cube algorithm (Lorensen and Cline, 1987) with constrained smoothing in Amira 5.2.2 (Visage Imaging, Inc.), followed by an additional Taubin smoothing step[1] using the Vascular Modeling Toolkit (Antiga, 2010). The surface mesh was then truncated by trimming terminal branches at right angles. Finally, the mesh quality was improved by re-triangulation in Gambit 2.4.6 (ANSYS, Inc.) without changing the overall resolution.

3.2.6 Geometric characterisation and comparison

A vessel can be characterised geometrically by its centreline, a cross-sectional measure such as the hydraulic diameter at the aortic root, and the variation of this measure along the centreline.

For all geometries the centreline of the aorta was traced using VMTK (Antiga et al., 2003). The centreline was resampled using a spline filter (VMTK) to ensure that the centreline definition was given by a set of points with an inter-point spacing of $D_0/4$. A moving average smoothing filter was also applied to the set of centreline points to limit high-frequency noise in the distributions of centreline curvature and torsion. Curvature and torsion of each centreline were computed at the sampling points using VMTK. For statistical analysis of curvature and torsion between age groups, geometric centrelines were combined by matching consecutive sampling points, using the branching point of the brachiocephalic trunk (as determined with VMTK; Antiga and Steinman (2004)) as a datum.

To analyse tapering of the aortas, the radii of maximum inscribed spheres were computed at the aortic root, near the first intercostal branch pair (or corresponding

[1] A common method for smoothing meshes is Laplacian smoothing, a process which is also known as diffusion. Following this concept the vertices of a mesh are incrementally moved in the direction of the Laplacian. However, meshes subjected to Laplacian smoothing shrink. Taubin smoothing, also known as the $\lambda|\mu$ algorithm, relies on the use of two diffusion steps, one inwards and one outwards, to approximately preserve the volume of the mesh (Bray, 2004).

single branch), and near the fifth intercostal branch pair (VMTK). Taper between two locations, which is a measure for the rate of change of radius, was calculated as the arctangent of the difference in radii divided by the distance between the slices, measured along the aortic centreline.

3.2.7 Statistics

Unless stated otherwise, data are presented as means with their standard errors (SEM), which is the standard deviation of the sample-means estimate of a population mean. Evaluation of outliers was done using Chauvenet's criterion, which states that data points are rejected if the probability of obtaining their deviation from the mean is less than $1/(2s_{\mathrm{smp}})$, where s_{smp} is the sample size. For comparisons, $P < 0.05$ was used as the criterion of significance.

3.3 Results

3.3.1 Reconstruction of aortic geometries

Figure 3.2 shows an example of a vascular cast. The image illustrates that the resin entered a vast number of vessels, e.g. the vasculature of kidneys and lungs are clearly visible and also part of the venous side of the vascular system was cast. The quality of the casts can be assessed from the DICOM images, which were reconstructed from the CT projections. Figure 3.3 gives an example of a particularly problematic section. The speckled grey area represents a section through the cast. An air bubble, trapped between the setting resin and the vessel wall, has left its trace along the top edge of the section. The brighter spot on the DICOM image is the trace of a bone particle which stuck to the cast during scanning. As mentioned in section 3.2.4 such artefacts were corrected by hand in the segmentation phase.

Figure 3.4 shows the luminal surface reconstructions of the five immature and five mature rabbit aortas. All vessels are shown to the same scale. This was achieved by aligning the geometries in a common coordinate system by rigid image registration (IRTK, Ixico Ltd).

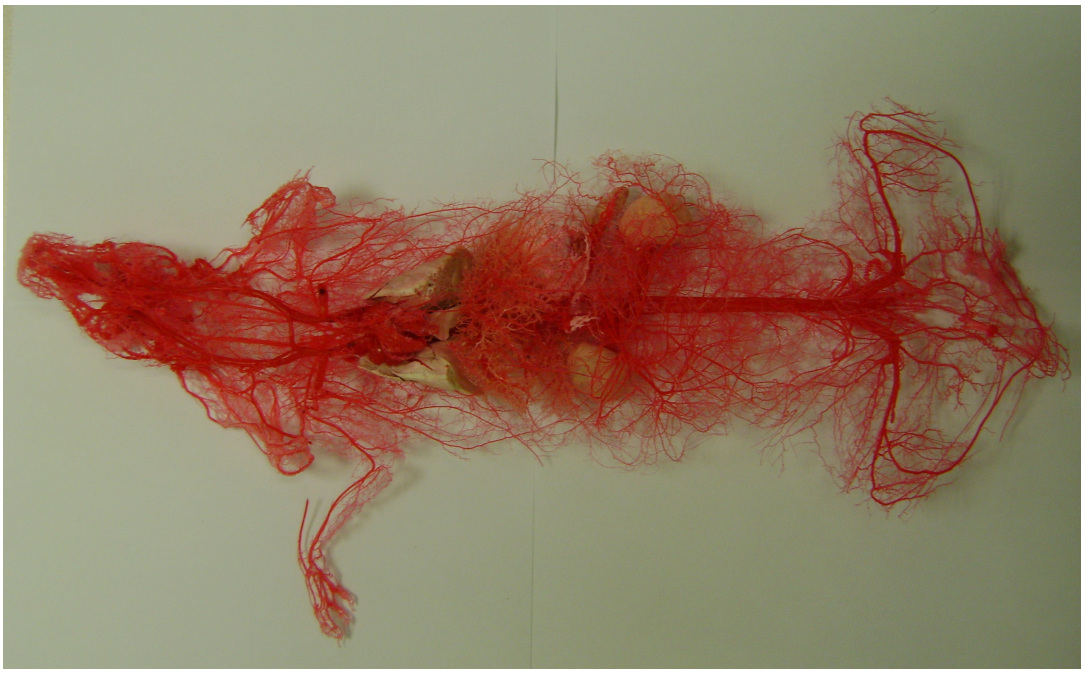

Figure 3.2: Vascular corrosion cast of rabbit AAEH091110.

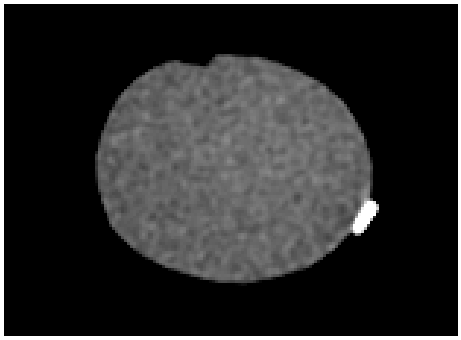

Figure 3.3: Example of a problematic DICOM image created by micro-CT of a vascular cast.

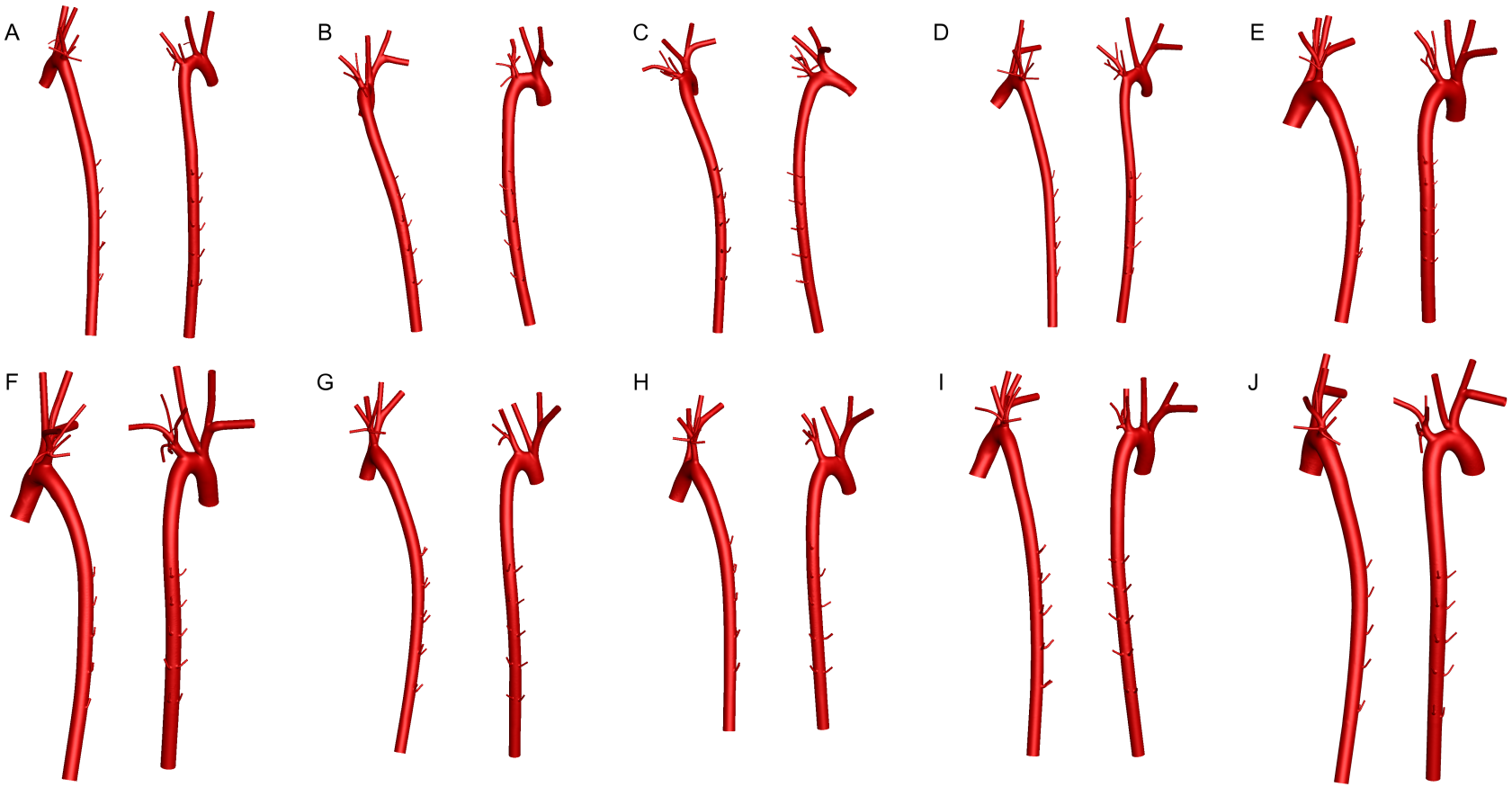

Figure 3.4: Reconstructions of proximal thoracic aortas of immature (A-E) and mature (F-J) rabbits. All vessels are shown to the same scale following rigid image registration (IRTK, Ixico Ltd). The letters refer to the short rabbit IDs as indicated in table 3.1. The geometry in F was taken from Vincent et al. (2011).

The reconstruction approach preserved small-scale features of the geometry, such as sharp branching angles and the cusp near the attachment site of the ligamentum arteriosum. Figure 3.5 shows close-ups of these features for the cast denoted VPADP091210.

3.3.2 Anatomic variability in aortic branching anatomy

The aortic branching anatomy varied between rabbits. Most striking was the variation in the branching configuration of the aortic arch: in 50% of the casts only the brachiocephalic trunk (BCT) and the left subclavian artery (LSA) originated from the aortic arch; in one geometry the left common carotid artery (LCCA) and the left vertebral artery (LVA) were also aortic arch branches; and the remaining casts had 3 aortic arch branches (LCCA or LVA in addition to the BCT and LSA). This is schematically shown in figure 3.6. Smaller arteries, which were sometimes be observed, were omitted here.

Anatomic variation is also apparent in the arrangement of the most proximal dorsal intercostal arteries, which did not always form the first intercostal branch pair on the descending aorta. This was the case for two animals (VPADP100324a and AAEH091110).

3.3.3 Geometric characterisation

Each aorta is characterised geometrically by its centreline, with varying curvature and torsion, the hydraulic diameter at its aortic root (D_0) and its taper.

Curvature of all aortas increased steadily from the aortic root into the aortic arch, reaching its maximum just after the branching point of the BCT, as is shown in figure 3.7A. The maximum curvature was $(0.946 \pm 0.062)/D_0$ (animal-specific values of D_0 are given in table 3.1) and there was no significant difference in maximum curvature between immature and mature rabbits ($P = 0.14$). At the distal end of the aortic arch, at a distance of $5D_0$ from the first aortic branch measured along the centreline, the aorta was almost straight in some cases, whereas in the descending thoracic aorta curvature was small but generally non-zero.

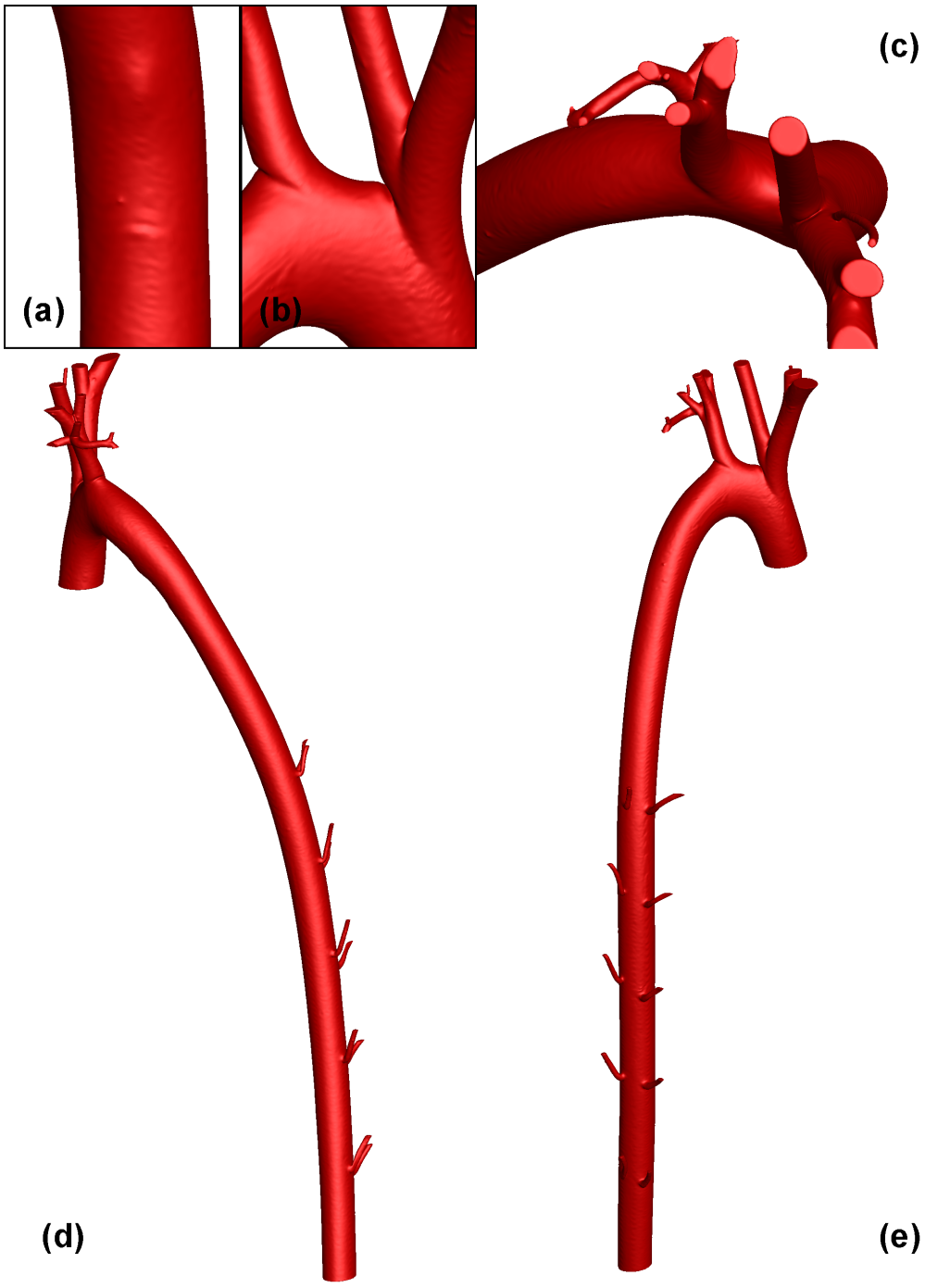

Figure 3.5: Reconstruction of the rabbit aorta denoted VPADP091210. (a) Close-up of the cusp near the attachment site of the ligamentum arteriosum; (b) Close-up of sharp-edged aortic arch branching sites; (c) Cranial view; (d) Left lateral view; (e) Dorsal view.

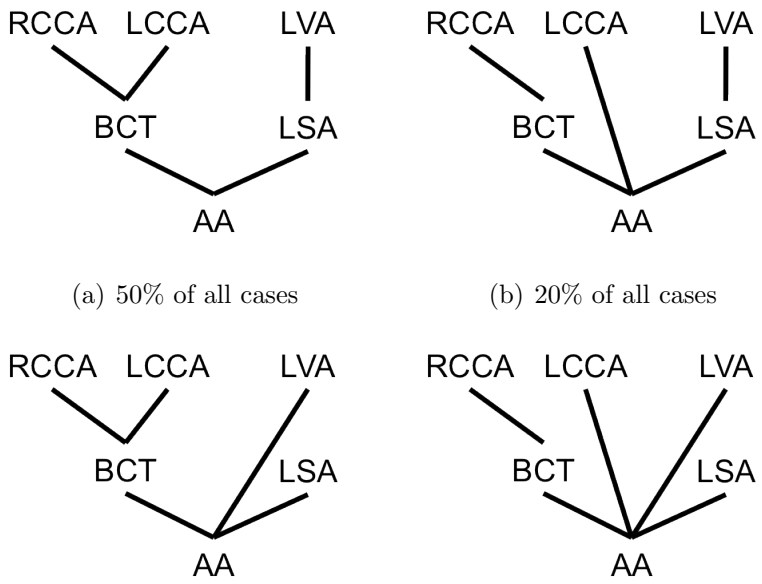

(a) 50% of all cases

(b) 20% of all cases

(c) 20% of all cases

(d) 10% of all cases

Figure 3.6: Aortic arch branching configurations and their relative occurrence in the dataset of rabbit aortas. RCCA: right common carotid artery; LCCA: left common carotid artery; LVA: left vertebral artery: BCT: brachiocephalic trunk; LSA: left subclavian artery; AA: aortic arch.

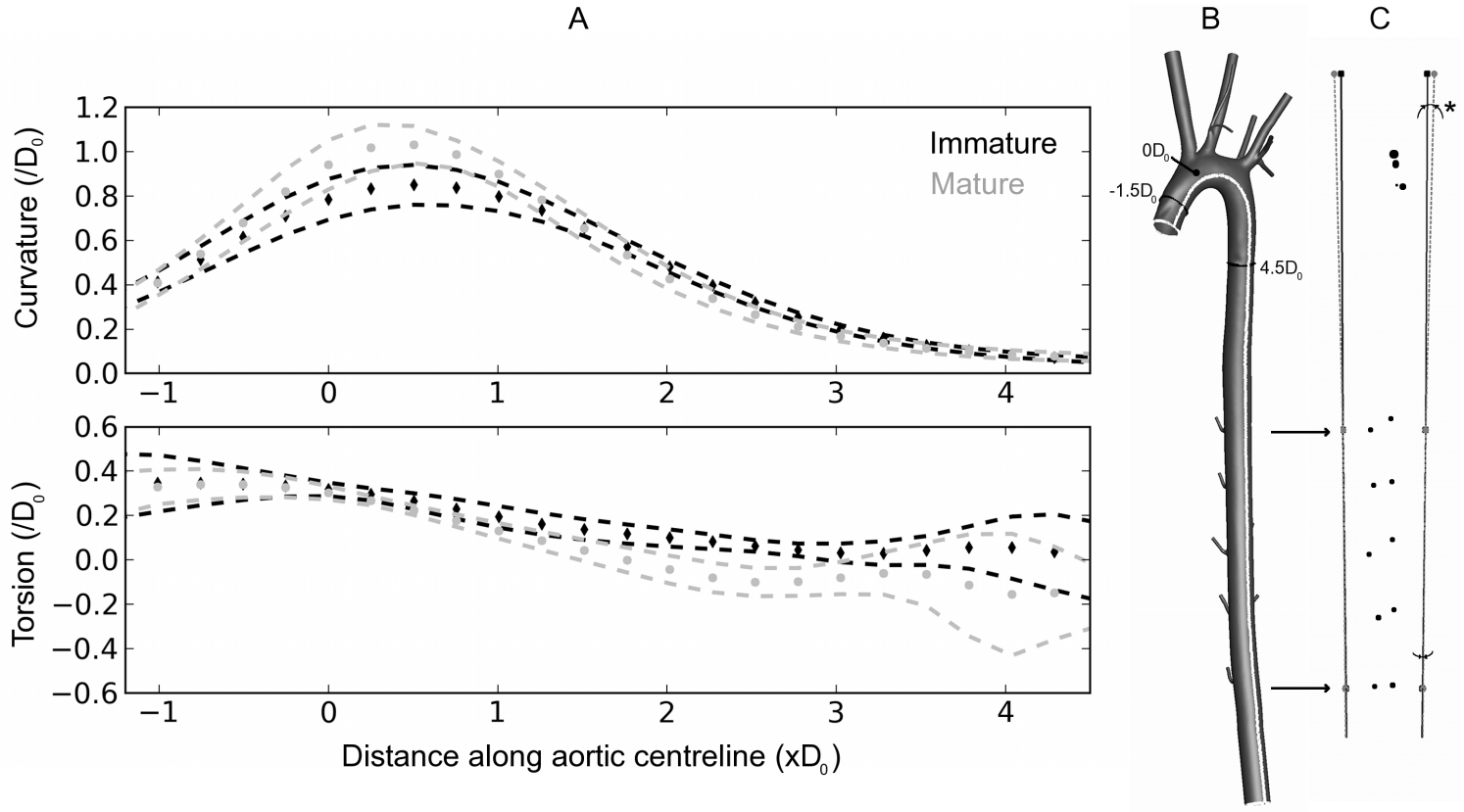

Figure 3.7: A: Curvature and torsion of the aortic arch of immature and mature rabbits (mean ± 1SEM). B: A thoracic aortic geometry showing the locations corresponding to the start, zero point and end of the horizontal axis of the plot in A. C: Diagram of opened immature and mature vessels (along the cutting line indicated in B), scaled longitudinally and circumferentially to match length and perimeter at the first intercostal branch pair, showing approximate branch locations and magnified (×4) taper angles (*significant without outlier in the immature group).

Figure 3.7A also shows the evolution of torsion along the centreline. A common feature was a peak in torsion proximal to or near the branching point of the BCT. For the descending aorta the concept of torsion is less meaningful because of the small curvature values. As can be appreciated from figure 3.7A, which concentrates on the aortic arch (the range is indicated in figure 3.7B), there were no clear age-related differences in the evolution of curvature and torsion.

The inlet hydraulic diameter (D_0), listed for each animal in table 3.1, was 3.96 ± 0.430 mm for immature rabbits and 5.23 ± 0.431 mm for mature rabbits ($P = 0.07$). However, the geometry of one immature aorta (figure 3.4E) was more similar to the geometries of the mature group. This geometry was identified as an outlier in the immature group using Chauvenet's criterion based on D_0. After excluding this outlier, the inlet diameter for the immature aortas was 3.55 ± 0.143 mm ($P = 0.01$ on comparison with the mature group).

Figure 3.7C illustrates the taper of the immature and mature vessels. On average, aortic arches of mature rabbits were more tapered than those of immature rabbits: taper from the aortic root to the first intercostal pair was $0.12 \pm 0.174°$ for immature but $0.57 \pm 0.104°$ for mature rabbits ($P = 0.058$ for all rabbits; $P = 0.003$ without the immature outlier). This difference remained when comparing the fifth intercostal pair with the aortic root ($P = 0.13$ for all rabbits; $P = 0.018$ without the immature outlier), although taper angles were similar for the descending aortic segment between the first and fifth intercostal pairs ($P \approx 0.5$ with and without the immature outlier).

3.4 Discussion

A dataset of rabbit aortic geometries was obtained by micro-CT of vascular corrosion casts. The dataset showed marked variations in the branching configuration of the aortic arch. While most aortic arches had only 2 branches (BCT and LSA), the LCCA and/or the LVA sometimes also branched off the aortic arch. This observation is in agreement with a report by Baldwin (1920), who found that about 20% of 106

rabbit aortic arches differed in branching configuration from what is considered normal.

In humans, the configuration with 3 branches, the BCT, LCCA and LSA, is more common; 30% of human aortic arches have a different configuration (Putz and Pabst, 2006).

Geometric analysis of the rabbit aortas showed inter-individual anatomical variation, but no significant age-related changes, in the curvature and torsion of the aortic arch. With the Dean number De defined by equation (1.15), the maximum non-dimensional curvature of approx. 1 (cfr. figure 3.7) results in a maximum De of approx. $\mathrm{Re}/\sqrt{2}$.

The hydraulic diameter at the aortic root D_0 increased significantly with age (after removal of the outlier in the immature group). Although this is an obvious fact, it is still important to point out from a fluid mechanical point of view. The aortas of mature animals tapered more than those of immature animals, particularly in the arch region. Note that there was one outlier in the immature group which was more similar to the mature animals, but this geometry was identified as an outlier based on its D_0.

The change in taper with age has, to our knowledge, not previously been observed in rabbits. Data on the evolution of diameter along the aortic centreline of younger and older men (Casteleyn et al., 2010) suggest that this age-related difference also holds for the aortic arch of humans: the mean aortic diameter of younger men (25-29 years old) decreased by 17.2% from the ascending aorta into the aortic arch, but by 25.0% in older men (84-85 years old).

As small changes in geometry can induce significant deviations in WSS (Cheer et al., 1998; Vincent et al., 2011), particular attention was paid to the reconstruction of anatomically realistic definitions of the luminal surface. In the study presented here, a *post mortem* approach combining vascular corrosion casting with micro-CT was used. This has advantages and disadvantages compared to imaging the lumen *in vivo*, as detailed in section 3.1. Given the high resolution of the micro-CT

scans (isometric voxel sizes of approx. 50 µm), inaccuracies introduced in this step are considered negligible for the investigation of blood flow inside the geometries at the macro-scale. Moreover, a higher resolution close-up scan (half the voxel size) of an intercostal branch region did not reveal any smaller geometric details. The question then remains how accurately the casting process represents the actual vascular geometry. Two issues require consideration.

Firstly, since casts are static objects they cannot capture geometric variations due to the heartbeat. Secondly, a number of research groups have reported on the shrinkage of resin during vascular casting. Kratky and Roach (1984) showed that a mixture of Batson's #17 and methylmethacrylate resulted in $20 \pm 0.7\%$ volume shrinkage in femoral arteries of sheep, compared to $15.8 \pm 0.4\%$ in rigid syringes. For different methylmethacrylate-based resins, Weiger et al. (1986) measured the combined shrinkage of all but the largest vessels of the rat ($8.0 \pm 0.8\%$ in volume). However, to the author's knowledge, non-linear shrinkage properties have not fully been investigated. Since this is key to the geometric accuracy of casts, a validation study was performed as part of the work presented here. This study is the subject of the following section.

3.5 Validation of the vascular casting technique

This section presents an investigation of the non-linear shrinkage behaviour of Batson's #17 resin. Such an investigation can provide a better insight into the accuracy of the dataset introduced in section 3.3, but the results can also be applied in a broader context. Indeed, the reconstruction of vascular geometry is an important step in many studies related to the cardiovascular system, from the complex microvasculature (Leiser et al., 1997) up to the largest arteries (Shahcheraghi et al., 2002), and vascular casting is the preferred method amongst *post mortem* techniques. Casting materials can be based on silicone rubbers, such as Microfil (Flow Tech Inc., Carver, MA, USA; Hoi et al. (2011)), epoxies, such as araldite (Hanstede and Gerrits, 1982), or methacrylate, such as the Batson's #17 resin which was used for this thesis.

A method was developed to monitor shrinkage of Batson's #17 resin during setting. The method was applied *in vitro* in rigid syringes and flexible tubing and subsequently *in situ* in aortas of rats and rabbits. The majority of experiments were performed and processed by a UROP student, Miss K. C. J. Shih, under this author's supervision.

3.5.1 Methods

3.5.1.1 General experimental setup

Batson's #17 resin casts were prepared in rigid syringes and flexible tubing of various sizes and in arteries of rats and rabbits. The resin mixture was prepared using a 60:13:3 weight ratio for monomer base solution, catalyst and promoter respectively, and a minimum batch volume of 25 ml. Weight instead of volume ratios (as in section 3.2.2) were used to ensure greater consistency with each repetition of the experiment. A small amount of red or blue pigment was added until the mixture was uniformly blended. Red pigment was used in the majority of the syringe tests for optimal contrast against a white background. For experiments in arteries, blue pigment was preferred because of improved visibility through the vessel wall and contrast against the surrounded tissue. The mixture was left undisturbed for approximately one minute prior to injection, allowing air bubbles to surface.

Shrinkage characteristics were determined by high-resolution photography (Canon EOS 500D SLR or a Sony MVX35i, both with f:3.5-5.6 zoom lens). Images were taken immediately after the resin was injected into the recipient, and after the resin was completely solidified. For a number of samples, including all experiments in arteries, the complete shrinkage process was tracked by taking consecutive images every minute (for approximately one hour) while the camera remained stationary. Each image consisted of 3200×4700 pixels (file size of $\sim$ 6MB) or 4600×3000 pixels (file size of $\sim$ 3MB) for the Canon and Sony cameras respectively. Images were processed using ImageJ (Rasband, 1997-2011). The amount of shrinkage in diameter was calculated according to the following formula:

$$\frac{D_{\text{final}} - D_{\text{initial}}}{D_{\text{initial}}} \times 100 \tag{3.1}$$

Table 3.4: Materials and initial diameters of recipients used for casting, and the number of experiments in each type of recipient. For casts in flexible tubing and arteries the infusion pressure is also given.

Recipient	**Initial diameter (mm)**	**# experiments**
1 ml syringe	4.78	22
2 ml syringe	8.92	22
5 ml syringe	12.06	1
10 ml syringe	14.50	2
20 ml syringe	19.13	2
50 ml syringe	26.70	4
3 mm PVC tubing (50 mmHg)	3.01	1
3 mm PVC tubing (100 mmHg)	3.25-3.37	2
5 mm PVC tubing (50 mmHg)	6.16-6.23	2
1/4 inch RAUMEDIC tubing (50 mmHg)	7.71-7.74	2
1/4 inch RAUMEDIC tubing (100 mmHg)	8.92	1
Rat aorta (100 mmHg)	1.56-2.46	9
Rabbit aorta (100 mmHg)	2.52-3.63	3

where D_{initial} and D_{final} are the cast diameters before and after resin setting respectively. A similar formula was used for length-wise shrinkage. Measurements were verified using vernier calipers (resolution: 0.01 mm).

3.5.1.2 Casting in rigid syringes (*in vitro*)

Polypropylene syringes (Becton, Dickinson and Company) of 1 to 50 ml in volume were used in these experiments. The number of experiments for each syringe size is listed in table 3.4. Prior to the experiment a camera was secured onto a tripod and set on the same horizontal plane as a syringe stand. Once the resin had been prepared as described previously, the mixture was drawn into the syringe. The syringe tip was subsequently sealed using a cap or stopper; the plunger was removed. The syringe was placed in the syringe stand in a vertical position (tip facing downwards) and left there, allowing the resin to set. For image processing, the outer diameter of the syringe (see table 3.4, according to the manufacturer's product information)

was used as a length reference.

The setting of the resin is an exothermic process (Polysciences, Inc. Technical Data Sheet 105). For seven experiments with various syringe sizes, a thermocouple temperature probe (Lascar Electronics) was inserted in the resin mixture immediately after the resin was drawn into the syringe. Temperature was measured every 30 s for approximately 70 min. The ambient temperature was 21-22 °C. Time was recorded from the moment the resin components were combined, until the resin visibly shrunk in diameter. This duration is defined here as the setting time.

3.5.1.3 Casting in flexible tubing (*in vitro*)

Polyvinyl chloride (PVC) tubing (RAUMEDIC AG Tubing, ECC no-DOP) was used in these experiments, with internal diameters ranging from 3.00 to 6.35 mm. A total of 8 experiments were conducted; details are listed in table 3.4. A piece of tubing was placed horizontally on a flat surface. Resin was prepared and injected into the tube via a three-way tap, which was also connected to a manometer. Once a segment of approx. 20 cm was filled, the tubing was clamped and the pressure of the closed system was brought up to 50 or 100 mmHg, depending on the experiment. Pressure was maintained until the resin had set completely and shrinkage visibly occurred. Multiple photographs were taken after initial injection of the resin, and after complete setting of the resin. In most experiments, a ruler was placed next to and at the same level as the tubing, for use as a reference length in the image-processing step. Alternatively, the outer diameter of the tube was measured immediately after resin injection.

3.5.1.4 Casting in arteries *in situ*

All animal procedures complied with the Animals (Scientific Procedures) Act 1986 and were approved by the local ethical review panel of Imperial College London. A total of 11 rats and 3 rabbits were used in this study, but 2 rats were discarded due to leakage in the system or an unusual calcification of the arterial wall. Rats were euthanised by CO_2 inhalation following the 20% rising concentration principle.

The rabbits were euthanised with an overdose of sodium pentobarbitone (Euthatal, 0.8 ml/kg, IV) after receiving heparin (2000 USP units).

Prior to the experiment a camera was secured onto a clamp stand, facing downwards. The animal was placed in the supine position and its thorax and abdomen were opened along the midline. The descending aorta was exposed and manually cleared of adherent connective tissue to ensure a good delineation of the exterior of the vessel wall. A retrograde cannula was then inserted into the abdominal aorta. After flushing the vascular system with a 0.9% w/v saline solution for rabbits or a heparin (2000 USP units, IV) and saline solution for rats, resin was injected at a pressure of 100 mmHg. The infusion was continued, maintaining the pressure, until the resin started to solidify and no more resin could be added. A plastic reference piece, measured using vernier calipers (resolution: 0.01 mm) and placed next to and at the same level as the aorta, served as a length scale during the image-processing step. Since the vessel diameter varies along the aorta, shrinkage was computed for three points along the vessel (inter-point spacing of approx. 10 mm) in seven rats. Due to the abundance of fat tissue around one rat aorta and all rabbit aortas, only two points were taken for these animals.

3.5.1.5 Statistics

Data are presented as means with their standard deviations (SD). Differences between data sets were analysed by Student's unpaired t-test, using $P < 0.05$ as the criterion of significance. Coefficients of determination (r^2) were calculated where appropriate.

3.5.2 Results

3.5.2.1 Casting in rigid syringes

When Batson's #17 resin was left to set in a rigid syringe, it shrunk both in diameter and in length. The resulting resin casts were circular in cross-section. For 1 ml syringes, which are closest in size to the largest arteries of rats and rabbits, shrinkage was $3.38 \pm 1.48\%$ in diameter and $14.64 \pm 3.10\%$ in length. Figure 3.8(a) summarises

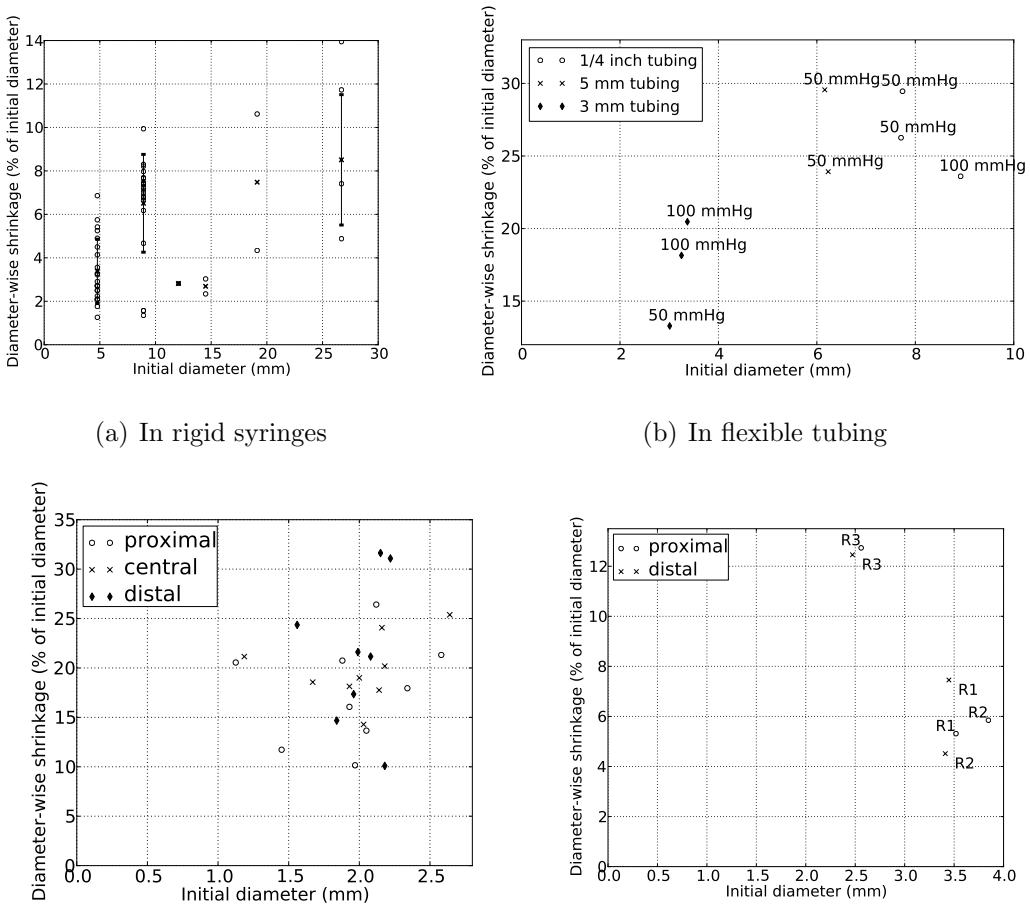

(a) In rigid syringes

(b) In flexible tubing

(c) In rat aortas

(d) In rabbit aortas

Figure 3.8: Percentage shrinkage in diameter measured during casting in four types of recipient.

the amount of diameter shrinkage in syringes of various sizes. Diameter shrinkage in 1 ml syringes was significantly different from the diameter shrinkage in 2 ml syringes ($6.51 \pm 2.25\%$, $P = 3 \times 10^{-6}$), indicating non-linear shrinkage behaviour. (Not enough experiments were conducted in larger syringes, which have diameters beyond the range of arterial diameters considered here, to justify a comparative analysis.)

The evolution of resin temperature and shrinkage with time is shown in figure 3.9 for an experiment in a 1 ml syringe. Temperature started to rise slowly once all resin components were combined. While the diameter remained constant at this stage, the resin height dropped drastically. After approx. 30 min the resin had shrunk in length by 12.16%. The temperature then started to increase rapidly, to peak around 55°C. After this peak, the temperature decreased as the resin solidified. The majority

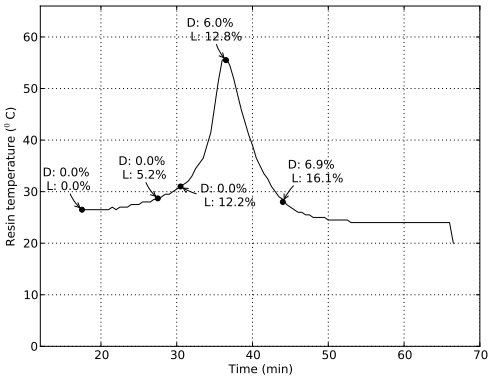

Figure 3.9: Evolution of resin temperature during casting in a 1 ml syringe as a function of time. Resin components were mixed at time $t = 0$ min. The amount of shrinkage in diameter (D) and length (L) are indicated for various points during the process.

of the shrinkage in diameter occurred around the peak in temperature. Once the temperature reached 30°C, the change in temperature slowed for the remaining period of the experiment.

The relation between the setting time and the maximum temperature reached during setting is shown in figure 3.10(a). Overall, the resin set faster when its temperature reached higher values. Figure 3.10(b) shows that the peak resin temperature depended linearly on the syringe diameter ($r^2 = 0.94$, P = 0.006).

3.5.2.2 Casting in flexible tubing

The resin casts made in flexible tubing were approximately oval rather than circular in cross-section. Hence, shrinkage was calculated based on caliper measurements in two directions perpendicular to each other. For example, in the tubing with inner diameter of 6.35 mm (which is beyond the range of arterial diameters of rats and rabbits), shrinkage was $23.80 \pm 0.97\%$ in the direction with minimal shrinkage but $30.76 \pm 5.57\%$ in the orthogonal direction. To enable comparison between tubing sizes, shrinkage values for the two directions were averaged. Figure 3.8(b) summarises the amount of shrinkage in diameter for experiments in tubing under pressure. Shrinkage was markedly higher than in syringes of similar diameter. Because of the flexibility of the walls, initial diameters were higher for higher infusion

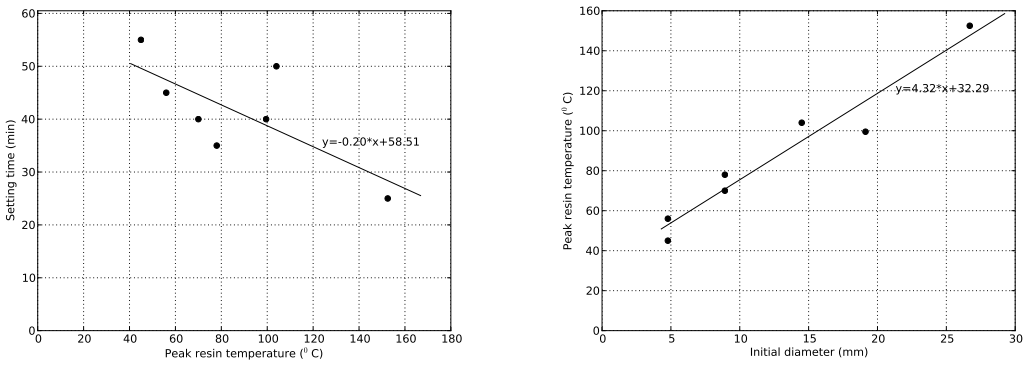

(a) (b)

Figure 3.10: (a) Setting time versus peak resin temperature during casting in syringes ($r^2 = 0.52$, P = 0.067); (b) Peak resin temperature during casting in syringes showed a strong linear correlation with syringe diameter ($r^2 = 0.94$, P = 0.006).

pressures, and this was also the case for the final cast dimensions. The results did not suggest any differences in shrinkage with infusion pressure.

3.5.2.3 Casting in arteries

The diameter of arteries varied along their length. Taken as an average of the diameter for three points along the vessel (measured from the photographs taken just after the start of the resin injection), the rat aortic diameters ranged between 1.56 and 2.46 mm. Casts of rat aortas shrunk by $20.58 \pm 3.33\%$ in diameter. There was no significant linear relationship between the artery diameter and percent diameter shrinkage (P = 0.12, figure 3.8(c)).

The stills in figure 3.11 illustrate how the aorta straightened during resin curing. The intercostal branching region shows that branching angles increased during the setting process.

Diameters of the rabbit aortas, taken as an average of 2 points along the vessel, ranged between 2.52 and 3.63 mm. Shrinkage for this species was $8.05 \pm 3.98\%$ in diameter, which is lower than the average shrinkage seen in rat aortas. The results are shown in figure 3.8(d).

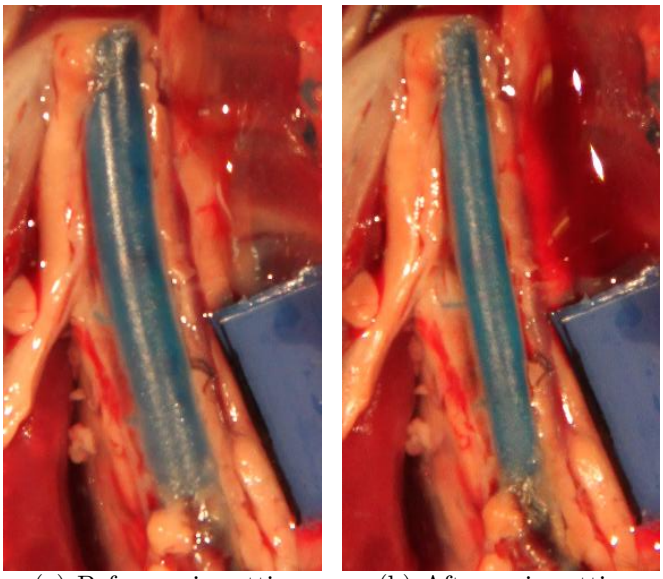

(a) Before resin setting (b) After resin setting

Figure 3.11: Stills before (a) and after (b) resin setting in a rat aorta, showing how the aorta straightened during the setting process. Branching angles of intercostal arteries increased over time.

3.5.3 Discussion

Geometric changes of Batson's #17 resin casts during setting were monitored over time. Based on the digital camera pixel resolution the smallest difference in diameter that could be resolved was 0.5% in 1 ml syringes and 1.1% in arteries. A comparison of the final cast dimensions measured using image processing and calipers showed differences of maximum 2% in diameter.

The results show that shrinkage does affect the geometry of vascular casts. Casts differed from their original counterparts not only in diameter, as reported previously (Kratky and Roach, 1984; Kratky et al., 1989), but also in cross-sectional shape, vascular curvature and branching angles.

Diameter Shrinkage measurements in 1 ml syringes ($3.38 \pm 1.48\%$ in diameter and $14.64 \pm 3.10\%$ in length) were within the range reported by Kratky and Roach (1984) for the same recipient but different compositions of Batson's #17-based resin. Additionally the results presented here indicate that shrinkage in syringes was non-linear, with significantly more shrinkage in 2 ml syringes (8.92 mm internal diameter)

compared to 1 ml syringes (4.78 mm internal diameter). An overall trend with size was not determined since diameters of larger syringes were far beyond the range of arterial diameters considered here.

Shrinkage values were also dependent on the recipient characteristics. (Interestingly, the Batson's #17 mixtures did not set in silicon-based recipients.) Diameter-wise shrinkage in flexible tubing was higher compared to shrinkage in similar-sized rigid syringes, and again different in arteries, leading to the hypothesis that the flexibility of the recipient wall plays a role in the shrinkage behaviour. In the rabbit aorta, shrinkage in diameter was $8.05 \pm 3.98\%$, compared to as much as $20.58 \pm 3.33\%$ in the rat aorta. This large difference could be explained by differences in arterial properties between species, with rat arteries being the more compliant (as is the case for carotid arteries; Cox (1978)). Additionally, differences between *in vitro* and *in situ* experiments could in part be due to a difference in set-up: *in vitro* syringe experiments used open systems, and *in vitro* experiments in tubing used closed systems; however, the *in situ* experiments in animals had leakage from the region of interest that were limited only by the high resistance of peripheral vessels.

As noted previously by Kratky et al. (1989), the infusion pressure is also a crucial determinant of the final cast dimensions.

Cross-sectional shape Caliper measurements on the casts made in flexible tubing revealed that their cross-sections were approximately oval rather than circular, implying directional variation in in-plane shrinkage characteristics. Since this was not the case for the syringe experiments, this phenomenon is likely to be a gravitational effect: while the tubing was placed horizontally, the syringes were clamped in a vertical position. Differences in in-plane shrinkage could not be measured in arteries, since the real cross-sectional shape of the arteries is unknown. Three-dimensional imaging of the setting process would be required to quantify this effect *in situ*.

Overall shape Length-wise shrinkage of the resin *in situ* caused distortion of the overall geometry: curved vessel segments tended to straighten and branching angles

changed over time during setting. This observation might also be responsible for the discrepancies in the iliac bifurcation angle measured from MR images and vascular casts of rabbits (Moore et al., 1999).

Temperature measurements during casting in syringes showed that the resin set faster if higher temperatures were reached. This is not surprising given the exothermic nature of the resin polymerisation reaction. The linear correlation between recipient diameter and temperature is likely to be a volume effect. Resin temperatures up to 152.5°C were measured during the casting in rigid syringes. This contrasts with observations by Levesque et al. (1979), who came to the conclusion that temperatures remained within the physiological range. However, their measurements were done in rabbit aortas; higher temperatures measured here in syringes may be explained by lower heat diffusion through the plastic syringe walls.

The results suggest that supra-physiological infusion pressures could be used to compensate for shrinkage-induced changes in diameters, curvature and branching angles. The pressure should ideally be determined based on a pilot experiment for the animal model and vascular section of interest, in which geometrical changes during resin injection and setting are monitored. However, it should be noted that the cross-sectional shapes might remain unphysiological.

The rabbit aortas from the dataset presented in section 3.3 were cast at mean physiological pressures. Nevertheless, translating the findings of the current section to this dataset, the reconstructed aortas are more representative of the geometries at lower pressures as in the diastolic phase.

3.6 Conclusion

In view of the simulation of blood flow in the rabbit aorta and recognising the importance of vascular geometry for flow dynamics, an anatomically realistic dataset of immature and mature rabbit aortas was developed. A literature study showed that none of the methods currently available for the acquisition of 3D vascular geometries is perfect. In this thesis, a combination of vascular corrosion casting and micro-CT

was used to obtain the rabbit aortic geometries. An investigation of the accuracy of the casting technique suggests that the reconstructed geometries best represent the aortas in the diastolic state. A geometric analysis showed marked inter-individual variation in the branching configuration of the aortic arch. Moreover, there was a notable increase in the degree of aortic taper with age, particularly in the aortic arch region.

Chapter 4

Blood flow in immature and mature rabbit aortas: steady-state and time-averaged pulsatile characteristics

The aim of this chapter is to investigate the characteristics of blood flow within the aorta of rabbits. This fits in with the central goal of the thesis presented here, which is to unravel the relation between atherogenesis and blood flow. Flow fields are predicted in the geometries of the dataset presented in section 3.3. This is done using numerical techniques (CFD), because *in vivo* measurements of blood velocity are not well resolved (Steinman, 2004). Since age-related differences have been observed in the atherosclerotic lesion distribution in the rabbit aortic model (Cremers et al., 2011), and it was shown in chapter 3 that the rabbit aortic geometry evolves with age, flow features in aortas of immature and mature animals are compared.

In line with the literature, the focus of this chapter is on steady-state and time-averaged effects. There is indeed no biological evidence (yet) that would suggest that features occurring during a particular part of the cardiac cycle are more important. Moreover, this chapter only discusses traditional metrics to capture potentially physiologically relevant flow features. A more in-depth analysis of pulsatile flow features

is covered in chapter 6.

Section 4.1 describes the pre- and post-processing techniques used for the CFD analysis. Pre-processing involves the generation of meshes based on the geometries from section 3.3, the choice of boundary conditions and a flow solver. Post-processing steps include the calculation of flow-related metrics and the mapping of flow results of different geometries onto a common grid.. The results of the analysis are shown in section 4.2. Age-related changes in the characteristics of the aortic blood flow are also identified in this section. In section 4.3 idealised models are developed to gain a better understanding of the governing flow dynamics. Flow is simulated and analysed in these models and the results are interpreted with reference to the results in the anatomically realistic geometries. Finally, section 4.4 discusses the validity and implications of the observations.

4.1 Methods

As mentioned in section 1.2.1, the motion of fluids is governed by the continuity equation and Navier-Stokes equations which, for blood flow in large arteries, can be reduced to equations (1.3)-(1.4). The problem is complemented by corresponding boundary conditions on $\partial\Omega$ and initial conditions at $t = 0$. Since in general no analytic solution is available, numerical techniques (CFD) are commonly used to approximate the solution ($\mathbf{u}$, p) in the computational domain. Input to the solver are a mesh of the computational domain and a set of boundary and initial conditions. This section therefore details not only the flow solver, but also mesh generation and the choice of boundary and initial conditions.

Simulations of flow enable the calculation of flow-related metrics, which are defined in this section. In addition, techniques for mapping the flow results of different geometries onto a common two-dimensional grid are described.

4.1.1 The spectral/*hp* element method

4.1.1.1 General concept

Equations (1.3)-(1.4) are a set of non-linear partial differential equations. Four traditional numerical methods exist to approximate their solution: finite difference, finite volume, finite element and spectral methods (Ferziger and Peric, 2002). The spectral/*hp* element method, which was employed for the thesis presented here, can be thought of as a high-order finite element method or a multi-domain spectral method (Karniadakis and Sherwin, 2005).

The finite element method subdivides the computational domain into subdomains or elements. This is called spatial or h-type discretisation, where h represents the characteristic size of the elements. The solution within each element is approximated using a low-order, often linear polynomial expansion. By reducing the size of the elements, or h-type refinement, algebraic convergence can be achieved.

For a spectral method, the solution is approximated by a global higher-order expansion within the entire computational domain. This is called spectral or p-type discretisation, where p refers to the order of the expansion. Increasing the number of modes in the expansion, or p-type refinement, results in exponential convergence.

While finite element methods exhibit greater geometric flexibility, as the size of the elements can vary within the computational domain, spectral methods exhibit superior convergence properties and higher accuracy. Spectral/*hp* element methods aim to combine these advantages by decomposing the computational domain into elements which broadly capture the geometry of the problem, while obtaining high spatial resolution by representing the solution within each element using a high-order polynomial expansion.

An in-house implementation of the spectral/*hp* element method, $N\epsilon\kappa\tau\alpha r$ (Karniadakis and Sherwin, 2005), was used to perform the flow simulations presented here.

4.1.1.2 *hp* discretisation

The set of equations (1.3)-(1.4) can be rewritten in the more general form of a differential problem, with equations of the form:

$$\mathbb{E}(u) = 0 \quad \text{in } \Omega \tag{4.1}$$

where u represents a component of $\mathbf{u}$ or p. The spectral/hp element method looks for a solution of the form:

$$u^{\delta}(\mathbf{x},t) = u^{0}(\mathbf{x},t) + \sum_{i=1}^{N_{\text{dof}}} \hat{u}_i(t)\Phi_i(\mathbf{x}) \tag{4.2}$$

where $\mathbf{x}$ denotes the spatial position, $\Phi_i(\mathbf{x})$ are analytic functions called trial or expansion functions, $\hat{u}_i(t)$ are the N_{dof} unknown coefficients, and $u^0(\mathbf{x},t)$ is selected to satisfy the initial and boundary conditions. Substitution of (4.2) into (4.1) produces a residual R:

$$\mathbb{E}(u^{\delta}) = R(u^{\delta}) \tag{4.3}$$

According to the method of weighted residuals, the following restriction is enforced on R in order to determine $\hat{u}_i(t)$:

$$\langle v_j(\mathbf{x}), R(\mathbf{x})\rangle = 0 \quad \text{for } j = 1,...,N_{\text{dof}} \tag{4.4}$$

where $v_j(\mathbf{x})$ are test or weight functions and the Legendre inner product $\langle .,. \rangle$ is defined as:

$$\langle f, g\rangle = \int_{\Omega} f(\mathbf{x})g(\mathbf{x})\mathrm{d}\mathbf{x} \tag{4.5}$$

In the Galerkin approximation, the test functions are chosen to satisfy: $v_j = \Phi_j$.

For h-type discretisation the computational domain is subdivided into N_{el} non-overlapping elements. (The mesh generation is detailed in section 4.1.2.) Within these elements the solution is approximated using a polynomial expansion. In other words, the global expansion basis $\Phi_i(\mathbf{x})$ is constructed from a combination of local expansion modes $\phi_p^e(\mathbf{x})$ defined within each element:

$$u^{\delta}(\mathbf{x},t) = u^{0}(\mathbf{x},t) + \sum_{i=1}^{N_{\text{dof}}} \hat{u}_i(t)\Phi_i(\mathbf{x}) = u^{0}(\mathbf{x},t) + \sum_{e=1}^{N_{\text{el}}} \sum_{p=0}^{P_o} \hat{u}_p^e(t)\phi_p^e(\xi) \tag{4.6}$$

where P_o represents the polynomial order of the expansion.

The choice of the local expansion basis strongly affects the numerical implementation and efficiency of the spectral/*hp* element method. In general, local expansions can be classified as nodal or modal expansions. Nodal expansions evaluate the approximate solution at a fixed set of points (nodes); the coefficients $\hat{u}_p^e$ then represent the value of the solution at a given node. Modal bases on the other hand are hierarchical in nature: a higher order modal basis can be constructed from lower order basis modes. The reader is referred to Karniadakis and Sherwin (2005) for a detailed discussion on the advantages and drawbacks of various options. In the $N\epsilon\kappa\tau\alpha r$ implementation a modal C^0 continuous expansion basis is used.

As there are more local expansion coefficients $\hat{u}_p^e$ than global expansion coefficients $\hat{u}_i$, further conditions are required to relate the local and global definitions of the solution u^δ. The continuous Galerkin method requires that the solution u^δ is C^0 continuous across elements. This condition is equivalent to imposing continuity at the boundaries of internal elements. The discontinuous Galerkin method takes a different approach; for advective terms coupling between elements is ensured by equating fluxes across elemental boundaries (Sherwin, 2003).

4.1.1.3 Temporal discretisation

The solution of the set of equations (1.3)-(1.4) can be obtained using a dual splitting scheme (Karniadakis and Sherwin, 2005):

$$\frac{\hat{\mathbf{u}} - \sum_{q=0}^{J_i-1} \alpha_q \mathbf{u}^{n-q}}{\Delta t} = -\sum_{q=0}^{J_e-1} \beta_q (\mathbf{u}^{n-q} \cdot \nabla \mathbf{u}^{n-q}) \quad \text{in } \Omega \tag{4.7}$$

$$\nabla^2 p^{n+1} = \nabla \cdot \left(\frac{\hat{\mathbf{u}}}{\Delta t} \right) \quad \text{in } \Omega \tag{4.8}$$

$$\left(\nabla^2 - \frac{\gamma_0}{\nu \Delta t}\right) \mathbf{u}^{n+1} = \nabla p^{n+1} - \frac{\hat{\mathbf{u}}}{\nu \Delta t} \quad \text{in } \Omega \tag{4.9}$$

with consistent boundary conditions for Eq. (4.8):

$$\frac{\partial p^{n+1}}{\partial n} = -\mathbf{n} \cdot \left[\frac{\partial \mathbf{u}^{n+1}}{\partial t} + \nu \sum_{q=0}^{J_p-1} \beta_q (\nabla \times \boldsymbol{\omega})^{n-q} + \sum_{q=0}^{J_e-1} \beta_q \mathbf{N}(\mathbf{u}^{n-q}) \right] \quad \text{on } \partial\Omega \tag{4.10}$$

where $\mathbf{u}^n$, p^n and $\boldsymbol{\omega}^n$ represent the velocity, pressure and vorticity fields at $t = t^n$ and $\Delta t = t^{n+1} - t^n$. The parameters α_q, β_q and γ_0 are the weights for mixed explicit-implicit integration of advection-diffusion equations using stiffly-stable integrators (table 5.2 of Karniadakis and Sherwin (2005)), and J_e, J_i and J_p are the orders of integration. Since the advection term is treated explicitly, Δt needs to satisfy a Courant-Friedrichs-Lewy (CFL) condition to guarantee the stability of the time scheme.

For a matrix formulation of the problem the reader is referred to Karniadakis and Sherwin (2005) and Grinberg et al. (2009).

4.1.1.4 Application in aortas of rabbits

The spectral/*hp* element method was applied to simulate blood flow in the geometries of the dataset presented in section 3.3, with the exception of geometry VPADP110713a since this geometry was identified as an outlier in the immature group (section 3.3.3). For the simulations of flow, solutions within each mesh element were approximated using 5^{th} order polynomials. Convergence of the solutions was verified for selected configurations using up to 7^{th} order polynomials. The difference in average aortic WSS when increasing the polynomial order from 3 to 5 was below 0.8% for all steady-state simulations with inflow Reynolds number $\text{Re}_{\text{in}} = 300$. Steady simulations were solved using a Galerkin projection with a discontinuous substepping method (Sherwin, 2003), while a continuous Galerkin method was chosen for pulsatile simulations. Time integration was of first order, with typical normalised time steps of 0.002 ($\times D_0/u_0$).

4.1.2 High-order mesh generation

As mentioned in section 4.1.1.2 the spectral/*hp* element method involves *h*-type discretisation. Consequently, the fluid volume needs to be subdivided into elements, a process called mesh generation. As part of the work presented here, meshes were generated for the set of geometries obtained by micro-CT of vascular corrosion casts (cfr. section 3.3.2). Mesh generation for each geometry was performed in a total

three steps. First, the surface of the volume was triangulated. Afterwards, the volume was filled with tetrahedral and prismatic elements. This two-step strategy - surface meshing followed by volume meshing - is commonly used to generate meshes for finite element applications. However, in contrast to finite element meshes, the meshes generated here were deliberately made relatively coarse since high-order polynomials can represent the solution more accurately inside the elements. On the downside, coarse straight-sided meshes generally do not conform well to the boundaries of complex geometries. A third step was therefore added to the procedure, in which the surface elements were curved to better represent the boundary geometry. Spectral/*hp* elements allow elements to be curvilinear.

The three steps of the high-order mesh generation process are now described in greater detail.

4.1.2.1 Surface meshing

In a first step, flow extensions terminating with a circular cross section were added to the intercostal arteries, aortic arch branches and descending aorta of the geometries using VMTK. These extensions facilitate the application of boundary conditions away from the region of interest, as explained in section 4.1.3.

The surface of each geometry was re-triangulated using curvature size functions (Gambit 2.4.6, ANSYS, Inc.). Curvature size functions enforce a limit on the angle between the outward-facing normals of any two adjacent mesh elements. Consequently, the size of the triangles of the resulting mesh is curvature-dependent, with small triangles in regions where the surface is highly curved. The newly obtained mesh was subsequently smoothed using the VMTK-implementation of the Taubin algorithm, a volume-preserving variant on Laplacian smoothing (see footnote in section 3.2.5). Smoothing essentially moves each vertex to a new position, defined by a weighted sum of the locations of its neighbouring vertices (Bray, 2004), and therefore predominantly acts upon larger elements. Since the size of the elements in the base mesh was curvature-dependent, small-scale geometric features in highly curved areas were retained in this smoothing step. The change in volume introduced in this step was 0.45% (for geometry VPADP100209), corresponding to a change in

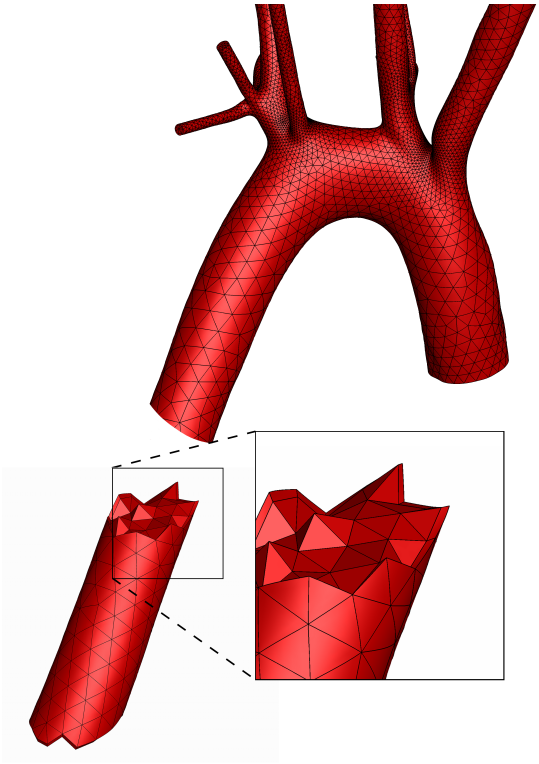

Figure 4.1: High-order volume mesh of the aortic geometry of rabbit VPADP100209.

diameter of 0.23% (assuming a cylindrical geometry with constant diameter). The resulting mesh will be referred to as the *high-definition surface mesh*.

As spectral/*hp* element methods can deal with coarse meshes, the number of surface elements was reduced in a last surface meshing step. Once more, curvature size functions were used, but this time the lower and upper limits on the size of the triangles were increased. The surface mesh of an aortic arch is shown in figure 4.1 (top).

4.1.2.2 Volume meshing

The volume meshes were generated in two steps: a prismatic layer, containing elements with an aspect ratio of 5, was first extruded from the surface mesh, and the remaining inner volume was then filled with tetrahedral elements. Both steps were performed using TGrid 4.0.24 (Ansys, Inc.). The cut-away of a mesh section in figure 4.1 shows the triangular faces of the internal tetrahedral elements and quadrangular faces of the prismatic elements adjacent to the arterial wall. The

Table 4.1: Total number of volume elements in the meshed geometries (N_{el}) and inflow Reynolds number ($\mathrm{Re}_{\mathrm{in}}$) for the simulations with $u_0 = 0.199\,\mathrm{m/s}$. Lettering corresponds to table 3.1. Note that geometry E was not included in the haemodynamic analysis. Simulations for geometry F are discussed in Vincent et al. (2011). In the geometries indicated with an asterik both steady-state and pulsatile dynamics were simulated.

Rabbit ID (short)	**Rabbit ID (long)**	$N_{\mathbf{el}}$	$\mathbf{Re}_{\mathrm{in}}$
A*	VPADP100209	81164	172
B	VPADP100324a	81504	204
C*	VPADP100426b	72685	176
D	VPADP110713a	65988	177
F	AAEH081013	79847	300
G*	VPADP091210	95337	222
H	AAEH091110	98376	230
I	VPADP091214	101356	254
J*	VPADP100713	91997	339

prismatic elements were used to accurately capture the boundary layer. Moreover, the curvature-dependent surface mesh ensured that the tetrahedral elements just below the prismatic layer fit inside the available space. Because of the geometric complexity of the aortic shapes, including sharp branching angles and subtle surface undulations, unstructured meshes were preferred, despite their weaker numerical performance compared to structured meshes (De Santis et al., 2010).

The total number of volume elements per mesh was approx. 10^5; details per mesh can be found in table 4.1. Combined with 5^{th} order polynomials this corresponds, in terms of degrees of freedom, to meshes of approx. 10^7 linear tetrahedral elements. For example, the volume mesh for geometry VPADP100209 consisted of a total of 102 786 elements, which is equivalent to a linear tetrahedral mesh with 19 727 166 elements.

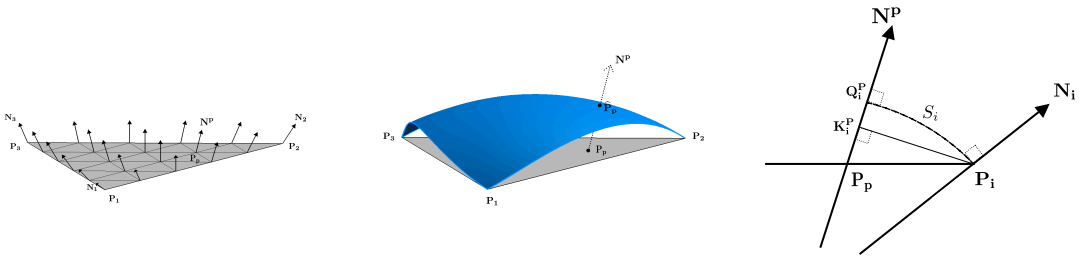

(a) (b) (c)

Figure 4.2: Construction of SPHERIGON patches: (a) Distribution of Phong normals in an element; (b) Phong projection; (c) Construction of a sphere S_i orthogonal to $\mathbf{N}_i$ at $\mathbf{P}_i$ and orthogonal to the line defined by $\mathbf{P_p}$ and $\mathbf{N^p}$. With permission reproduced from Plata (2010).

4.1.2.3 Curving the surface

The third step in the generation of a high-order volume mesh consists of curving the surface elements. This was done here following a method developed by Plata et al. (submitted to J. Numeric. Methods Fluids, Plata (2010)). The method employs so-called SPHERIGON patches to define the curvature of the triangular surface elements. In general, the SPHERIGON patch can provide a curvilinear approximation of a polygonal element given its vertices and vertex normals by blending spherical surfaces orthogonal to the vertex normals of the element (Volino and Magnenat Thalmann, 1998).

Consider a triangular surface element with vertices $\mathbf{P}_1$, $\mathbf{P}_2$ and $\mathbf{P}_3$ and vertex normals $\mathbf{N}_1$, $\mathbf{N}_2$ and $\mathbf{N}_3$, as illustrated in figure 4.2(a). Let $\mathbf{P_p}$ be an arbitrary point inside this triangle. In the application presented here, the points $\mathbf{P_p}$ are the nodes of the polynomial expansion. The Phong normal $\mathbf{N^p}$ at point $\mathbf{P_p}$ is defined as:

$$\mathbf{N^p} = \frac{\sum_{i=1}^{3} r_i^{\text{bar}} \mathbf{N}_i}{||\sum_{i=1}^{3} r_i^{\text{bar}} \mathbf{N}_i||} \tag{4.11}$$

where r_i^{bar} are the barycentric coordinates of point $\mathbf{P_p}$ (i.e. $\mathbf{P_p} = \sum_{i=1}^{3} r_i^{\text{bar}} \mathbf{P}_i$). The goal is now to find the location of point $\hat{\mathbf{P}}_\mathbf{p}$, which is the Phong projection of point

$\mathbf{P_p}$ onto the SPHERIGON patch. This is illustrated in figure 4.2(b). Let S_i be the sphere through $\mathbf{P}_i$, orthogonal to $\mathbf{N}_i$ in $\mathbf{P}_i$ and orthogonal to the line defined by $\mathbf{P_p}$ and $\mathbf{N^p}$. Let point $\mathbf{Q}_i^{\mathbf{p}}$ be the point of intersection of sphere S_i and the line defined by $\mathbf{P_p}$ and $\mathbf{N^p}$, as is illustrated in figure 4.2(c). It can then be shown that (Volino and Magnenat Thalmann, 1998):

$$\mathbf{Q}_i^{\mathbf{p}} = \mathbf{K}_i^{\mathbf{p}} + \frac{(\mathbf{P}_i - \mathbf{K}_i^{\mathbf{p}})\mathbf{N}_i}{1 + \mathbf{N^p}\mathbf{N}_i} \tag{4.12}$$

where $\mathbf{K}_i^{\mathbf{p}}$ is the orthogonal projection of $\mathbf{P}_i$ onto the line defined by $\mathbf{P_p}$ and $\mathbf{N^p}$.

The SPHERIGON patch at point $\mathbf{P_p}$ is determined by blending the points $\mathbf{Q}_i^{\mathbf{p}}$:

$$\hat{\mathbf{P}}_{\mathbf{p}} = \sum_{i=1}^{3} f_i^p \mathbf{Q}_i^{\mathbf{p}} \tag{4.13}$$

where the blending functions f_i^p can be chosen to guarantee C^0 and C^1 continuity across patches (Volino and Magnenat Thalmann, 1998) of the SPHERIGON approximation which is not a polynomial space (Plata et al., submitted to J. Numeric. Methods Fluids).

The construction of SPHERIGON patches requires an accurate estimate of the vertex normals $\mathbf{N}_i$ of the (coarse) surface mesh. These were calculated here according to the algorithm developed by Plata (2010). Consider a straight-sided coarse mesh $\mathcal{M}$ and a corresponding straight-sided high-definition surface mesh $\bar{\mathcal{M}}$. Let $\mathbf{P}_i$ be an arbitrary vertex in $\mathcal{M}$ and $\bar{\mathbf{P}}_i^j$ $(j = 1...N_v)$ the N_v vertices in $\bar{\mathcal{M}}$ closest to $\mathbf{P}_i$. $\bar{\Omega}_j$ $(j = 1...N_v)$ are the N_v elements constructed from the vertices $\bar{\mathbf{P}}_i^j$ and $\mathbf{P}_i$.

The normal $\mathbf{N}_i$ at vertex $\mathbf{P}_i$ is then approximated by averaging the face normals $\bar{\mathbf{N}}_j$ of the elements $\bar{\Omega}_j$:

$$\mathbf{N}_i = \frac{1}{\sum_{j=1}^{N_v} \bar{A}_j} \sum_{j=1}^{n_v} \bar{\mathbf{N}}_j \bar{A}_j \tag{4.14}$$

where $\bar{A}_j$ is the face area of element $\bar{\Omega}_j$.

When curving one side of a volume element, it is possible that the element becomes invalid. An example is given in figure 4.4(a), in which the curved side $\mathbf{P}_1\mathbf{P}_2\mathbf{P}_3$ of the element protrudes into the opposite side $\mathbf{P}_4\mathbf{P}_5\mathbf{P}_6$. Although the

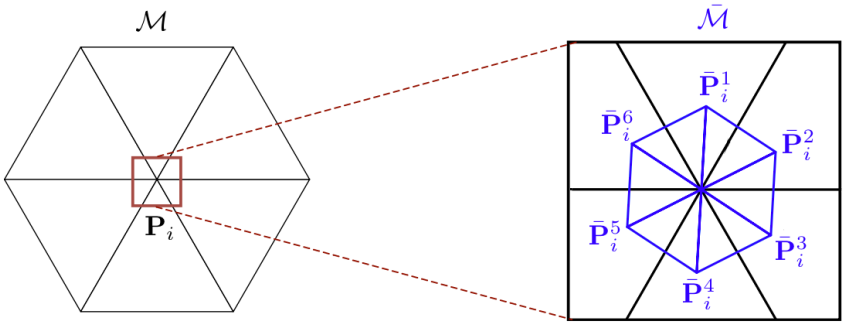

Figure 4.3: The normal $\mathbf{N}_i$ at vertex $\mathbf{P}_i$ can be computed by area-averaging the face normals of the elements $\bar{\Omega}_j$, which are shown as blue triangles. After Plata (2010).

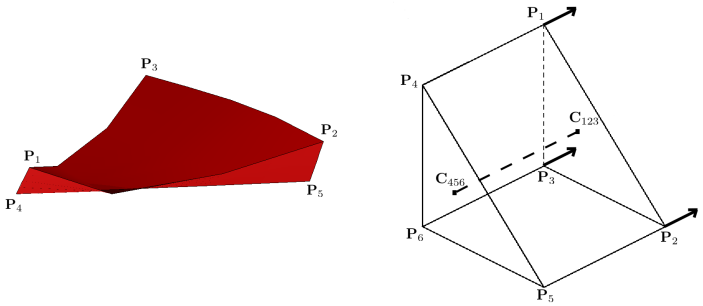

(a) (b)

Figure 4.4: (a) Example of an invalid prismatic element; (b) Illustration of a correction technique.

combination of a curvature-based surface mesh and a reasonable aspect ratio of the underlying prismatic elements ensured that most prismatic elements remained valid, there were a few exceptions in highly concave regions.

Here an algorithm to correct invalid prismatic boundary elements is proposed. The method is illustrated in figure 4.4(b). Let points $\mathbf{P}_i$ $(i = 1...6)$ be the vertices of a prismatic boundary element, and the side defined by the vertices $\mathbf{P}_i$ $(i = 1...3)$ be curved using the SPHERIGON patch technique. First the centroids $\mathbf{C}_{123}$ and $\mathbf{C}_{456}$ of the (planar) triangles $\mathbf{P}_1\mathbf{P}_2\mathbf{P}_3$ and $\mathbf{P}_4\mathbf{P}_5\mathbf{P}_6$ are determined. The vertices $\mathbf{P}_1$, $\mathbf{P}_2$ and $\mathbf{P}_3$ are then shifted away from $\mathbf{P}_4$, $\mathbf{P}_5$ and $\mathbf{P}_6$ respectively in the direction defined by $\mathbf{C}_{456}$ and $\mathbf{C}_{123}$ and over a distance equal to 0.5% of the distance between $\mathbf{C}_{456}$ and $\mathbf{C}_{123}$. The procedure is repeated until the element is no longer invalid. An alternative approach could be to curve both triangular elements of the problematic

prismatic elements.

4.1.3 Boundary conditions and model parameters

4.1.3.1 General modelling assumptions

Assumptions were made to limit the number of model parameters for the simulation of blood flow. In particular:

- The governing equations were reduced to the set of equations (1.3)-(1.4) under the assumption of a homogeneous, incompressible, Newtonian blood model. The blood density was taken to be $1044\,\mathrm{kg/m^3}$ (Kenner et al., 1977) and the blood dynamic viscosity $4.043\,\mathrm{g/ms}$ (Windberger et al., 2003);

- Arterial wall compliance and motion were neglected. The validity of these assumptions is addressed in section 4.4;

- At the aortic root the axial inflow velocity profile was assumed to be plug-like, and no in-plane flow component was applied. This is an approximation, since flow from the left ventricle is likely to be skewed and possess an in-plane component. To assess the effect of the axial velocity profile, parabolic and skewed profiles were also considered for one of the geometries (VPADP100209). In addition, a simulation with an in-plane inflow velocity component was performed to assess the influence of secondary flow at the aortic root;

- Flow splits to the various branches emanating from the aorta were based on experimental measurements where available in the literature, and estimated elsewhere. The flow splits are detailed in section 4.1.3.2. Further flow divisions to the individual branches were calculated using Murray's law (Murray, 1926), which states that the cube of the mother vessel's radius equals the sum of cubes of the daughter vessels' radii (r_i). When translating this law to flow rates using the continuity equation (equation (1.3)), the following expression is found for

the average speed u_1 in a branch with radius r_1 and outlet area A_1:

$$u_1 = f_{\mathrm{br}} \frac{Q}{A_1} \frac{r_1^3}{\sum_{i=1}^{N_{\mathrm{br}}} r_i^3} \tag{4.15}$$

where f_{br} is the percentage of the total flow (Q) going to all branches and N_{br} is the number of branches. The use of Murray's law is an approximation; the law has been debated by a number of research groups (Reneman and Hoeks, 2008; Trachet et al., 2011).

4.1.3.2 Simulations of steady flow

Steady flow was simulated in all geometries shown in figure 3.4, except for the outlier in the immature group (geometry E). Two simulations, with different boundary conditions at the aortic root, were performed in each geometry.

Aortic root In both sets of simulations, the axial inflow velocity profile was assumed to be plug-like, and no secondary inflow was applied.

- For the first set of simulations, an average velocity of $u_0 = 0.199\,\mathrm{m/s}$ was assumed at the aortic root on the basis of experimental mean flow rate measurements (Avolio et al., 1976) and the observation that mean aortic blood velocity is independent of body mass (Weinberg and Ethier, 2007). $\mathrm{Re_{in}}$ for each of those simulations is listed in table 4.1.

- To study the influence of geometry on the flow, a second simulation was run using $\mathrm{Re_{in}} = 300$, which corresponds to an average inflow velocity of $0.199\,\mathrm{m/s}$ for rabbit AAEH081013.

Aortic arch branches Flow splits to the aortic arch branches were based on experimental measurements, with 14.7% (Barakat et al., 1997b) of the flow in the ascending aorta going to the first branches of the aortic arch (the BCT, LCCA and their branches) and 7.1% (Barakat et al., 1997b) to the LSA and its branches. Further flow divisions to the individual branches were calculated using Murray's

law, as detailed above. Fully developed parabolic velocity profiles were assumed at the outlets of the branches. This is a reasonable assumption since flow extensions were added to the branches during mesh generation (section 4.1.2.1).

Intercostal arteries A total of 2% of the descending aortic flow was assumed to enter the 9 or 10 intercostal arteries, based on an estimate by Vincent et al. (2011). Further flow divisions to the individual branches were calculated using Murray's law, as detailed above. Note that flow splits to human intercostal branches, measured using US, have been reported by Koyanagi et al. (2009), but were considered physiologically unrealistic. Parabolic velocity profiles were assumed at the outlets of the branches. This is a reasonable assumption since flow extensions were added to the branches during mesh generation (section 4.1.2.1).

Distal descending aorta At the outlet of the descending aorta below the fifth pair of intercostal branches, a zero velocity gradient boundary condition was applied. This is a reasonable assumption since the outlet was extended during mesh generation (section 4.1.2.1). A zero pressure reference was placed at the outlet.

Aortic wall A no-slip condition was prescribed at the arterial wall.

4.1.3.3 Simulations of pulsatile flow

Time-dependent flow dynamics were simulated in two immature and two mature aortic geometries (figure 3.4, geometries A, C, G and J).

Steady-state boundary conditions at the aortic root ($\mathrm{Re_{in}} = 300$) and branches were modulated using a time-varying velocity waveform. This waveform, shown in figure 4.5, was computed by Dr. Jordi Alastruey using a pulse wave propagation model, which simulated pulse wave propagation in the largest arteries of the systemic circulation of a rabbit using the one-dimensional equations of blood flow in compliant vessels (Alastruey et al., 2009). The waveform for use in the simulations was selected at the proximal descending aorta, since the purpose was to accurately model flow in the descending aorta.

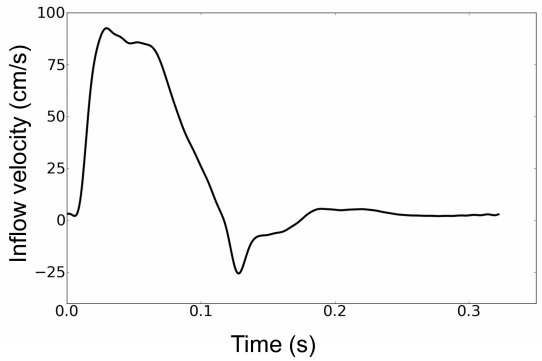

Figure 4.5: Velocity waveform at the aortic root for time-dependent simulations, here for $u_0 = 0.199\,\mathrm{m/s}$.

4.1.3.4 Initial conditions

A zero velocity field was chosen as the initial condition for simulations of steady as well as pulsatile flow. To damp transients related to this choice of initial condition in time-dependent simulations, two cardiac cycles were simulated and results were analysed for the second cycle.

4.1.3.5 Sensitivity analyses

For geometry VPADP100209 additional simulations were run to assess the influence of the choice of inlet conditions on the flow.

To analyse the effect of the inflow velocity profile, parabolic and skewed profiles were considered, as shown in figure 4.6. The parabolic profile is a fully developed profile for steady-state flow in straight pipes with circular cross-section and is not physiologically realistic at the inlet of the ascending aorta (Vincent et al., 2011). The skewed inflow profile was chosen to represent a more physiologically realistic condition, with skewing towards the inner curvature of the aortic arch based on unpublished MRI measurements in the porcine ascending aorta (A. De Luca, 2011).

To analyse the effect of secondary inflow, a 20% in-plane inflow component pointing away from the centre of curvature was included. Its direction and magnitude were based on extreme conditions in pigs (unpublished data, A. De Luca, 2011).

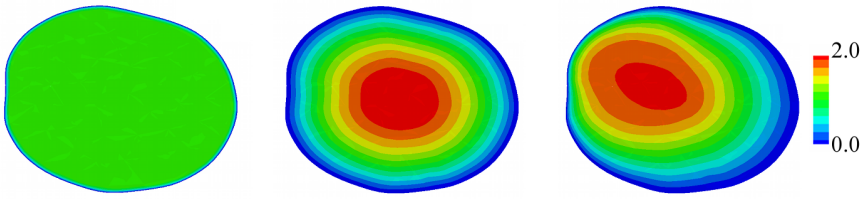

Figure 4.6: Axial inflow velocity profiles ($\times u_0$) applied to geometry VPADP100209: blunt (left), parabolic (middle) and skewed towards the inner curvature of the aortic arch (right).

4.1.4 Flow-related metrics

4.1.4.1 Coherent vortical structures

Coherent vortical structures were captured using the λ_2-criterion (Jeong and Hussain, 1995). This criterion defines a vortex in an incompressible flow in terms of the eigenvalues of the symmetric tensor $(\overset{\leftrightarrow}{S}_{\nabla\mathbf{u}})^2 + (\overset{\leftrightarrow}{\Omega}_{\nabla\mathbf{u}})^2$, where $\overset{\leftrightarrow}{S}_{\nabla\mathbf{u}}$ and $\overset{\leftrightarrow}{\Omega}_{\nabla\mathbf{u}}$ respectively represent the symmetric and antisymmetric parts of the velocity gradient tensor $\nabla\mathbf{u}$, so that:

$$\nabla\mathbf{u} = \overset{\leftrightarrow}{S}_{\nabla\mathbf{u}} + \overset{\leftrightarrow}{\Omega}_{\nabla\mathbf{u}} \, . \tag{4.16}$$

Concretely, the criterion defines a vortex core as a connected region with at least two negative eigenvalues of $\overset{\leftrightarrow}{S}^2_{\nabla\mathbf{u}} + \overset{\leftrightarrow}{\Omega}^2_{\nabla\mathbf{u}}$. In this way local pressure minima associated with the axis of a swirling motion are identified. However, since not all pressure minima correspond to vortex cores and vice versa, the criterion does not simply look for pressure minima, but:

- The pressure at a point that satisfies the λ_2-criterion does not have to be a minimum in all directions at that point, it only has to be a minimum in a plane perpendicular to the vortex axis;
- When looking for the minima, viscous effects are disregarded, as they could eliminate the pressure minimum in a flow with vortical motion;
- The effect of unsteady straining, which could create a pressure minimum without involving a vortical motion, is disregarded when looking for the minima.

For a mathematical derivation of the λ_2-criterion, the reader is referred to Jeong and Hussain (1995).

4.1.4.2 Shear-related metrics

For simulations of steady-state flow, the WSS magnitude was computed on the boundaries of the computational domain, according to equation (1.10).

For simulations of time-varying flow, the TAWSS and OSI were computed on the boundaries of the computational domain, according to equations (1.11) and (1.12) respectively.

4.1.5 Haemodynamic mapping

4.1.5.1 3D to 2D mapping

Mapping the 3D arterial surface onto a plane allows comparison between flow results and lesion distributions and facilitates statistical analysis of the flow results for the different age groups. The most straightforward parametrisation uses the curvilinear abscissa (along the centreline) and angular position of each point around the centreline. Antiga and Steinman (2004) presented a slightly modified method for mapping branches which are topologically equivalent to a cylinder. The approach allows point-by-point comparison between non-identical branching regions and is implemented in VMTK. As this mapping approach requires the geometry to be a topological cylinder, all rabbit aortas were pre-manipulated using VMTK and a purpose-written MATLAB R2009 (The MathWorks, Inc.) script. The manipulation steps are illustrated in figure 4.7 for an arterial segment containing one intercostal branch pair.

First, aortic branches were removed. This is illustrated in figure 4.7(a) and 4.7(b). The holes created during this procedure were closed and the correspondingly generated nodes tagged. After calculating the longitudinal and circumferential coordinates, the aortas were virtually opened up. The periodicity of the circumferential coordinate was interrupted by removing elements with nodes on either side of the cutting line, i.e. angular coordinates on either side of the spectrum. The cutting line

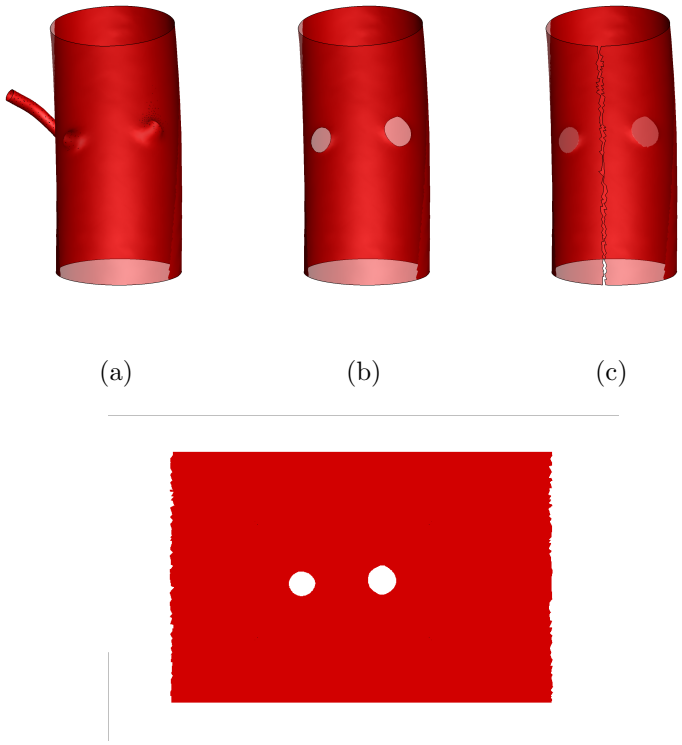

Figure 4.7: Procedure for mapping of the arterial lumen onto a 2D patch: (a) An arterial segment; (b) The branches are cut to create a topological cylinder; (c) The segment is cut open; (d) The segment is unfolded (*en face* view).

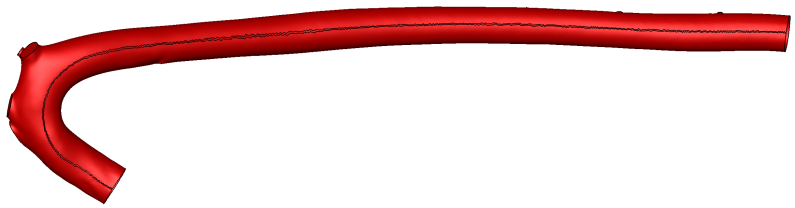

Figure 4.8: Location of the cutting line for 3D to 2D mapping, shown here for geometry VPADP100209 (ventral view).

naturally followed the curve of the vessel and is shown in figure 4.7(c) for the sample section and in figure 4.8 for an entire aorta. The cutting line was positioned on the ventral side and ensured that the locations of the intercostal ostia were similar to those in *en face* lesion maps of rabbit aortas (Cremers et al., 2011). Finally, the branch ostia were reopened by disregarding all tagged nodes. The 2D map of the sample section is illustrated in figure 4.7(d).

4.1.5.2 Maps around intercostal ostia

Around each intercostal branch opening a region of $2.4 \times 3.6\,\text{mm}$ was selected and WSS values in this region were mapped onto a 20×30 grid. To obtain the average distribution near the branches, maps were combined using the centre of the ostium as a datum. Squares close to the ostium were not calculated if they lacked data from more than 25 branches (as a consequence of the presence of the branch openings); these grid squares are coloured white.

4.1.5.3 Maps of thoracic aortas

For entire aortic segments, WSS, TAWSS and OSI values were mapped onto a coarser 20×140 grid. Values in corresponding grid squares were averaged for all animals within each age group to obtain the averaged maps. Averages were not calculated when data from more than two animals were lacking (as a consequence of the presence of branch ostia); these grid squares are coloured white.

4.1.6 Statistics

Data are presented as means with their standard errors (SEM) unless stated otherwise. Comparisons of aortic WSS between age groups were analysed by Student's unpaired t-test. One-way nested ANOVA was used to assess age-related differences in WSS around intercostal ostia. Nesting accounted for the fact that each animal contributed nine or ten intercostal ostia to the data. $P < 0.05$ was used as the criterion of significance.

4.2 Results

4.2.1 Changes in flow characteristics with age

In all aortas the plug-like axial velocity profile became crescent-shaped in the aortic arch, and was skewed to one side in the descending aorta. Two Dean-type vortices of unequal magnitude formed in the aortic arch. For mature animals these continued to propagate down the thoracic descending aorta, consistent with observations by Vincent et al. (2011) for a single mature rabbit aorta. However, in immature rabbits the aortic flow characteristics were different. In particular, although Dean-type vortical structures still formed in the aortic arch, they did not extend into the descending aorta. Representative cases from each age group are shown in figures 4.9A and 4.9D, using the λ_2-criterion to define the coherent vortical structures.

4.2.2 WSS around intercostal branch ostia

Figure 4.10A (top) shows the mean WSS distributions around intercostal ostia in immature and mature rabbits for the simulations with $u_0 = 0.199\,\mathrm{m/s}$. WSS was highest in a triangular region downstream of the ostium, and was also increased proximally. The evolution of WSS along the longitudinal centreline through the branch, corresponding to the average of the two central columns of squares in the maps, is shown in figure 4.11. The percentage difference between the peak WSS on the downstream side compared to the peak WSS on the upstream side along this line was not significantly greater for mature (51.5%, range: $11.5 - 99.9\%$) animals

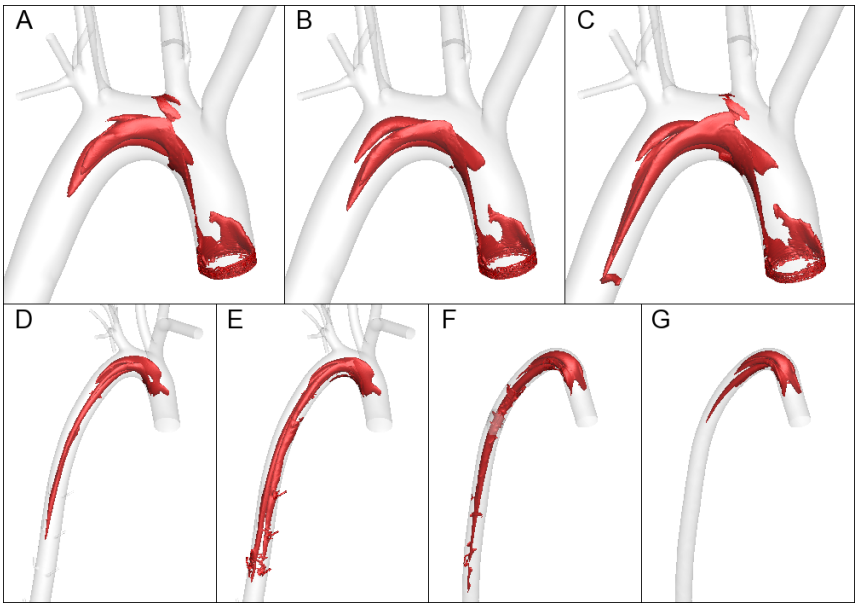

Figure 4.9: Coherent vortical structures for the following simulations: A: immature geometry with $u_0 = 0.199\,\mathrm{m/s}$; B: immature geometry with $\mathrm{Re_{in}} = 300$; C: immature geometry with $\mathrm{Re_{in}} = 300$ and zero net flow to the arch branches; D: mature geometry with $\mathrm{Re_{in}} = 300$; E: mature geometry with $\mathrm{Re_{in}} = 300$ and zero net flow to the arch branches; F: idealised mature geometry with taper ($\mathrm{Re_{in}} = 300$); G: idealised mature geometry without taper ($\mathrm{Re_{in}} = 300$). The immature and mature geometries are VPADP100209 and AAEH081013 respectively.

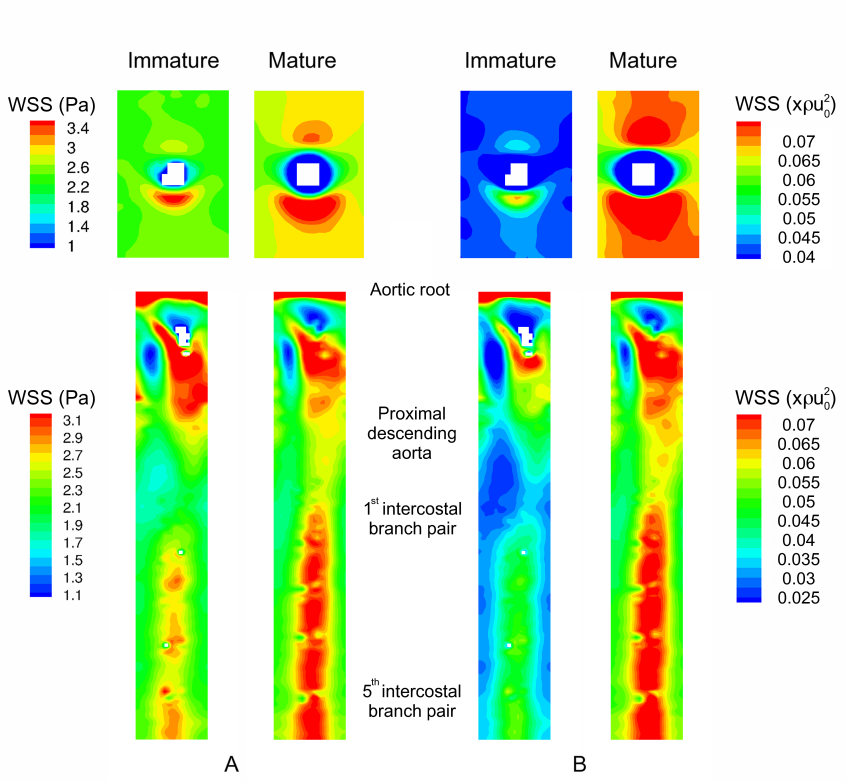

Figure 4.10: Averaged maps of WSS in immature and mature geometries around a branch ostium (top) and in the thoracic aorta (bottom), as computed from simulations with $u_0 = 0.199\,\mathrm{m/s}$ (A) or $\mathrm{Re_{in}} = 300$ (B). In B, the white spots correspond to locations where ostia were optimally aligned. The luminal surface of each segment, opened ventrally, is shown *en face*. Net aortic flow is from top to bottom.

than for immature (41.4%, range: 6.94-81.9%) animals (P = 0.10). WSS was lower in a ring around the ostium and to its sides. The average WSS in the $2.4 \times 3.6\,\mathrm{mm}$ region around immature ostia was 2.43 Pa (range: 1.38-3.30 Pa), compared to 2.71 Pa (range: 1.81-4.32 Pa) around mature ostia (P = 0.43).

The mean immature and mature WSS distributions around ostia based on the simulations with $\mathrm{Re_{in}} = 300$ are shown in figure 4.10B (top). Patterns were similar to those described above, but the difference in magnitude between immature and mature geometries was more pronounced. The average WSS, non-dimensionalised using ρu_0^2, was 0.0417 (range: 0.0229-0.0595) around immature ostia and 0.0637 (range: 0.0403-0.1194) around mature ostia (P = 0.055).

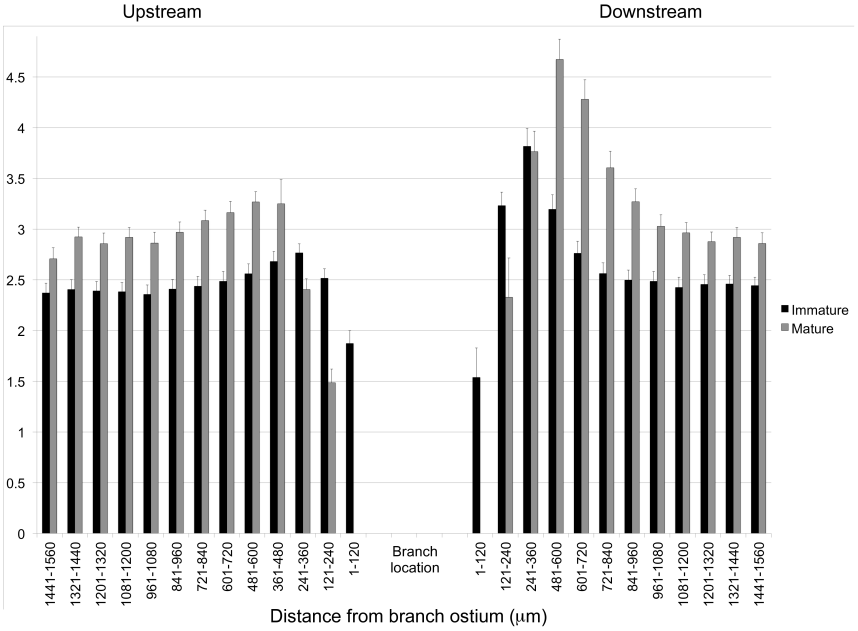

Figure 4.11: WSS (Pa, mean+1SEM) along the longitudinal line through the centre of the intercostal branch ostia.

4.2.3 WSS in the thoracic aorta

Figure 4.10A (bottom) shows the mean WSS distributions in thoracic aortas of immature and mature rabbits for the simulations with $u_0 = 0.199\,\mathrm{m/s}$. WSS was low along the greater curvature of the ascending aorta, on the distal inner wall of the aortic arch and, particularly for immature rabbits, proximal to the superior right intercostal artery. Zones of high WSS were found at the aortic root, where the originally plug-like velocity profile changed rapidly, and distal to the aortic arch branches. In mature animals the latter region extended further down into the descending aorta, resulting in a dorsal streak of high WSS. A similar streak formed more distally in the immature animals. The average WSS was $2.38 \pm 0.23\,\mathrm{Pa}$ in the immature thoracic aortas and $2.47 \pm 0.17\,\mathrm{Pa}$ in the mature aortas ($P > 0.5$).

The mean immature and mature WSS distributions in the thoracic aorta based on the simulations with $\mathrm{Re_{in}} = 300$ are shown in Figure 4.10B (bottom). Patterns were qualitatively similar to those for the simulations with constant inflow velocity. The average non-dimensional WSS was 0.0405 ± 0.0041 in the immature thoracic aortas, and 0.0576 ± 0.0061 in the mature aortas ($P = 0.06$).

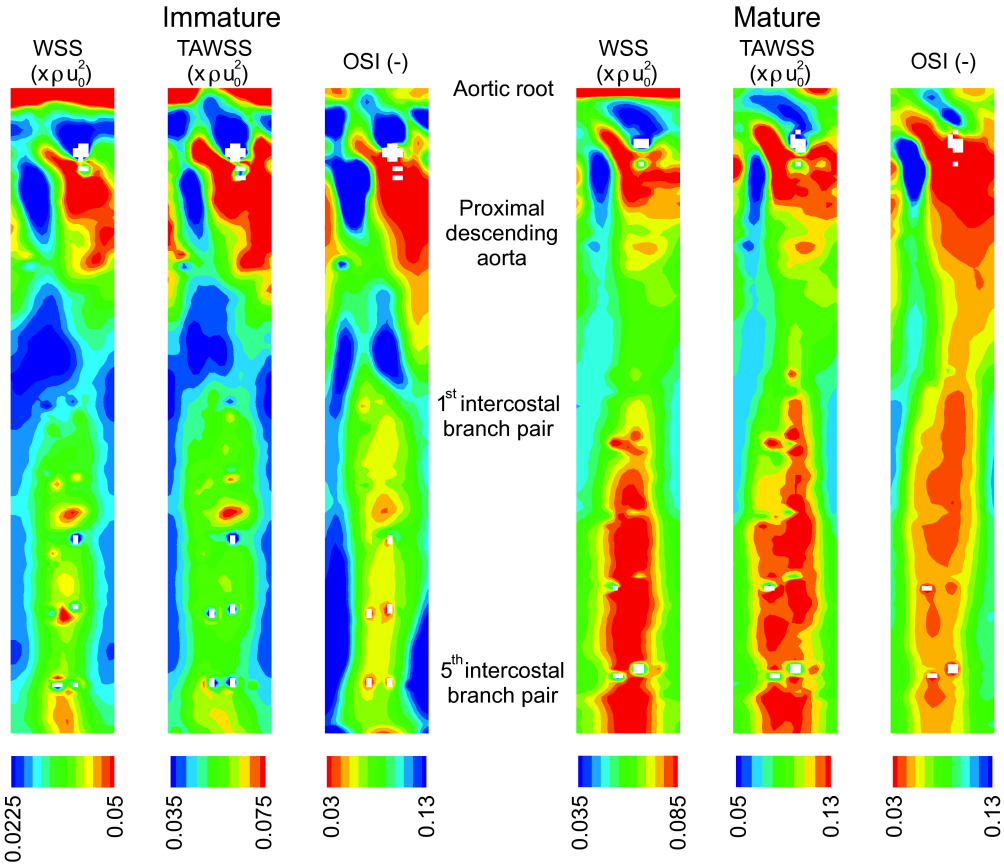

Figure 4.12: Averaged maps of TAWSS and OSI for time-dependent simulations in two immature and two mature aortas ($\mathrm{Re_{in}} = 300$). The corresponding averaged maps of steady WSS are also shown. The luminal surface of each segment, opened ventrally, is shown *en face*. Net aortic flow is from top to bottom.

4.2.4 Pulsatile flow characteristics

Unsteady blood flow was simulated in a subset of geometries, two from each age group, to study the effect of flow pulsatility. The resulting averaged maps of TAWSS and OSI are shown in figure 4.12. With adjusted scaling for each metric, time-averaged patterns were very similar to their steady equivalent. The most notable differences could be found in the proximal part of the descending aorta, where some unsteady (rather than quasi-steady) phenomena occurred: during early diastole there was more secondary flow than with steady-state dynamics in this region. In addition, the range of OSI (but not WSS or TAWSS) values in the descending aorta was substantially larger than corresponding values in the aortic arch.

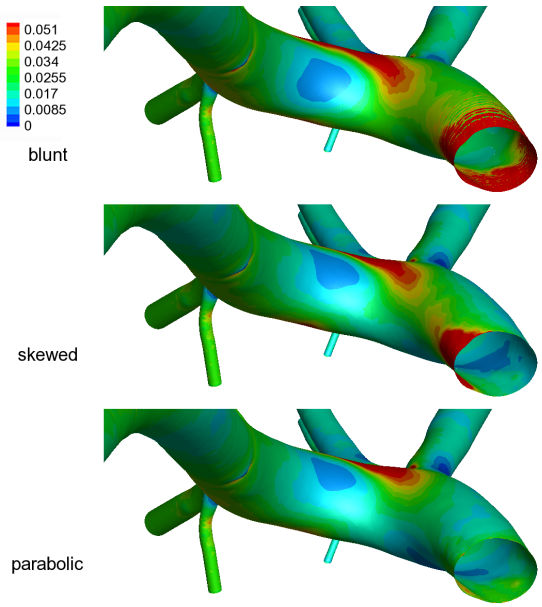

Figure 4.13: Influence of the velocity profile at the aortic root on WSS ($\times \rho u_0^2$) in the aortic arch of rabbit VPADP100209 (caudal view). The skewed inflow profile was skewed towards the inner curvature of the aortic arch.

4.2.5 Sensitivity of flow to assumptions and boundary conditions

A number of additional simulations were run in the aorta of rabbit VPADP100209 to evaluate the sensitivity of the results to modelling assumptions and boundary conditions. In all cases, $\mathrm{Re}_{\mathrm{in}}$ was kept at 300.

First, the effect of the inflow velocity profile was investigated. When a skewed parabolic profile (skewing towards the inner curvature of the aortic arch) was applied at the aortic root, the coherent vortical structure on the anatomical right-hand side developed earlier due to the higher velocity gradient. For this case, as well as with a parabolic inflow profile, the coherent vortical structures were slightly larger than for the original plug-like profile. However, the WSS distribution was hardly influenced by the changes in inflow profile: patterns were essentially unaltered throughout the aorta, although some minor quantitative changes could be seen in the ascending aorta and aortic arch. This is shown in figure 4.13.

Secondary inflow was generally disregarded. When this assumption was relaxed,

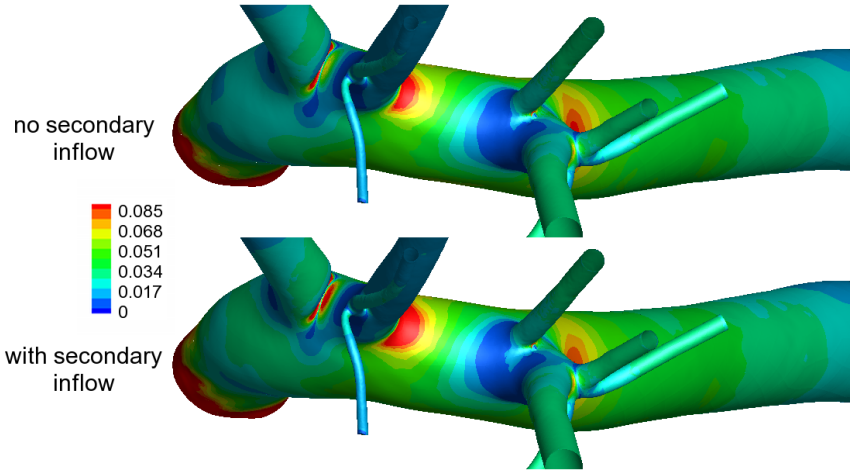

Figure 4.14: Influence of secondary inflow at the aortic root on WSS ($\times \rho u_0^2$) in the aortic arch of rabbit VPADP100209 (cranial view). For the case with secondary inflow an in-plane inflow component of 20%, pointing away from the centre of curvature, was applied.

WSS increased on the outer wall of the aortic arch, as is shown in figure 4.14, but once more WSS patterns and the extent of the coherent vortical structures remained largely unchanged.

To study the effect of flow into branches of the aortic arch, flow splits to these branches were set to zero. This resulted in an increase in the extent of the vortical structures, as the difference between figures 4.9B and 4.9C indicates. Moreover, the higher flow split towards the descending aorta caused an increase in the magnitude of the dorsal streak of high WSS. The location of the streak, however, was not affected.

4.3 Influence of centreline geometry and taper on flow in idealised geometries

Idealised models of the rabbit aorta were generated to gain insight in the governing flow dynamics. Concretely, tapered and non-tapered geometries were constructed based on the centreline of geometry AAEH081013.

This section starts with a description of the methods used to generate the idealised geometries, simulate blood flow inside them and analyse the flow dynamics

by transformation to a centreline-specific coordinate system. Subsequently, relevant flow features are discussed. Results in the geometry without taper are analysed first, focusing on the effects of curvature and torsion on the flow and resulting WSS. The influence of taper is discussed afterwards.

4.3.1 Methods

4.3.1.1 Idealised geometries

Idealised geometries were constructed based on the centreline of geometry AAEH081013. Two configurations were considered:

- Non-tapered geometry: A circular section with a radius equal to the maximum inscribed sphere radius at the aortic root of the original geometry, was swept along the centreline (Rhinoceros 4.0). The resulting geometry had the same centreline as the original aortic geometry, but constant cross-section and no side branches;

- Tapered geometry: A non-branching geometry with circular cross-sections was generated by sweeping a circular section through a series of circles along the centreline of the original geometry (Rhinoceros 4.0). The circles were derived from the original geometry, using corresponding maximum inscribed sphere radii at regular intervals ($D_0/4$ between adjacent circles).

4.3.1.2 Mesh generation and boundary conditions

Mesh generation was performed as detailed in section 4.1.2. The resulting volume mesh for the non-tapered geometry consisted of 1437 elements (562 prismatic and 875 tetrahedral elements), and the tapered geometry had a total of 1469 elements (594 prismatic and 875 tetrahedral elements). These numbers are significantly lower than those for the anatomically realistic geometries (table 4.1) because of the absence of sharp branching angles in the idealised models. A high number of degrees of freedom was achieved by using a higher order for the polynomial approximation (section 4.3.1.3).

Both cases were solved using a velocity inlet and zero velocity gradient boundary outlet. $\mathrm{Re_{in}}$ was set at 300, corresponding to the simulations in the anatomically realistic counterpart.

4.3.1.3 Numerical methods

Steady-state flow was calculated in the two idealised geometries using a spectral/*hp* element method, as detailed in section 4.1.1. Solutions within each element were approximated with 7^{th} order polynomials. Convergence was verified using up to 9^{th} order polynomials.

Techniques detailed in section 4.1.4 were used to locate vortical structures and calculate WSS distributions.

4.3.1.4 Decomposition of local momentum

To analyse the individual roles of inertial forces, viscous forces and pressure gradients, forces and accelerations were transformed from the Cartesian coordinate system (x, y, z) in which the flow-governing equations were solved, to an orthogonal Germano coordinate system (s, r, θ) (Germano, 1982). The orientation of the latter is indicated in figure 4.15 for a cross-section located at $\mathbf{R}(s)$, where:

$$\phi(s) = -\int_{s_0}^{s} \tau(s')ds' \tag{4.17}$$

with $\tau(s)$ the torsion, and s_0 an arbitrary value. The Germano coordinate system follows the centreline of the non-branching vessel, which can have varying curvature $\kappa(s) = |d^2\mathbf{R}/ds^2|$ and torsion $\tau(s)$. Each point P with Cartesian coordinates $\mathbf{x}$ is expressed using its local coordinates (s, r, θ). Conversion formulae for position, velocity, its first and second derivatives, and the pressure gradient are provided in appendix A.

The terms in the momentum balances of the Navier-Stokes equations (1.4) can be projected onto the tangential, normal and binormal axes, $\mathbf{T}$, $\mathbf{N}$ and $\mathbf{B}$ respectively (figure 4.15), to arrive at:

$$\mathrm{CA}_T = \mathrm{Co} + \mathrm{PG}_T + \mathrm{VF}_T, \tag{4.18}$$

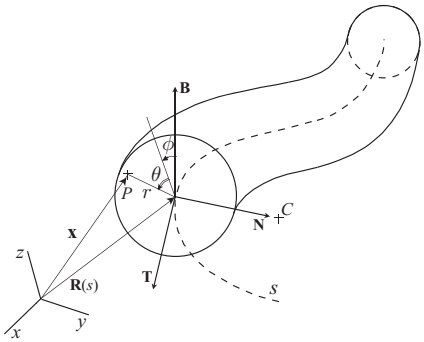

Figure 4.15: Germano coordinate system (s, r, θ) along the centreline of a vessel (Germano, 1982). With permission reproduced from Alastruey et al. (2012).

$$\mathrm{CA}'_N = \mathrm{CF}_N + \mathrm{TF}_N + \mathrm{PG}_N + \mathrm{VF}_N, \tag{4.19}$$

$$\mathrm{CA}'_B = \mathrm{TF}_B + \mathrm{PG}_B + \mathrm{VF}_B, \tag{4.20}$$

where the abbreviations CA, Co, CF, TF, PG and VF denote the convective acceleration and Coriolis, centrifugal, torsional, pressure gradient and viscous forces per unit of mass respectively. The subscripts indicate the direction of the force components, and primes indicate a modification compared to the equivalent force expressed in the Germano coordinates (s, r, θ). Concretely, torsion-dependent components were subtracted from CA_N and CA_B, giving rise to the terms $\mathrm{TF_N}$ and TF_B on the right-hand sides of equations (4.19)-(4.20). Consequently, TF is non-zero only in geometries with non-zero torsion, while CF and Co only exist in geometries with non-zero centreline curvature.

It can be shown that $\mathrm{Co}\mathbf{T} = -\boldsymbol{\Omega} \times \mathbf{V_N}$, where $\mathbf{V_N}$ represents the velocity component in the direction of $\mathbf{N}$ and $\boldsymbol{\Omega} = u\kappa h^{-1}\mathbf{B}$ about the local centre of curvature C ($h\kappa^{-1}$ is the distance from C of the vessel centreline to the projection of the point into the plane spanned by $\mathbf{T}$ and $\mathbf{N}$). Hence, Co is half of the usual Coriolis force per unit of mass.

The derivation of equations (4.18)-(4.20) starting from the Navier-Stokes equations in the Cartesian coordinate system can be found in appendix A and Alastruey et al. (2012).

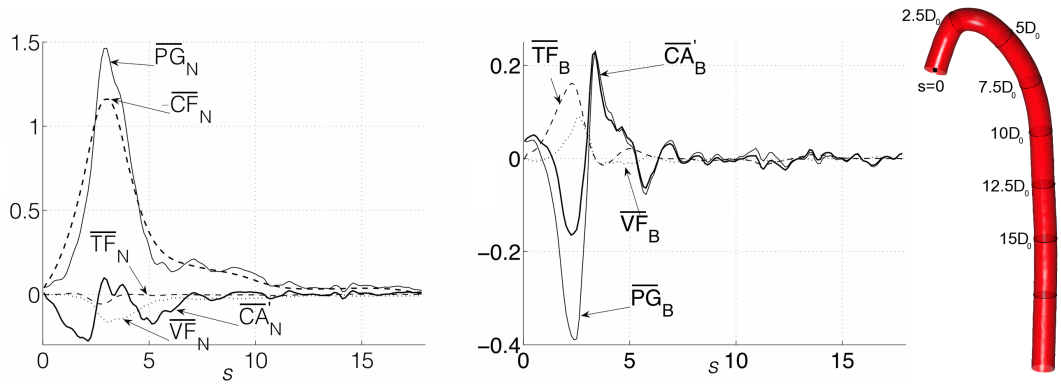

Figure 4.16: Cross-sectionally averaged normal (left) and binormal (middle) accelerations and forces along the centreline of the non-tapered idealised geometry. Overlines indicate cross-sectional averages of the corresponding quantities. The geometry is shown on the right. After Alastruey et al. (2012).

4.3.2 Findings

4.3.2.1 Effect of curvature and torsion

It was found in section 4.2.1 that Dean-type vortical structures developed in all rabbit aortic arches. This observation can be understood by analysing the effects of inertial, viscous and pressure gradient forces in the idealised geometry without taper. The most notable results of this decomposition are shown in figures 4.16 and 4.17.

As already indicated in section 1.2.3.4, the interaction between centrifugal forces and an in-plane pressure gradient gives rise to secondary motion. This interaction occurs in the ascending aorta of the idealised geometry without taper (figure 4.16, left). The counterplay between CF_N, which pulls the bulk flow away from the centre of curvature, and the opposing in-plane PG, which makes the flow return along the lateral sides, results in the formation of a pair of counter-rotating Dean-type vortices. The flow symmetry is broken by the torsional force TF, which expands the vortex of positive axial vorticity ω_s (figure 4.17, bottom left) and accelerates the core flow in the direction of $\mathbf{B}$ up to $s = 4D_0$ (as indicated by $\overline{\mathrm{TF}_B} > 0$ in figure 4.17, middle). TF rotates the positions of the two vortices in the clockwise sense and yields asymmetric pressure gradients that rotate the bulk of the axial flow

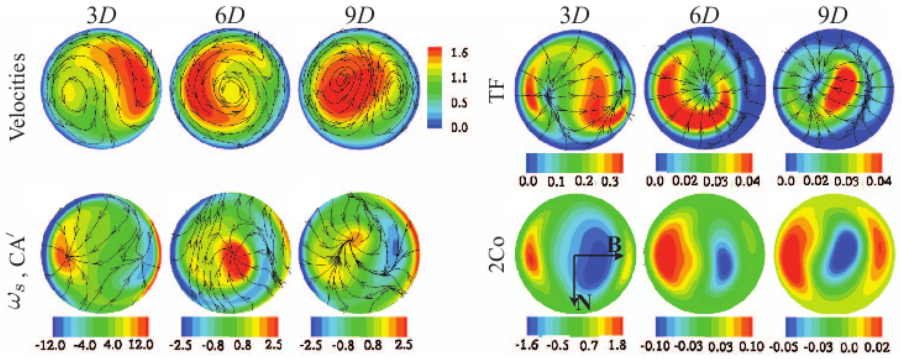

Figure 4.17: Magnitude contours of the following local quantities at 3 locations along the centreline of the non-tapered idealised geometry: (top left) axial velocity with secondary-flow streamlines; (top right) torsional force per unit of mass, TF, overlaid with its directions; (bottom left) axial vorticity ω_s, with overlaid directions of the in-plane convective acceleration CA′; (bottom right) full Coriolis force per unit of mass, 2Co. With permission reproduced from Alastruey et al. (2012).

clockwise.

In the second half of the aortic arch, the positions of the two vortices start to rotate anticlockwise. The vortex of positive ω_s moves toward the centre of the cross-section (figure 4.17, bottom left, $s = 6D_0$), generating a dominant anticlockwise swirling flow. From the end of the arch, TF helps to recover flow axisymmetry in the descending aorta by expanding the vortex of negative ω_s and contracting the vortex of positive ω_s.

Another notable observation in section 4.2 was the presence of a streak of high WSS on the dorsal side of the descending thoracic aorta. Figure 4.18 (left) shows that the maximum axial WSS ($\mathrm{WSS}_{s,\mathrm{peak}}$) in each cross-section correlates well with the local radial offset of the peak axial velocity (d_{peak}). In addition, the circumferential angles at which the axial velocity and WSS magnitudes reach their maximum are similar, as is shown in figure 4.18 (right). This is because a greater d_{peak} yields greater velocity gradients $\partial u/\partial r$ at the wall next to where the peak axial velocity is attained.

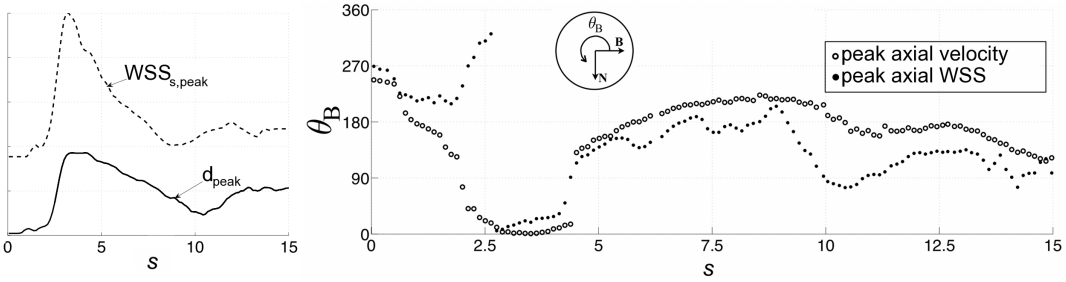

Figure 4.18: Left: The maximum axial WSS ($\mathrm{WSS}_{s,\mathrm{peak}}$, non-dimensionalised using its maximum value) and radial offset of the peak axial velocity (d_{peak}, non-dimensionalised using D_0) have a similar evolution along the centreline; Right: Circumferential angles of the locations of the peak axial velocity (open circles) and $\mathrm{WSS}_{s,\mathrm{peak}}$ (dots), measured as indicated on the diagram. After Alastruey et al. (2012).

4.3.2.2 Effect of taper

In the anatomically realistic geometries the extent of the vortical structures towards the descending aorta was found to be age-dependent. In a similar fashion, the vortical structures extended significantly further downstream in the tapered idealised geometry (figure 4.9F) than in the geometry without taper (figure 4.9G). This phenomenon can be interpreted using the ballerina effect: when a rotating body moves closer to the axis of rotation (as when a pirouetting ballerina draws in her arms), it will spin faster in order to conserve angular momentum. Since an age-related change in the degree of taper was observed in the dataset of rabbit aortic geometries (chapter 3) this exercise demonstrates that the age-related geometric change has an influence on the flow dynamics in the two age groups.

Corresponding changes in the strength of the high WSS streak on the dorsal side of the descending aorta are primarily a consequence of conservation of mass, which enforces an increase in velocity magnitudes along the centreline in the tapered geometry compared to the geometry without taper. Additionally, as was highlighted in section 1.2.3.2, velocity profiles in Jeffery-Hamel flow are intrinsically more blunted than those in Poiseuille flow.

4.4 Discussion

Simulations of blood flow were performed in aortas of immature and mature rabbits, in order to gain a better understanding of the haemodynamics in this animal model and to identify potential age-related differences. Two simulations of steady-state flow were run in each anatomically realistic rabbit aortic geometry:

- Simulation with $\mathrm{Re_{in}} = 300$: When matching the ratio of inertial to viscous forces, as indicated by Re, at the inlets of different arterial geometries, differences in flow characteristics further downstream can be exclusively attributed to differences in the vessel shape. Consequently, when analysing non-dimensional quantities, the simulations with constant $\mathrm{Re_{in}}$ provide an insight into the direct effects of geometry on blood flow;

- Simulation with $u_0 = 0.199\,\mathrm{m/s}$: This boundary condition is more physiologically realistic, since measurements and allometric arguments show that the mean aortic blood velocity is constant with animal size across at least three orders of magnitude of body weight (Weinberg and Ethier, 2007). The average aortic inflow velocity was based on experimental flow measurements in rabbits (Avolio et al., 1976).

Dean-type vortical structures developed in all aortic arches, and a streak of high WSS was found on the dorsal side of the descending thoracic aortas. These observations were explained through the analysis of the individual roles of inertial, viscous and pressure gradient forces in an idealised geometry without taper.

Differences in flow dynamics were observed between immature and mature animals: the coherent vortical structures and associated offset axial flow, generated by the curvature of the arch, extended further into the descending aorta in the latter. Differences between animals in cross-sectional shape, inlet conditions or nominal flow splits towards the arch branches could not explain these age-related changes. Only removing taper from a mature model drastically reduced the extent of the vortical structures, making it similar to the immature case. This result is consistent with the age-related change in the degree of taper, which was observed in the rabbit

aortic dataset (chapter 3). Geometric taper accelerates the axial flow and promotes a stretching of the vortical structures. Equivalently, this phenomenon can be interpreted using the ballerina effect: when a rotating body moves closer to the axis of rotation, it will spin faster in order to conserve angular momentum. In the same way, the greater geometric taper of the mature vessel causes the vortical structures to rotate faster and hence extend further into the descending aorta.

As mentioned in section 4.2.1, the simulation results for the mature aortas were in good agreement with Vincent et al. (2011). There are however discrepancies between the WSS results presented here and the results of Bond et al. (2011), who used endothelial nuclear elongation as a surrogate for WSS magnitude. Although both studies indicated elevated WSS downstream of immature branch ostia, only the CFD also indicated elevated WSS upstream, and only the nuclear morphology suggested a reversal in the pattern of WSS with age. The studies were in better agreement away from branches: both sets of data were consistent with counter-rotating helical flows and a dorsal streak of high shear in the descending thoracic segment. One possible explanation for the observed discrepancies is that nuclear morphology reflects factors other than WSS. For example, endothelial cells elongate in response to cyclic stretch as well as shear (Zhao et al., 1995), and the elongatory effect of shear can be amplified by flow pulsatility (Helmlinger et al., 1991). A second potential explanation for the discrepancy is that the assumptions underlying the CFD modelling are incorrect. A sensitivity analysis was therefore performed to consider whether relaxation of the assumptions could change the WSS patterns.

A first simplification was the assumption of Newtonian rheology. As quantitative changes introduced by this simplification are only modest (Johnston et al., 2006), relaxation of this assumption would not influence the conclusions of the work presented here.

Secondly, MRI flow measurements in mice and pigs have revealed that secondary flow is non-zero even at the aortic root and that the velocity profile at this location is skewed rather than plug-like (Van Doormaal (2010); unpublished data A. De Luca, 2011). The sensitivity analysis in the present study showed that more physiologically

realistic inflow conditions do not substantially alter the WSS patterns.

Aortic wall motion was not considered in the work presented here. Only a few studies have included this factor in their CFD models. They reported differences in WSS of less than 0.5 Pa (Suo et al., 2003), implying that the assumption of rigid walls is justifiable. Moreover, a study of the effects of flow pulsatility and wall compliance on haemodynamics in a mature rabbit aorta (unpublished data A.M. Plata, 2011) did not reveal any significant change in patterns of time-averaged flow-dependent metrics.

Finally, many recent experimental studies have highlighted the importance of flow reversal as an initiating factor for atherosclerosis (Cheng et al., 2006; Conway et al., 2010; Halliwill and Minson, 2010), suggesting that the pulsatility of the flow is decisive for the development of particular disease patterns. Also, an increasing number of computational studies compare lesion distributions against time-dependent flow metrics (Knight et al., 2010; Hoi et al., 2011). However, the patterns of TAWSS and OSI derived here from the simulations of unsteady flow in four aortic geometries were very similar to the steady WSS patterns.

4.5 Conclusion

The spectral/*hp* element method was used to simulate blood flow in a set of anatomically realistic geometries. In all aortas a pair of coherent vortical structures dominated the flow in the aortic arch, and a streak of high WSS was present on the dorsal side of the descending aorta. Both features were subject to age-related changes, which could be attributed to an age-dependent difference in the degree of aortic taper. The results were not sensitive to the modelling assumptions, including the velocity profile at the aortic root and flow pulsatility.

Chapter 5

Comparison of disease localisation and wall shear stress

This chapter aims to assess the capability of traditional haemodynamic metrics to predict the distribution of atherosclerotic lesions in the rabbit aorta. Concretely, averaged WSS distributions in aortas of immature and mature rabbits, described in chapter 4, are compared with lesion prevalence maps in similar study groups, obtained by Cremers et al. (2011). Since the findings from chapter 2 underscored the importance of evaluating the relation between WSS and lesion maps after minimal processing, the respective distributions are first compared qualitatively. Afterwards, a technique for quantitative comparison of the image pairs is proposed. Changes in the lesion distribution with age are used as a tool to validate the spatial correlation between the localisation of atherosclerotic lesions and haemodynamic metrics.

Section 5.1 explains how Cremers et al. (2011) generated rabbit aortic lesion maps, which are used here as a representation of the disease localisation. The section also introduces techniques for comparison of lesion maps with distributions of haemodynamic metrics. In section 5.2 the results of the comparative analysis are presented. Regions in which a correlation between lesion prevalence and steady WSS exists, are identified and the nature of this correlation is investigated. Finally, in section 5.3, conclusions are drawn for the relation between WSS and atherogenesis, taking into account age-related differences.

5.1 Methods

5.1.1 Disease localisation

Maps of lesion prevalence in descending aortas of immature and mature rabbits were obtained previously by Cremers et al. (2011). Relevant procedures of this study are included here (smaller font; with permission from Dr. S. G. Cremers).

5.1.1.1 Animals and diet

Eight immature (approx. 9.1 weeks old) and nine mature (approx. 6.1 months old) male New Zealand White rabbits (HSDIF strain; Harlan, Bicester, Oxford, UK) were used for the part of the study relevant in the scope of this thesis. The animals were fed 75 g/day of a normal diet supplemented for 8 weeks with 1% w/w cholesterol. Compared to the group used for geometric and haemodynamic analysis (table 3.1) and given rabbits reach sexual maturity around 6 months of age, the mature animals used in the study by Cremers et al. (2011) were still relatively young.

5.1.1.2 Surgical procedures

The animals were euthanised, aortas were cannulated below the origin of the superior mesenteric artery, flushed by retrograde perfusion with Ringer's solution, and then fixed with 10% buffered formalin for 10 min. Subsequently the aortic section from the point of cannulation to the descending part of the aortic arch was excised, cleansed of loose adventitial tissue and divided into descending thoracic and upper abdominal segments. The third pair of intercostal branches was removed for a separate study. Only the descending thoracic segment is relevant in the scope of this thesis.

5.1.1.3 Staining and imaging

The tissue of interest was equilibrated with phosphate buffered saline (PBS), stained for 1 h in a 1% w/v solution of Oil Red O in 60% v/v triethyl phosphate, destained for 30 min in 60% triethyl phosphate and re-equilibrated with PBS. It was then counterstained with 0.003% w/v Evans blue for 1 h and destained for 30 min in PBS. The segments were subsequently opened along the ventral wall, placed on a flatbed scanner with the luminal side facing downwards and scanned at a nominal resolution of 3200 dpi. The lesions appeared red against a blue background.

5.1.1.4 Lesion mapping

The distribution of lesions was quantified with a frequency-mapping technique. Lesion frequency was analysed at a high resolution around the branches and at a lower resolution in the whole aortic

segments (including the same branches). For the regions around the branches, areas of the scanned images equivalent to 2.4×3.6 mm before magnification and centred on the branch ostium, were selected. For the whole segments, the entire scanned image was used.

Each image or sub-image was imported into spreadsheet software using a grid of 20×30 squares for the branches (equivalent to 120 µm in length) and a coarser grid (equivalent to 600 µm in length) for the whole descending thoracic segments. The presence of lesions was recorded by manually selecting the grid squares that had lesions covering more than 50% of their area.

A subset of the lesion maps is shown in figure 1.3.

Mean frequencies were calculated around the intercostal branches and for the entire thoracic segment, and this for both age groups. To obtain the average distributions near the branches, maps were combined using the centre of the ostium as a datum. To obtain the average distributions for the entire thoracic segments, maps were combined using alignments that gave the best superimposition of the branch points. Since the segments had been excised with slightly different lengths, this procedure resulted in the summary map for each group lacking data from increasing numbers of rabbits towards its proximal and distal ends. When calculating the mean frequencies, such regions were not included if they lacked data from more than two animals. The aortic segments also had slightly different widths. This variation was too small to warrant correction.

5.1.2 WSS distributions

Maps of WSS in the thoracic aorta and around intercostal ostia of immature and mature animals were used. Only distributions of steady WSS were considered, given patterns of time-averaged metrics were not distinctly different (section 4.2.4). Details on the animals used for the haemodynamic analysis are summarised in table 3.1. For details on how the WSS maps were obtained, the reader is referred to section 4.1. For the purpose of the current chapter, WSS maps were regenerated to match the resolution of the corresponding lesion maps. Consequently, the numbers of pixels per map differed between the proximal and more distal segments of the thoracic aorta.

5.1.3 Comparative analysis

For intercostal branch regions as well as the descending thoracic aorta of immature and mature animals, the summary maps of lesion prevalence were compared visually

with the averaged maps of WSS. Additionally, the maps of lesion prevalence and averaged WSS were subjected to a more quantitative comparative analysis.

Initially, a straightforward pixel-to-pixel analysis was performed using a linear regression approach, as was also adopted by Joshi et al. (2004), Wentzel et al. (2005) and many other research groups. However, such an analysis is based on a number of assumptions. In particular, its use requires linearity of the relationship between the dependent and independent variables (WSS and lesion prevalence in this application), which is not necessarily justifiable. Figure 5.1 shows scatter plots of the [lesion prevalence, WSS] pairs in the various aortic segments of immature and mature animals. The linear regression lines clearly do not represent the data accurately: the relationship between the two variables is not linear and the data are not normally distributed. For example, a large number of data points away from the immature intercostal ostia have WSS values of around 2.4 Pa, but varying lesion prevalence. These points are grouped around the 2.4 Pa line in figure 5.1(a). Points with high WSS and high lesion prevalence in the upper right corner of the scatter plot represent points downstream of the ostia, while the smaller set of pixels with increased WSS but low lesion prevalence are located upstream of the ostia. For mature intercostal ostia (figure 5.1(b)) the points grouped around the 2.6 Pa line originate from the lateral sides of the ostia. The deviation of this line to higher WSS levels at low lesion prevalence is a result of the region of increase WSS upstream of the ostia. The zone of high WSS downstream of the ostia has medium to high lesion prevalence and covers the right hand side of the scatter plot. At the low WSS end, points located closer to the ostia can be found. In the thoracic aortic maps there are fewer levels of lesion prevalence since the prevalence was calculated for a smaller number of samples (number of aortas instead of number of ostia). As a consequence horizontal lines are visible on the scatter plots of figures 5.1(c)-5.1(f). The linear regression lines do not represent these datasets very well either.

A novel technique for quantitative comparison of the WSS and lesion maps is proposed. The technique was designed to test if two images - i.e. a WSS map and corresponding lesion distribution - are correlated, without pre-imposing any

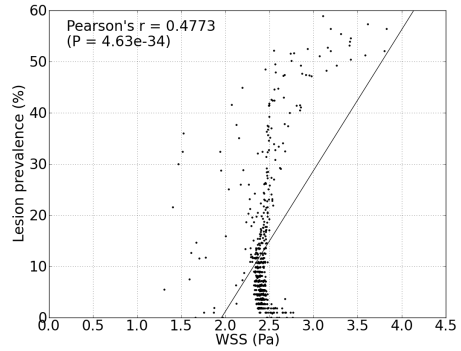

(a) Intercostal ostia (immature)

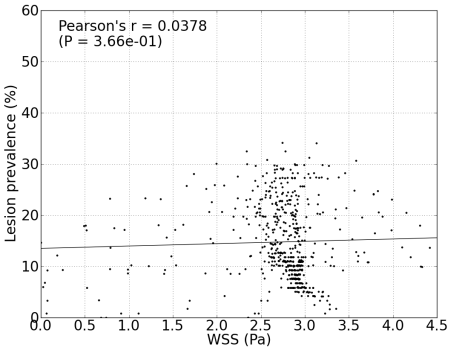

(b) Intercostal ostia (mature)

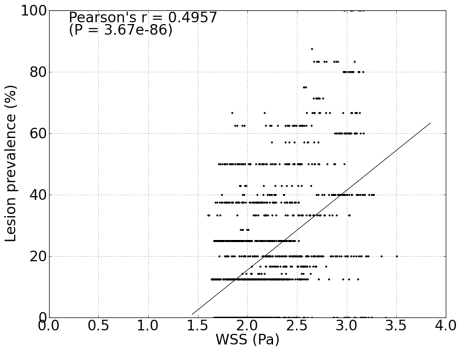

(c) Proximal thoracic aorta (immature)

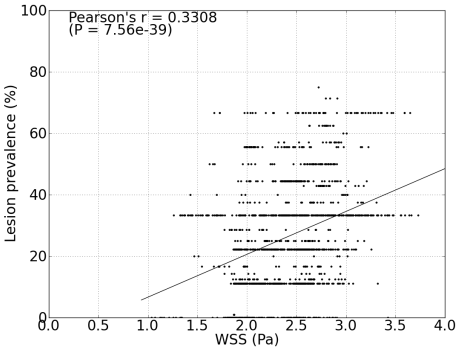

(d) Proximal thoracic aorta (mature)

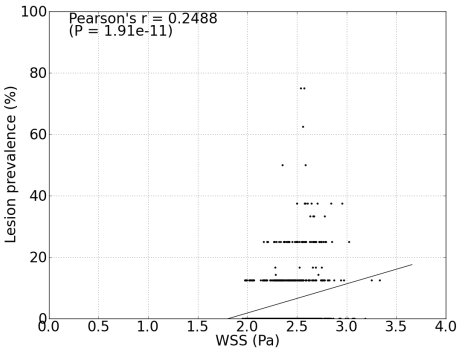

(e) 4^{th}-5^{th} intercostal pairs (immature)

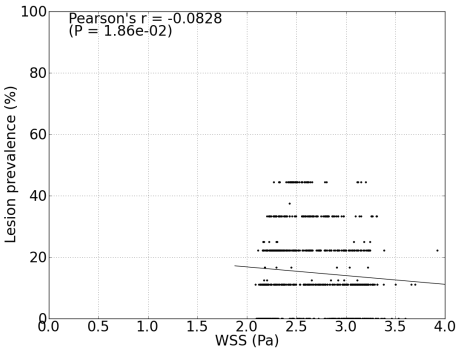

(f) 4^{th}-5^{th} intercostal pairs (mature)

Figure 5.1: Scatter plots of lesion prevalence versus averaged WSS, and lines of linear regression showing how inappropriate a linear analysis is for these data.

requirements (such as linearity) on the nature of the correlation. The algorithm, which will now be explained, is summarised in figure 5.2. At the core of the technique (red box in the figure) is a surrogate data analysis (Theiler et al., 1992). The surrogate data analysis is used to assess how likely it is to obtain a [lesion prevalence, WSS] pair, given two lists of data with the same mean and standard deviation as the lesion prevalence and WSS datasets under investigation, but in which the ordering of one of the datasets has been randomised. The method is illustrated in figure 5.3.

Concretely, a discriminating statistic (which will be defined later) is calculated for the original [lesion prevalence, WSS] data, taking pairs of corresponding pixels in the lesion prevalence and WSS maps. This is schematically indicated in figure 5.3 (left). The pixels of one of the images are then shuffled randomly and the discriminating statistic is recalculated (figure 5.3, top right). The randomisation procedure and subsequent discriminating statistic calculation are repeated n_{sur} times (figure 5.3, right). In this way, a histogram of discriminating statistics can be generated (figure 5.3, bottom). For high enough n_{sur} the histogram is insensitive to n_{sur}. In a final step, the percentile of the discriminating statistic calculated for the *original* datasets, is determined in the histogram of discriminating statistics. This percentile is a measure for the correlation between the lesion prevalence and WSS maps.

Any discriminating statistic which relates the two maps to each other can be used in the data analysis. Here, the sum of the absolute differences between both images (which have non-negative pixel values) was chosen. The images were normalised first, turning them into probability density functions. This definition of the discriminating statistic is best-suited for monotonic correlations; in such cases, the discriminating statistic for the original dataset falls in the left-hand side if the correlation positive (e.g. histogram in figure 5.3) and in the right-hand side if the correlation is negative. More involved statistics could be based on, for example, Pearson's correlation coefficient or mutual information (Maes et al., 1997).

Returning to the point-wise comparisons shown in figure 5.1, for all segments except the mature intercostal ostia a significance test of zero regression and correlation resulted in a rejection of the null hypothesis, often with very low P-values, despite

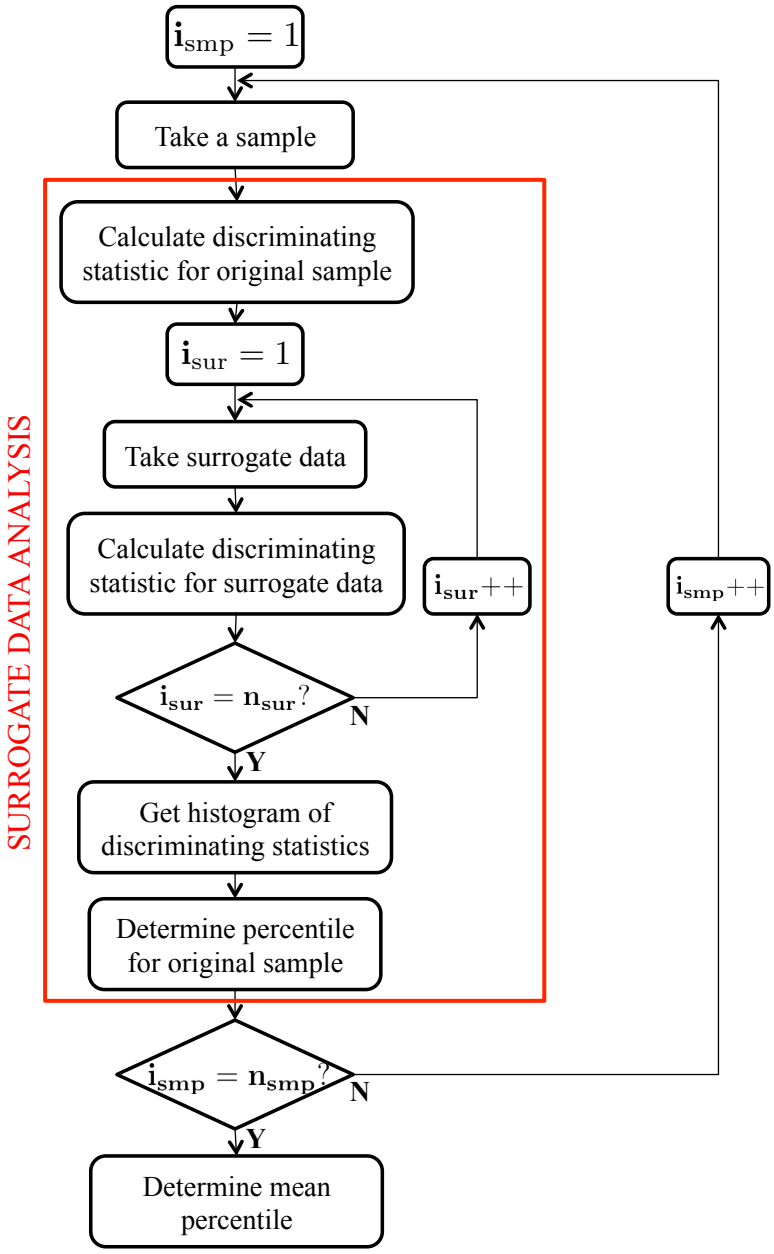

Figure 5.2: Flow diagram of a novel technique for quantitative comparison of WSS and lesion prevalence data.

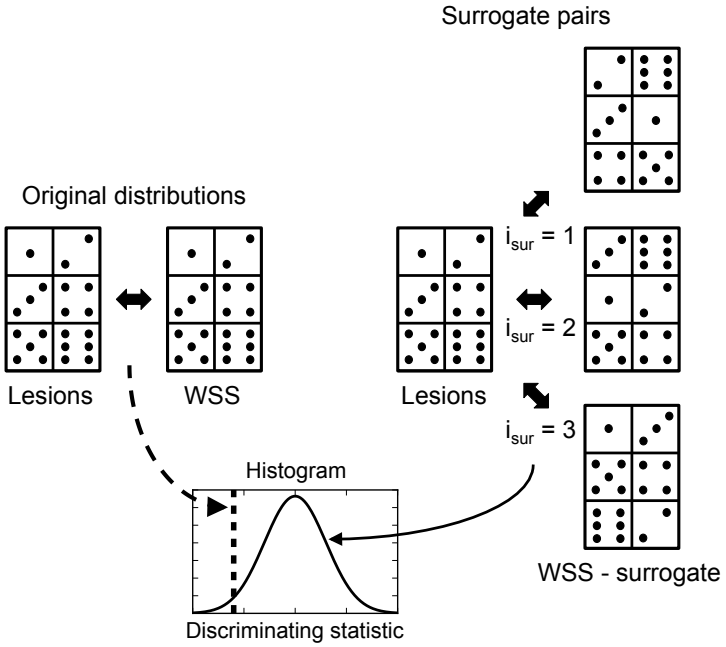

Figure 5.3: Illustration of the surrogate data analysis. The images on the left represent 3×2 maps of lesions and WSS. Corresponding pixels in the two maps are marked with matching numbers of dots. Three sets of surrogate data, generated by shuffling the pixels from the WSS map, are shown ($n_{\mathrm{sur}} = 3$). This results in 3 surrogate data pairs, as shown on the right. A discriminating statistic is calculated for each of the surrogate pairs, resulting in a histogram in which the percentile of the discriminating statistic calculated for the original pair can be determined (bottom, the histogram shown here is only illustrative). The dotted line indicates the statistic calculated for the original data; its position on the histogram determines the P-value.

of the poor visual correlation. The resolution of the maps influences the statistical power of the analysis: in the case of the immature intercostial ostia, for example, the P-value increased from 4.63×10^{-34} for the (30×20) maps, to 1.42×10^{-10} for (15×10) maps or 2.85×10^{-8} for (8×5) maps. This is a consequence of the spatial autocorrelation in the image pairs, which for example makes that pixels close to a pixel with a high lesion prevalence are more likely to contain lesions as well. The level of autocorrelation depends on the resolution, or number of pixels of the map: if the map is coarse relative to the gradients in the actual distribution of the variable, neighbouring pixels are less dependent on one other. For this reason, and because the number of pixels s_{map} $(= m \times n)$ influences the statistical power of the analysis, the resolution of the map is important.

The surrogate data method does not solve this problem, but a workaround can be built in. As the flow diagram in figure 5.2 indicates, the surrogate data analysis can be applied to selections of pixels, or *samples*, one at a time rather than to all pixels at once. This is also illustrated in figure 5.4. The sample selection introduces a second level of randomisation: n_{smp} random samples are chosen (figure 5.4, left) and the surrogate data analysis is performed on each of these samples (figure 5.4, right). The median percentile P of all surrogate data analyses is then taken as a measure for the correlation between the lesion prevalence and WSS maps. The null hypothesis, which states that the maps are uncorrelated, is rejected if $P < 0.05$.

Using this approach it is the sample size (s_{smp}) which determines the significance of the test. The sample size should be chosen so that the average distance between pixels in the sample matches the average distance at which pixels in the original map become de-correlated. With l_{dec} the de-correlation length, the sample size could then be calculated as:

$$s_{\text{smp}} = \frac{s_{\text{map}}}{{l_{\text{dec}}}^2}. \tag{5.1}$$

A number of techniques have been proposed in the literature to estimate the degree or length scale of the spatial autocorrelation in an image, including the use of Moran's I (Moran, 1950) or the Euler characteristic (Brett et al., 2003). Here, a tailored approach is suggested to estimate l_{dec}. First, for each pixel (except

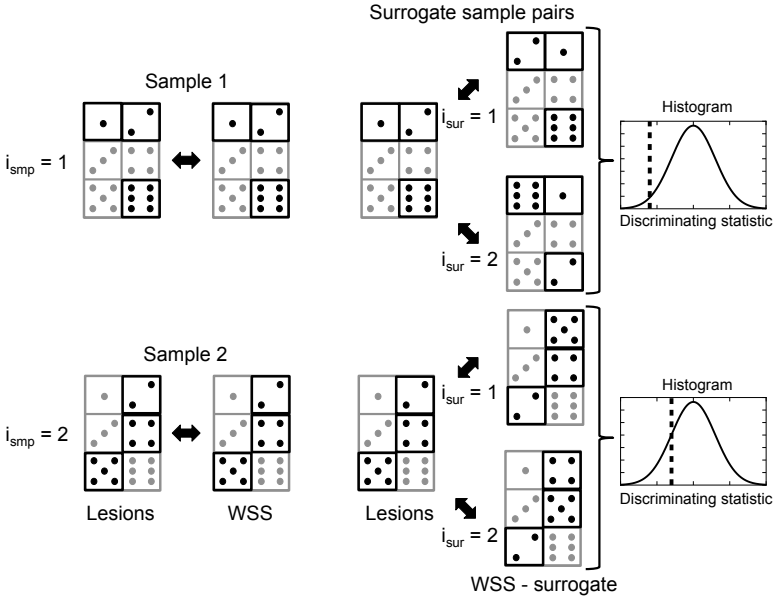

Figure 5.4: Illustration of the surrogate analysis on samples of [lesion, WSS] data. Samples of the original dataset (indicated by the grid squares outlined in bold lines) are selected (left, $n_{\mathrm{smp}} = 2$), and a surrogate data analysis ($n_{\mathrm{sur}} = 2$) is applied on each of these samples (right). The median of the results of all surrogate data analyses is taken as a measure for the spatial correlation between the lesion and WSS maps.

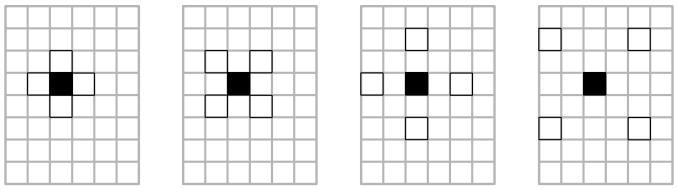

Figure 5.5: The average distance at which pixels become de-correlated was determined based on summary statistics on the correlation between pixels and their direct neighbours (left), their diagonal neighbours (middle left), pixels at a distance of 2 pixels lengths (middle right), pixels at a distance of $2\sqrt{2}$ pixels lengths (right), and so on, up to an inter-pixel distance of 4.

those at the border) the four neighbouring pixels are selected. This is schematically illustrated for one pixel (coloured black) in figure 5.5 (left). A sample Z-score for the central pixel is calculated based on the five pixel values:

$$Z = \frac{x_{\text{cnt}} - \mu_5}{\sigma_5} \tag{5.2}$$

where x_{cnt} represents the central pixel value, and μ_5 and σ_5 the mean and standard deviation for the five pixel values. A sample Z-score with a high absolute value implies that the central pixel has a value that is very different from its neighbours, while a sample Z-score with a low absolute value can indicate a uniform field or opposing gradients which average out. Since a sample Z-score is calculated for each pixel of the image (except those at the border), an average sample Z-score over the image can be determined, resulting in a summary statistic for the correlation between pixels and their immediate neighbours. The procedure is repeated for the four pixels diagonal to the central pixel, as indicated in figure 5.5 (middle left), then for an inter-pixel distance of two pixel lengths (figure 5.5, middle right), and so on, up to a maximum inter-pixel distance of four. (Beyond these distances, pixels were considered intrinsically uncorrelated.) A maximum inter-pixel distance, or equivalently a minimum sample size, was set to avoid the problem of under-resolving the image. The smallest distance corresponding to the maximum average sample Z-score is now chosen as the average distance at which pixels are no longer correlated, l_{dec}.

The technique was successfully verified on block pattern images, identifying a

de-correlation length of 1 pixel size for a 1×1 checkerboard pattern, 2 pixel sizes for a 2×2 checkerboard pattern, etc. A line pattern containing alternate rows (or columns) of zero and non-zero values resulted in a de-correlation length of $\sqrt{2}$ pixels, which is again intuitively correct since pixels are correlated in the horizontal (vertical) direction but not in the perpendicular direction. For uniform images or images with a uniform gradient the technique does not suggest a de-correlation length. Since the presence of noise influences the de-correlation length, the technique was applied to the WSS maps, which are less prone to noise than the lesion prevalence maps. The de-correlation length l_{dec} was $2\sqrt{2}$ pixels for the maps around mature intercostal ostia and at the level of the fourth and fifth intercostal pairs, 4 pixels for the map around immature intercostal ostia, and $3\sqrt{2}$ pixels for all other maps.

5.2 Results

This section describes the results of the comparative analysis of WSS and lesion prevalence maps. The findings of the visual, qualitative analysis are discussed first, followed by an overview of the results of the novel quantitative approach. Figures 5.6 and 5.7 summarise the results for the intercostal branch regions and descending thoracic segments respectively.

5.2.1 Qualitative analysis

In immature animals the most diseased region was a triangular zone downstream of the ostium, where the WSS reached its maximum. There was more variation in the distribution of near-branch lesions in mature animals. Although mean lesion maps indicated that the lateral margins of ostia are the most athero-prone regions, lesions also developed upstream or downstream in some animals (figure 1.3). This contrasts with the mature WSS distribution: the pattern - high WSS downstream and to a lesser extent upstream of the ostium - was similar to the immature one, and was very consistent.

At the level of the first to fourth pairs of intercostal arteries, lesions away from the branches in the descending thoracic aorta were located mainly on the dorsal side.

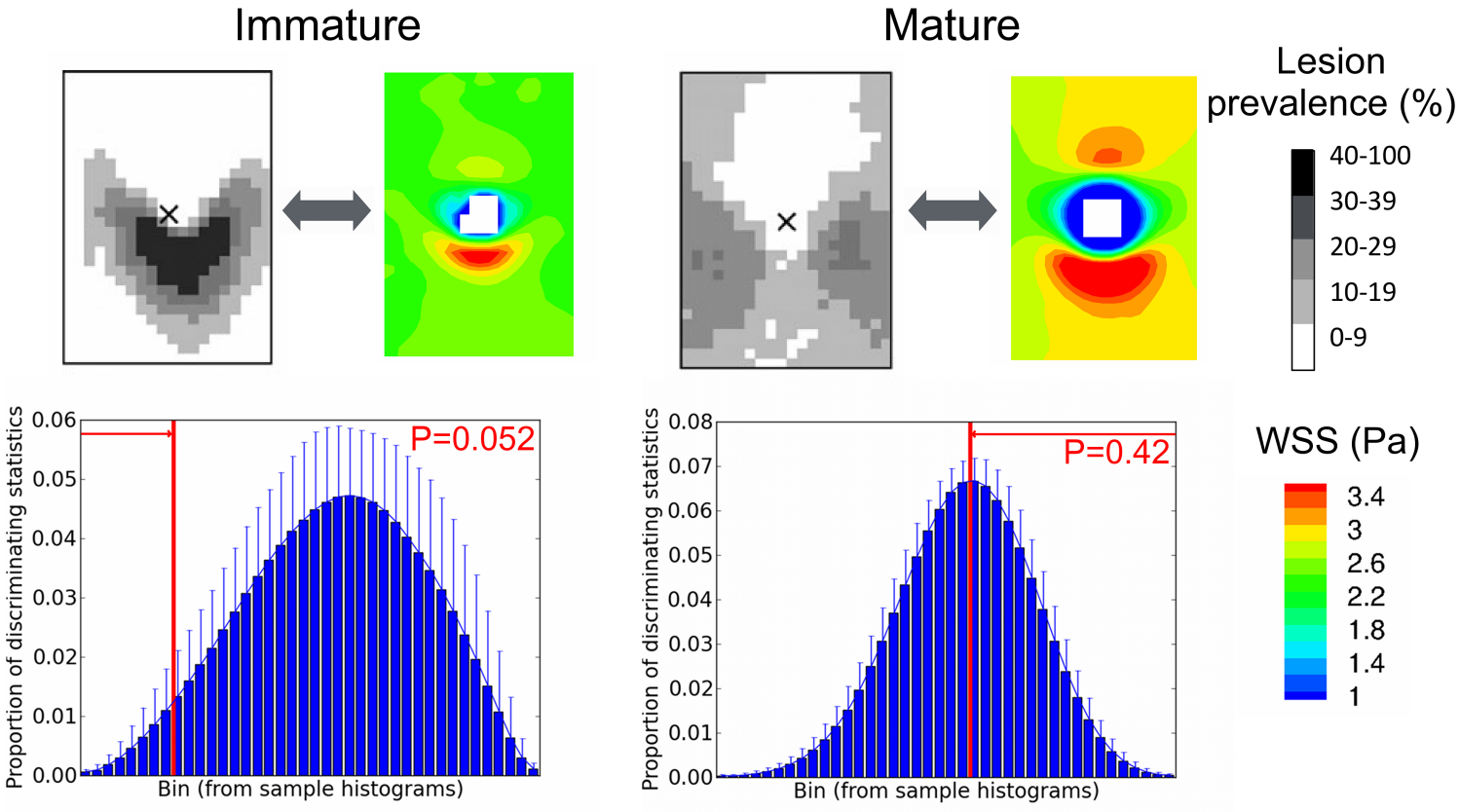

Figure 5.6: Comparative analysis of lesion prevalence and WSS maps around intercostal ostia. Greyscale and colour maps show lesion prevalence (reproduced with permission from Cremers et al. (2011)) and WSS respectively, averaged for immature (left) and mature (right) animals. Maps are shown *en face*, and aortic flow is from top to bottom. X marks the ostial centre in the lesion prevalence maps. The graphs summarise the quantitative analysis, and were obtained by combining the normalised histograms for the various samples. Each bin represents the mean+SD of the corresponding bins in the normalised histograms. The null hypothesis states that the lesion and WSS maps are uncorrelated. The red line marks the percentile of the discriminating statistic calculated for the original dataset; the corresponding numerical value is also given.

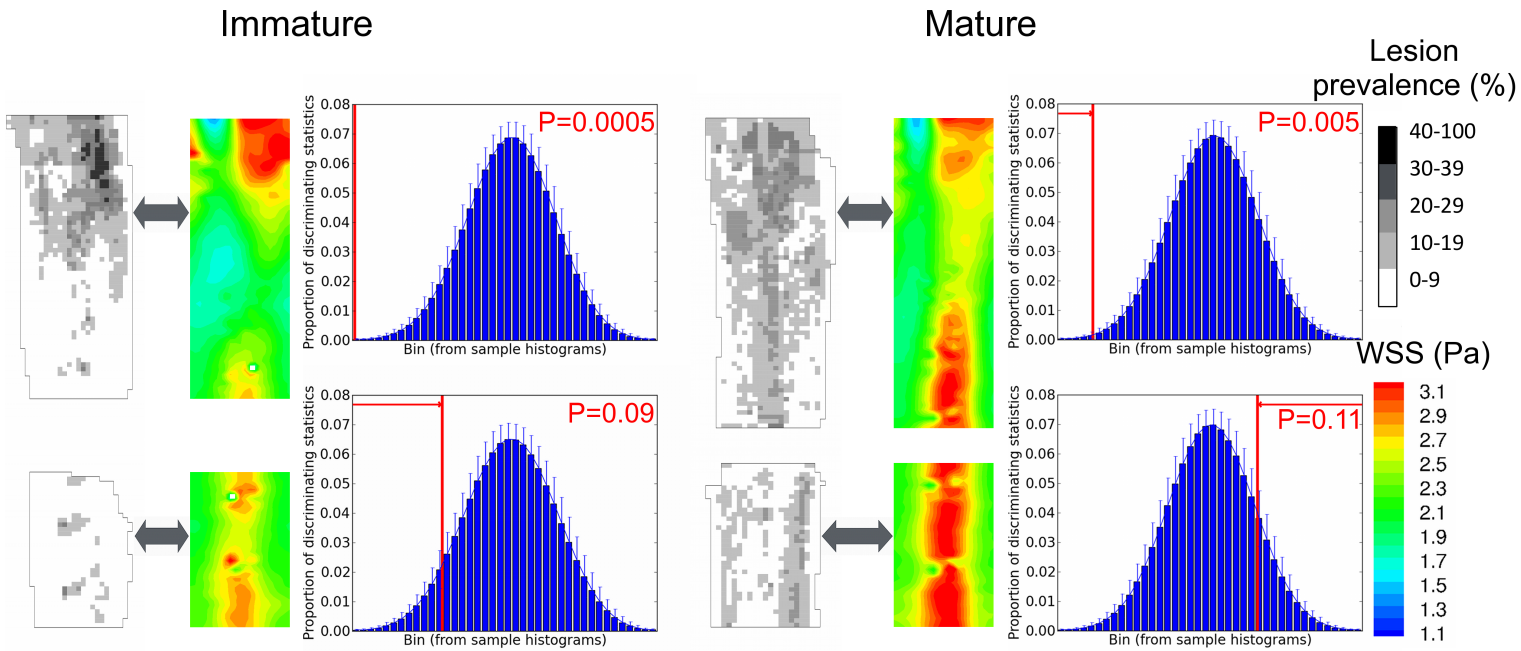

Figure 5.7: Comparative analysis of lesion prevalence and WSS maps in segments of the descending thoracic aorta. Greyscale and colour maps show lesion prevalence (reproduced with permission from Cremers et al. (2011)) and WSS respectively, averaged for immature (left) and mature (right) animals. Maps are shown *en face*, and aortic flow is from top to bottom. The graphs summarise the quantitative analysis, and were obtained by combining the normalised histograms for the various samples. Each bin represents mean+SD of the corresponding bins in the normalised histograms. The null hypothesis states that the lesion and WSS maps are uncorrelated. The red line marks the percentile of the discriminating statistic calculated for the original dataset; the corresponding numerical value is also given.

This trend was particularly pronounced in mature animals, although outliers exist in both age groups. The dorsal location corresponds to the location of a streak of high WSS. This streak was more pronounced in the mature animals. Further downstream, a shift to the ventral side was observed in the maps of lesion prevalence (particularly so in mature animals), but not in the distribution of the WSS.

5.2.2 Quantitative analysis

As appears from figure 5.6, there was no correlation between lesion prevalence and WSS around intercostal ostia of mature rabbits ($P = 0.42$), while there was a trend for the lesion prevalence and WSS maps to be correlated around intercostal ostia of immature animals ($P = 0.052$).

Figure 5.7 shows that a good correlation between lesion prevalence and WSS was found in the proximal descending aorta ($P = 0.0005$ in immature and $P = 0.005$ in mature animals), but the correlation was not maintained further downstream ($P = 0.09$ in immature and $P = 0.11$ in mature animals). Since the correlation changed from a positive to a (non-significant) negative one in the mature animals, the discriminating statistic for the original dataset moved from the left-hand tail to the right-hand tail of the histogram.

5.3 Discussion

As discussed in detail in chapter 2, it is often regarded an established fact that lesions occur in areas of low WSS. The results of this chapter do not support the low shear theory. Around intercostal ostia of immature rabbits lesions even seemed to occur more frequently in zones of high WSS. This observation, however, was only borderline significant due to the absence of lesions in the region of increased WSS immediately upstream of the branch opening. Moreover, the change in pattern with age in lesion prevalence was not matched by a change in the WSS distribution, resulting in uncorrelated lesion prevalence and WSS maps around intercostal ostia of mature rabbits.

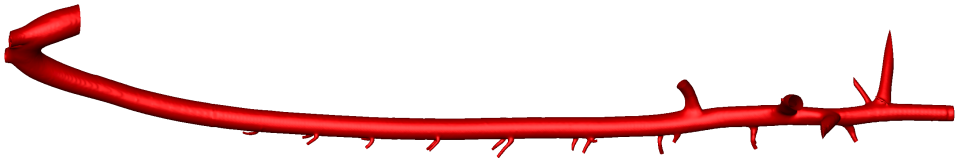

Figure 5.8: Reconstruction of the ascending aorta, aortic arch and descending aorta (down to the renal branches) of animal VPADP091214. Note that the first intercostal branch pair is not visible.

For the coarser descending thoracic maps a good, albeit not simply linear, correlation was found in the proximal descending aorta. Once more visual observation showed a better colocation of high lesion prevalence with high rather than low shear, and this on the dorsal side of the vessel. Further downstream a shift to the ventral side was observed in the lesion prevalence maps, particularly for mature animals. This shift was not present in the WSS maps, and as a consequence no spatial correlation was found in this region for both age groups. Since the shift in the lesion pattern occurred towards the end of the aortic section considered in the CFD simulations, a section extending further downstream was scanned at a lower resolution for one of the animals (voxel size of 91.2 µm). The reconstructed geometry is shown in figure 5.8. No abrupt geometric changes were observed immediately downstream of the fifth intercostal branch pair. Changes in aortic curvature at the level of the coeliac artery and the flow towards these branches will affect the aortic flow, but are not expected to have a significant effect as far upstream as the region of the fourth and fifth intercostal branch pairs.

As the conclusions presented here are not in agreement with the general consensus theory, it is instructive to consider why this is the case, accepting that the maps of lesion prevalence were obtained in a rigorous fashion (Cremers et al., 2011) and that the WSS patterns were insensitive to modelling assumptions (section 4.4).

Firstly, it should be noted that the concept that lesions would develop in regions of high WSS is not new: an early theory of localising factors in atherosclerosis also suggested that lesions develop in regions of high WSS (Fry, 1969). However, neither this theory nor the current general consensus theory have taken into account the age-related changes in lesion location that are now known to occur, not only in

rabbit but also in human aortas (Weinberg, 2002).

Secondly, as highlighted in section 2.4, there are important inconsistencies in the levels of data reduction used in the literature. In the present work a rigorous method for detailed quantitative comparison was proposed and applied, while results were also evaluated after minimal processing. The method proposed here, which is derived from techniques used to test for non-linearity in time series data (Theiler et al., 1992) and functional imaging analysis (Brett et al., 2003; Nichols and Holmes, 2002), avoids unjustified assumptions made, often implicitly, in previous analyses. In particular, the assumption of a linear relation between disease severity and WSS magnitude is avoided. Moreover, the method overcomes the effects of the frequently-overlooked dependency between data points without having to choose arbitrary thresholds to dichotomise the data (Chatzizisis et al., 2008; LaMack et al., 2010) or average over large patches.

Finally, translation of results from one species to another might not be straightforward. However, since lesions are also reported to occur downstream of intercostal branches in immature human aortas (Sinzinger et al., 1980) and to be most prevalent on the dorsal wall of the descending thoracic segment of mature human aortas (Svindland and Walløe, 1985), the present data cannot *a priori* be regarded as relevant only to experimental atherosclerosis in laboratory animals; the relation between WSS and lesions at these locations in people requires further investigation.

5.4 Conclusion

A comparative analysis of lesion prevalence and WSS in aortas of immature and mature rabbits was presented. Maps were compared visually, and a novel method for quantitative comparison was developed to avoid the requirement of certain assumptions (such as linearity) on the nature of the relationship. Randomised sampling was used to ensure the independence of data points, another basic assumption of commonly-used statistical methods that is often disregarded. The results did not support the low shear theory of atherosclerosis. In the proximal descending aorta lesions even occurred more frequently in regions of high WSS. This was also the

case around intercostal ostia in immature animals, although the correlation did not reach the significance level here. Age-related changes around branch ostia were not explained by the flow patterns.

Chapter 6

A novel technique to characterise multi-directional flow

CFD simulations of blood flow in arteries have been widely used to investigate the relation between disease and WSS and, owing to decreasing computer power:cost ratios, more and more realistic configurations can be considered (Xiong et al., 2011; Rikhtegar et al., 2012). Over the years haemodynamic metrics of increasing complexity have been suggested to be of physiological importance. However, a selection of metrics has been favoured. This chapter questions if the traditional metrics do indeed have the potential to elucidate the most relevant aspects of the flow field.

Section 6.1 considers three different flow environments and investigates if the most commonly used haemodynamic metrics can distinguish between these flow environments. Based on the results of this analysis, a novel metric is introduced in section 6.2. The metric is subsequently applied to pulsatile flow in an idealised branching geometry and in aortas of immature and mature rabbits. Distributions of the various metrics are presented in section 6.3. Section 6.4 discusses implications for the study of cardiovascular disease.

6.1 The importance of flow multi-directionality

Without attempting to be exhaustive, the introduction of chapter 2 provided an overview of haemodynamic metrics that have been suggested to link blood flow and atherosclerosis. Whereas initially the literature focused on the the steady-state or time-averaged magnitude of the wall shear stress (WSS or TAWSS), the OSI was introduced later "to describe the shear stress acting in directions other than the direction of the temporal mean shear stress vector" (Ku et al., 1985). This was done to explore the effects of flow pulsatility on haemodynamic forces acting on the endothelial surface, and because it was realised that both low mean shear stress and oscillatory shear stress contribute to an increased fluid residence time. An increase in residence time may in turn result in modification of the mass transport of atherogenic substances between lumen and wall or in interference with endothelial metabolism (Ku et al., 1985).

Since the introduction of the OSI, biological evidence has indeed shown that endothelial cells react to conditions of flow reversal (Chien, 2008). Moreover, endothelial cells behave differently when exposed to flow without a definite direction, in contrast to shear with a clear direction (whether resulting from steady or pulsatile flow). For example, porcine aortic endothelial cells cultured under oriented shear stress are more elongated and less compliant than cells grown under static conditions or under shear stress with no preferred orientation (Potter et al., 2012).

Although the OSI was introduced to quantify the extent of disturbed flow and has been used frequently for this reason, it should be emphasised that neither the OSI nor other similar metrics are able to distinguish between simple uniaxial flows (which can be purely forward flowing or reversing) and multi-directional flows. To illustrate this, figure 6.1 shows three different flow environments endothelial cells could be exposed to: purely unidirectional flow without reversal, unidirectional flow with reversal, and multi-directional disturbed flow[1]. The examples have been chosen to yield identical TAWSS, implying that the TAWSS cannot capture the differences between the three

[1]The time-harmonic aspect of the flow could also be of interest (Himburg and Friedman, 2006), but is not covered here.

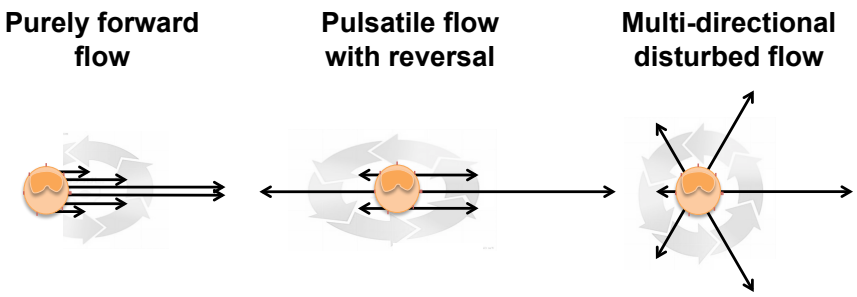

TAWSS:	2.5	2.5	2.5
OSI:	0	0.367	0.367
RRT~	1	3.76	3.76
TransWSS:	0	0	1.1547

Figure 6.1: Three different flow environments to which an endothelial cell could be exposed. The black arrows represent WSS vectors at various times in the cardiac cycle. The grey arrows indicate their evolution with time. The table lists TAWSS (Pa), OSI (-), RRT (relative to purely forward flow) and transWSS (Pa) for the three environments.

flow environments. Indeed, recalling the definition of the TAWSS in equation (1.11), the TAWSS does not have this potential since all directional information in the instantaneous WSS vector $\boldsymbol{\tau}_w$ is lost by taking the vector magnitude.

The definition of the OSI, equation (1.12), ensures that purely forward flow as in figure 6.1 (left), is identified with OSI = 0. The OSIs of the two other cases in figure 6.1 are both non-zero, indicating that the flow changes direction or sense. However, the OSI is not a suitable metric for identifying the multi-directional case since it is not capable of separating it from the unidirectional flow with reversal (OSI = 0.367 for both cases). A similar reasoning holds for the RRT, which is also listed in the table at the bottom of figure 6.1.

The fact that traditional metrics cannot identify the multi-directional character of a flow field may hamper our understanding of *disturbed* arterial flow and its role in the initiation of atherosclerosis. A method that has this potential could complement existing metrics, thereby helping investigations of the importance of flow directionality.

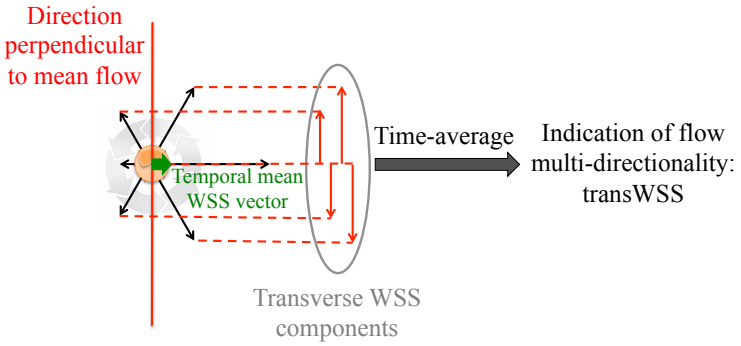

Figure 6.2: Schematic diagram of the calculation of the time-averaged transverse WSS. To the left, black arrows represent WSS vectors at various times in the cardiac cycle, and grey arrows indicate their evolution with time. The meaning of other arrows and lines are indicated on the diagram.

6.2 Methods

As traditional metrics cannot fully characterise multi-directional flow, a new metric that has this capacity when used in combination with existing metrics, is introduced in this section. Idealised and physiologically realistic environments in which the metric was applied, are also set out.

6.2.1 Time-averaged transverse WSS

A characteristic of multi-directional disturbed flow is that $\boldsymbol{\tau}_w$ does not remain parallel to a single axis throughout the cardiac cycle. Hence, only such flows have non-zero WSS components in the direction normal to the temporal mean vector. The calculation of the time-average of the magnitudes of these components results in the *time-averaged transverse WSS* (transWSS) and is schematically depicted in figure 6.2. Mathematically, this leads to the following definition:

$$\text{transWSS} = \frac{1}{T}\int_0^T \left|\boldsymbol{\tau}_w \cdot \left(\mathbf{n} \times \frac{\int_0^T \boldsymbol{\tau}_w \mathrm{d}t}{\left|\int_0^T \boldsymbol{\tau}_w \mathrm{d}t\right|}\right)\right| \mathrm{d}t \tag{6.1}$$

The transWSS can take any value between 0 and its theoretical maximal value, which is equal to TAWSS, so long as there is a preferred flow direction. A low transWSS indicates that the flow, which can be steady, pulsatile or oscillatory,

remains approximately parallel to a single axis throughout the cardiac cycle. A high transWSS indicates large changes in flow direction, smaller changes in direction but over a larger portion of the cardiac cycle, or small changes in direction of a high-speed near-wall flow. As the examples in figure 6.1 suggest, transWSS does not differentiate between purely forward and reversing unidirectional flow. It therefore does not replace TAWSS, OSI or RRT, but rather complements them.

6.2.2 Applications in arterial flow

The transWSS was calculated for the idealised models of pulsatile flow in an intercostal branch region presented by Kazakidi et al. (2011), and for pulsatile flow in four rabbit aortas.

The computational domain from Kazakidi et al. (2011), is shown in figure 6.3. Three combinations of boundary conditions at the aortic inflow and side-branch outflow were considered:

- Case I: Steady aortic flow with pulsatile but non-reversing side-branch flow;
- Case II: Steady aortic flow with pulsatile reversing side-branch flow;
- Case III: Pulsatile aortic flow that reversed near the wall but not at the centreline, with pulsatile non-reversing side-branch flow.

At the aortic inlet and along the lateral planes of the computational domain, a parabolic velocity profile was imposed, with its peak velocity at the bottom plane of the domain (opposite to the aortic wall). For pulsatile flow conditions this profile was complemented by a time-dependent component, consisting of a single sinusoidal harmonic. For more details on the imposed velocity profiles, the reader is referred to Kazakidi et al. (2011). The (mean) inflow Reynolds number $\mathrm{Re}_{\mathrm{in}}$ was 500 for all cases. A flow split of 0.79%, based on the average inflow rate, was applied at the side branch outlet, where a Womersley profile was imposed. At the aortic outlet a zero pressure gradient was specified, and the no-slip condition was applied on the aortic and side-branch walls.

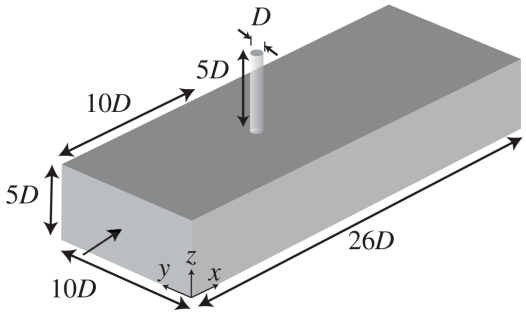

Figure 6.3: Computational domain representing an intercostal artery emerging perpendicularly from the thoracic aorta. The aortic inlet is located at $x = 0$. After Kazakidi et al. (2011).

For details on the simulations of pulsatile flow in rabbit aortas, the reader is referred to section 4.1.3.3. Briefly, pulsatile flow with $\mathrm{Re_{in}} = 300$ was simulated in the aortic geometries of two immature and two mature rabbits.

6.3 Results

6.3.1 Pulsatile flow in an idealised geometry

The distributions of the TAWSS, OSI, RRT and transWSS for the 3 simulation cases are visualised in figure 6.4. The TAWSS and OSI distributions were discussed in detail by Kazakidi et al. (2011). (Note that there is some ambiguity regarding the distribution of the OSI for case II.) RRT was increased in regions of low and oscillatory shear, and there were no distinct differences in its pattern between cases. For all three simulations transWSS was increased in a circumscribed region downstream of the ostium, colocating with the zone of increased OSI, and to the lateral sides of the ostium. Whereas for cases I and III the latter zones reached their maximum transWSS away from the branch opening, for case II the two zones started at the branch rim, forming lobes on either side of the ostium.

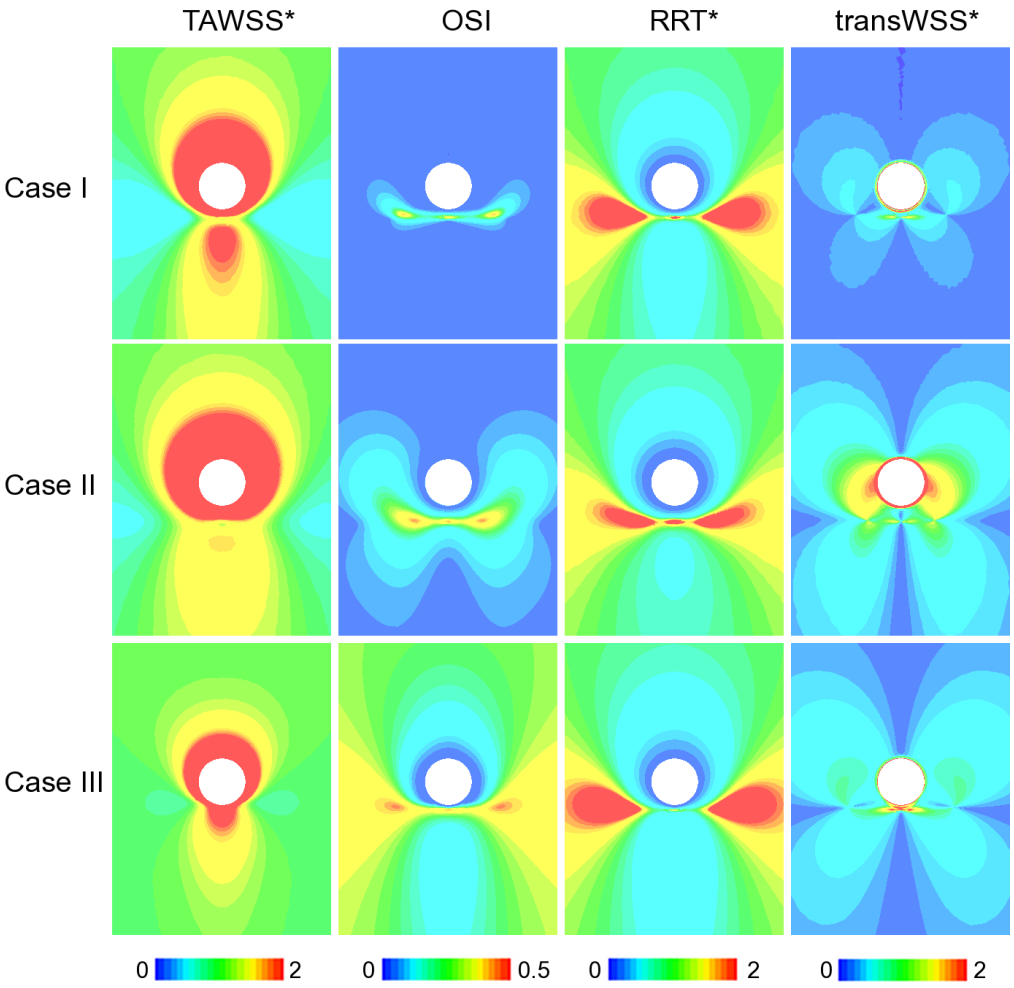

Figure 6.4: Distributions of four haemodynamic metrics on the aortic wall of the idealised branching geometry presented by Kazakidi et al. (2011). The different rows represent different sets of boundary conditions: steady aortic flow with non-reversing (case I) or reversing (case II) side-branch flow, or pulsatile aortic flow with non-reversing side-branch flow (case III). Net aortic flow for each plot is from top to bottom. TAWSS* and transWSS* were normalised using the TAWSS at the aortic inlet; RRT* was normalised using the RRT at the aortic inlet.

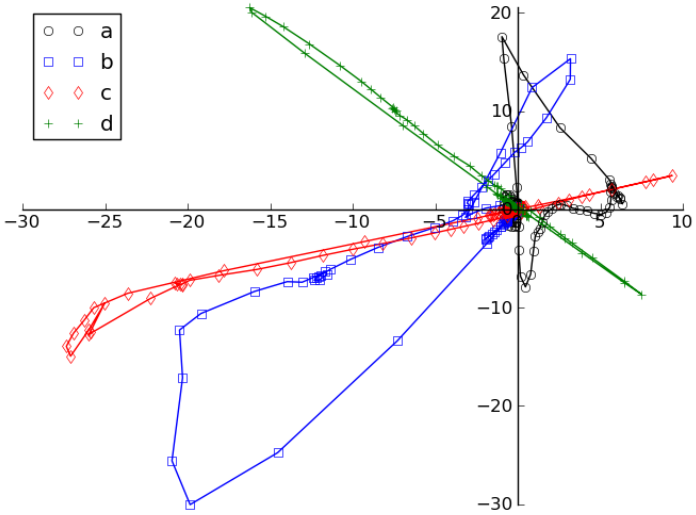

Figure 6.5: Two-dimensional WSS vector traces (Pa) for four points in the aorta of rabbit VPADP100209. Locations of the four points are indicated on the TAWSS map in figure 6.6: point a is located along the outer curvature of the ascending aorta, point b in the inner curvature of the aortic arch, point c on the dorsal side of the proximal descending aorta, and point d on the ventral side of the descending aorta.

6.3.2 Pulsatile flow in rabbit aortas

The directionality of the near-wall flow and of the corresponding wall shear stress varied greatly with location in the aorta. Figure 6.5 shows the trace of the WSS vector for four points in the aorta of rabbit VPADP100209. Whereas in the distal thoracic aorta the flow was unidirectional with flow reversal, more variation in the direction normal to the mean flow occurred in the proximal region. In the aortic arch region the flow was truly multi-directional.

The distributions of TAWSS and OSI, averaged for two immature and two mature animals, were compared in section 4.2.4. It was concluded that both time-averaged patterns were very similar to their steady equivalent. In figure 6.6 the distributions of the TAWSS, OSI, RRT and transWSS are shown for the aorta of rabbit VPADP100209. TAWSS was low, and OSI and RRT were high along the greater curvature of the ascending aorta, on the inner wall of the aortic arch and along two

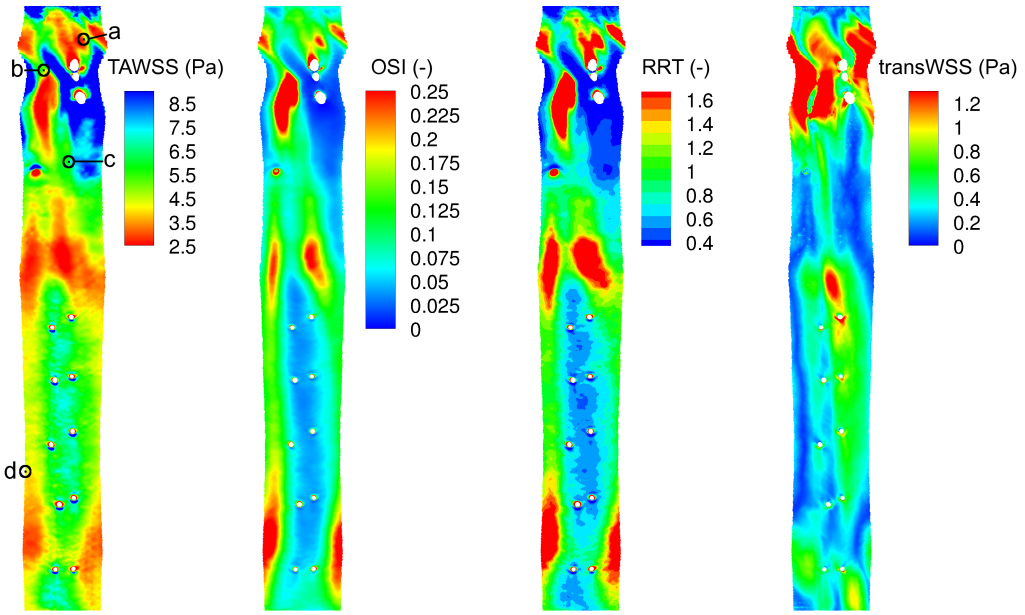

Figure 6.6: Distributions of four haemodynamic metrics in the aorta of rabbit VPADP100209. The luminal surface of each segment, opened ventrally whilst preserving tapering, is shown *en face*. The colour scale of the TAWSS map was inverted for ease of comparison. The letters on this map refer to the selection of points used in figure 6.5. Net aortic flow is from top to bottom.

separate stripes in the descending aorta proximal to the first intercostal branch pair. The latter regions were narrower on the OSI map than on the TAWSS and RRT maps. The regions identified by the transWSS as regions of multi-directional flow were in similar areas, although displaced with respect to those characterised by low and oscillatory shear. In particular, transWSS was also high on the lateral sides of the aortic arch but the stripes proximal to the first intercostal branch pair were replaced by a single dorsal stripe. In the descending thoracic aorta, multi-directional flow was found along the left dorsal side, and was most pronounced at the level of the most proximal intercostal ostium. A close-up of this region is shown in figure 6.7. Away from the immediate vicinity of the ostia in this figure, TAWSS and OSI were again essentially inversely related. Around the left ostium, however, the simple relation between the indices broke down. TAWSS was low and OSI high in a ring closely surrounding the left ostium, implying slowly moving, oscillatory near-wall flow, but further downstream, where the boundary layer reestablishes, OSI was not strikingly

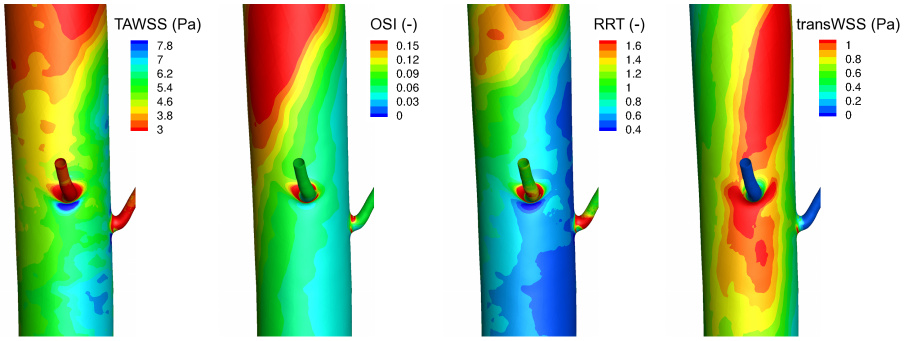

Figure 6.7: Distributions of 4 haemodynamic metrics around the proximal left intercostal branch ostium of rabbit VPADP100209. The colour scale of the TAWSS map was inverted for ease of comparison.

low even though TAWSS reached a maximum. The distribution of the RRT was in agreement with these observations. TransWSS was high in an arrowhead-shaped region downstream and to the sides of the ostium. This area encloses the zone of maximal TAWSS, but TAWSS was less elevated elsewhere within this area, implying greater changes in flow direction.

Figure 6.8 shows transWSS distributions in aortas of two immature and two mature animals. The map on the left corresponds to the TAWSS map in figure 6.6 for animal VPADP100209. In the three aortas on the right, two streaks of increased transWSS are clearly visible in the descending section. The two streaks appeared to start more upstream in mature than in immature rabbits. The interaction of the streaks with the intercostal ostia gave rise to a range of different patterns around the ostia. In contrast with near-ostial zones of elevated TAWSS, which were found immediately downstream of the ostia, patterns of transWSS were generally skewed with respect to the aortic centreline. To analyse differences in patterns, the distributions around selected ostia are shown with adjusted colour scaling in figure 6.9. An arrowhead-shaped zone of high transWSS developed below and to the sides of some ostia, as is shown in figure 6.7. In these cases, transWSS reached its maximum in a circumscribed region downstream of the ostium, as can be appreciated from figure 6.9b. In other cases, for example for the ostium shown in figure 6.9c, the region of elevated transWSS was confined to a zone close to the downstream lip of the ostium.

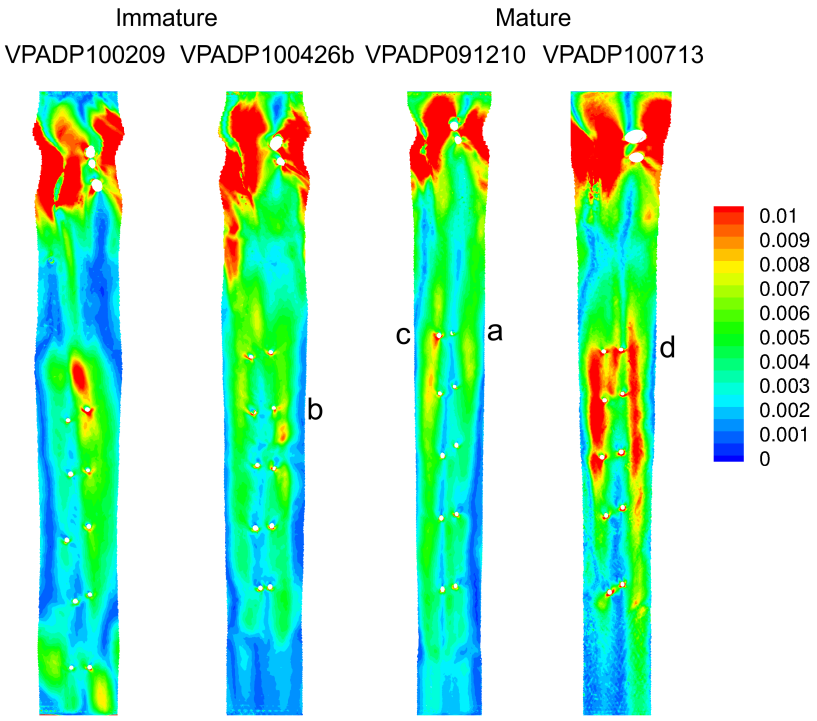

Figure 6.8: Distribution of transWSS ($\times \rho u^2$) in aortas of two immature and two mature rabbits. The luminal surface of each segment, opened ventrally whilst preserving tapering, is shown *en face*. Letters refer to the intercostal ostia shown in figure 6.9.

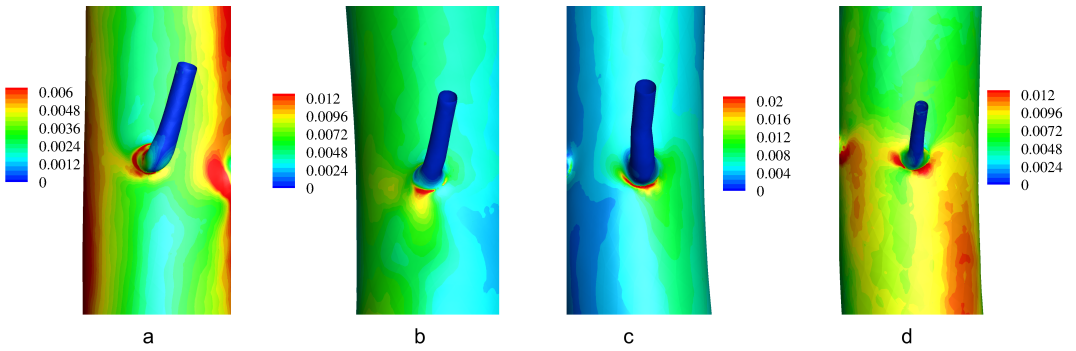

Figure 6.9: Distribution of transWSS ($\times \rho u^2$) around four intercostal ostia. The selected ostia are indicated in figure 6.8. The colour scale range was adapted to the maximal transWSS for each ostium individually.

Alternatively, two lobes of increased transWSS existed in the region downstream or to the lateral sides (figure 6.9a and 6.9d). For the ostium shown in figure 6.9a, one of these lobes was dominant.

6.4 Discussion

The concept that *disturbed* blood flow plays a role in atherosclerosis is well established in the bioengineering community. At the same time, however, researchers acknowledge the imprecise nature of the term (Lee et al., 2009). Investigations to better characterise disturbed flow have often focused on a limited set of aspects of disturbed flow, in particular low shear magnitudes and the unidirectional oscillatory behaviour. This narrow view may hamper our understanding of disturbed flows and its role in atherosclerosis.

In the eighties McMillan (1985) argued that the contradiction between the high shear theory of Fry (1968) and the low shear theory of Caro et al. (1969) could be explained by a "multi-directional stress atherogenesis model". The hypothesis was substantiated using conceptual biological and fluid mechanical arguments but was, to this author's knowledge, never explored in further detail.

Only recently, a growing interest in the multi-directional disturbed character of arterial flows and its relation to atherosclerosis has emerged.

Gallo et al. (2012) aimed to link the amount of helicity in the bulk flow to traditional risk factors in atherosclerosis. However, using this strategy circumferential variations in the lesion distribution remain unexplained.

Also, Chakraborty et al. (2012) developed a novel directional oscillatory shear index (DOSI) "to quantify the directionality of oscillating shear", and successfully correlated its distribution to the cellular elongation in an orbital shaker model. The DOSI focuses on the relative oscillatory character of the flow in two directions perpendicular to each other, in contrast to the more straightforward definition of the transWSS, which was introduced in this chapter.

The definition of the potential aneurysm formation index (AFI), introduced by Mantha et al. (2006), is more closely related to the definition of the transWSS. However, since the cosine of the angle between the instantaneous WSS and the time-averaged WSS vector is taken, the AFI is completely independent of the WSS magnitude in contrast to the transWSS. Moreover, Mantha et al. (2006) did not consider the time-averaged quantity.

In its current definition, the transWSS is undefined if the flow environment does not have a flow dominant direction. Although in such cases a random direction will be selected due to numerical errors in practical calculations, the definition could be modified to eliminate this mathematical incompleteness. Concretely, an equivalent principal axis could be found based on a principal component analysis, as suggested by Chakraborty et al. (2012).

Evaluation of the transWSS in an idealised branching geometry shows that patterns of transWSS differ from the patterns of traditional haemodynamic metrics. Moreover, the patterns are influenced by the boundary condition imposed at the side branch: for pulsatile but non-reversing side-branch flow transWSS reached its maximum away from the branch opening, whereas the maximum was on the branch rim for reversing side-branch flow. By combining the information available in the maps of TAWSS, OSI and transWSS, the governing flow environment in the different regions of the branching geometry can be characterised. Downstream of the ostium a circumscribed region of multi-directional flow exists (low TAWSS, high OSI and

high transWSS); this is where flow stagnation occurs during at least part of the cycle as explained by Kazakidi et al. (2011). To the lateral sides of the ostium the near-wall flow oscillates around its mean direction without reversing (high transWSS but low OSI).

Also in anatomically realistic thoracic aortas patterns of transWSS showed distinctive differences compared to those of traditional metrics. Whereas patterns of traditional haemodynamic metrics around intercostal ostia did not vary notably between ostia, a range of different near-branch transWSS patterns was found. This is encouraging, since lesion distributions also vary from ostium to ostium within the same subject and with age. In the study presented here no age-related difference in transWSS patterns was observed. This finding may however change when considering more realistic intercostal flow splits, which may well be age-dependent. In the descending aorta the transWSS maps were dominated by a pair of streaks, which were not present on the TAWSS, OSI and RRT maps. Interestingly, the double streaks show a resemblance to patterns seen in maps of albumin uptake in this region (unpublished data, L. A. Clarke, 2012).

Although the transWSS was introduced here as a tool to further our understanding of multi-directional flow environments, the parameter also has a physiological interpretation, which may be relevant to the initiation of atherosclerotic disease.

In vitro studies have shown that endothelial cells and their nuclei align with the predominant flow direction and elongate with increasing shear stress (Levesque and Nerem, 1985; Potter et al., 2011). For example, in an orbital shaker model endothelial cells are randomly oriented at the centre of the well, but elongated in the periphery. Although the time-averaged WSS is approximately constant across the well, CFD analysis has shown that the radial and tangential shear components are balanced in the centre, but not in the periphery where there is more unidirectional flow (Potter et al., 2011). The relationship between cell/nucleus shape and WSS also appears to hold *in vivo* (Flaherty et al., 1972; Bond et al., 2011). These observations, in combination with the popular low shear theory, have led to the concept that endothelial cells in atherosclerosis-prone areas are more rounded or

polygonal-shaped than elsewhere. It is argued here that the length-to-width ratio of endothelial cells and their nuclei may also depend on the local transWSS: if a preferred flow direction exists, and the endothelial cell/nucleus aligns with this direction, the transWSS expresses how much the cell/nucleus is tugged sideways. In this sense, the interpretation of the transWSS is related to theories involving spatial WSS gradients (Lei et al., 1995; Barakat et al., 1997a; Buchanan et al., 1999).

However, before transWSS patterns can be compared rigorously to lesion maps, more physiologically realistic pulsatile flow conditions should be considered (keeping the averaged velocity at the aortic root rather than the inlet Reynolds number constant across animals, cfr. section 4.4). Additionally, the influence of the modelling assumptions, such as the flow rates imposed at the intercostal branches, on the distribution of the transWSS should be investigated in greater detail. The latter can be done in idealised geometries using an approach analogous to Kazakidi et al. (2009), who studied the influence of Re and flow division under steady flow conditions.

6.5 Conclusion

Metrics of *disturbed* flow traditionally used in haemodynamic studies cannot distinguish pulsatile and oscillatory unidirectional flows from multi-directional flow. The transverse WSS (transWSS), a metric that has this potential which was introduced here, showed patterns different from those seen with traditional haemodynamic metrics. Since near-branch patterns of transWSS vary between intercostal ostia even within the same subject, as is the case for lesion distributions, and transWSS patterns are dependent on the flow conditions in the side-branch (which could change with age), the metric may lead to improved understanding of atherogenesis and its relation with age.

Chapter 7

Conclusions

The research presented in the previous chapters supports the following thesis:

> A causal role for disturbed flow in early atherosclerosis is widely accepted in the bioengineering community. However, the evidence in literature for the consensus low and/or oscillatory shear theory of atherogenesis is less clear-cut than often assumed, at least partly owing to differences in study design and data processing techniques. The age-dependent localisation of lipid-rich lesions in aortas of cholesterol-fed rabbits is not in agreement with a linear low shear theory of atherogenesis, but does correlate with distributions of wall shear in the proximal descending thoracic segment. The analysis of different aspects, including the multi-directional character, of disturbed flow may help elucidate the relation between blood flow and early atherosclerosis.

In addition, the work presented here offers tools and guidelines for use in future studies.

Key findings are summarised in sections 7.1, and additional insights and tools are highlighted in section 7.2. Section 7.3 concludes with suggestions for future research directions.

7.1 Summary of key findings

Corresponding to the five research aims stated in section 1.3, five key findings are highlighted here.

Firstly, although a low and/or oscillatory shear theory is becoming largely accepted in the bioengineering community, a systematic literature review performed as part of the work presented here underscores that there is still no unequivocal answer on what aspect of the flow, if any, initiates atherosclerotic disease. This confirms the complexity of the problem, but is also in part due to substantial differences between studies in terms of study design (e.g. choice of species and disease assessment strategy) and data processing techniques (e.g. averaging or selective analysis). The outcome of the review emphasises the need for detailed longitudinal studies from the healthy state or average flow metrics derived from large numbers of healthy vessels.

Secondly, geometric analysis of a set of immature and mature rabbit aortas, reconstructed by micro-CT of vascular corrosion casts, revealed an age-related increase in the degree of aortic taper, particularly in the aortic arch region. No significant changes with age were observed in the curvature and torsion of the aortic centrelines.

Furthermore, computational simulations of steady-state and pulsatile blood flow dynamics in the reconstructed geometries showed age-related differences in the extent of Dean-type vortical structures into the descending aorta and the strength of a streak of high shear on the dorsal side of the aorta. The changes with age in blood flow characteristics were related to the observed geometric changes.

A qualitative and quantitative comparative analysis of wall shear stress and lesion prevalence distributions in aortas of immature and mature rabbits did not unequivocally support the low shear theory of atherogenesis and thereby added to the complexity of the relation between blood flow and early atherosclerosis. In the proximal descending aorta lesions even occurred more frequently in regions of high WSS. Age-related changes around branch ostia were not explained by the flow patterns.

Finally, recognising the importance of the multi-directionality of disturbed flow, a novel haemodynamic metric was defined which can distinguish between uni- and multi-directional flows. Application in idealised and anatomically realistic geometries showed that this metric, in combination with current metrics, gives a better characterisation of arterial flow and may lead to improved understanding of atherogenesis.

7.2 Additional insights and tools

On top of answering a number of research questions, as described in section 7.1, the work presented here has led to the development of tools and guidelines that can be applied in future studies. Four achievements are highlighted here.

In the first place, a dataset of vascular corrosion casts of immature and mature rabbits, including high-resolution reconstructions of the thoracic aortic segment, has been constructed. The reconstructed aortas best represent the geometries in the diastolic phase.

Further insight has been obtained into the non-linear shrinkage behaviour of Batson's #17 resin. The analysis suggests that supra-physiological infusion pressures should be used to compensate for shrinkage-induced changes in diameters, curvature and branching angles. The pressure should ideally be determined based on a pilot experiment for the animal model and vascular section of interest.

Many studies investigating the relation between blood flow and atherosclerosis lack a rigorous method of comparison between distributions of flow- and disease-related metrics. A statistical method has been developed here to assess the correlation between image pairs. The method does not require any assumptions (such as linearity) on the nature of the relationship and overcomes effects of the frequently-overlooked dependency between data points.

Finally, a novel haemodynamic metric has been introduced to allow a better characterisation of multi-directional disturbed flow.

7.3 Recommendations for future directions

The following studies could further our understanding of the rabbit aortic model of atherosclerosis, multi-directional disturbed flow and the relation between blood flow and atherosclerosis in general.

7.3.1 The rabbit aortic model of atherosclerosis

The rabbit aortas used in the geometric and haemodynamic analyses set out in this report were reconstructed by micro-CT of vascular corrosion casts. An investigation of the shrinkage properties of the resin used for vascular casting demonstrated the limitations of this technique. Although none of the methods currently available for the acquisition of 3D vascular geometries is perfect, the reconstruction of a similar dataset using a different technique, e.g. *in vivo* MRI scanning, could provide useful insights. In addition, such a study could be combined with the *in vivo* measurement of flow rates and waveforms in the aortic arch branches to investigate potential age-related differences. Flow rates and waveforms to the intercostal arteries are also unknown, but obtaining the required resolution with state-of-the-art technology is likely to be the limiting factor here.

Aortic wall motion was not considered in the work presented here, because a separate study of the effects of wall compliance on haemodynamics in a mature rabbit aorta did not reveal any significant changes in patterns of time-averaged flow-dependent metrics (unpublished data A. M. Plata, 2011). However, particularly in the ascending aorta, that study may have underestimated the amount of wall movement as a result of the choice of computational strategy, which was formulated in a fixed grid (Figueroa et al., 2006). A deformable wall strategy may therefore be required. The amount of *in vivo* wall movement, and potential age-related differences, could once more be investigated using MRI. In addition, the effect of arterial compliance on the multi-directional character of rabbit aortic flow has not been investigated.

Since the endothelium is more permeable to water than to LDL, an LDL-rich

layer forms adjacent to the endothelial surface. Local variations in the LDL concentration of this layer are considered to play a role in atherosclerotic plaque formation (Vincent et al., 2009). It would therefore be interesting to model this effect in the rabbit aorta and compare LDL concentration patterns to those of shear-related metrics and lesion prevalence.

Finally, only a limited segment of the rabbit aorta was investigated here. Since lesion prevalence and albumin uptake maps are also available further downstream (Cremers et al. (2011); unpublished data, L. A. Clarke, 2012), simulations of blood flow in entire rabbit aortas could directly be used in a more extensive comparative analysis. In particular, it would be interesting to investigate the distribution of transWSS in other segments of the rabbit aorta.

7.3.2 Multi-directional disturbed flow

The effect of Re and flow division on patterns of transWSS and other time-averaged haemodynamic metrics can be studied in an idealised branching geometry, similar to the analysis of Kazakidi et al. (2009) who investigated the effect of both parameters on steady WSS. Using this knowledge the distributions of the haemodynamic metrics in the rabbit aortas can be re-analysed. In addition, more physiologically realistic pulsatile flow conditions should be considered in the rabbit aortas.

On the experimental side, *in vitro* studies investigating the effects of disturbed flow on endothelial cell behaviour have often been limited to unidirectional flow environments, an exception being the orbital shaker model (Potter et al., 2012). Cell culture devices that can operate regimes of controlled multi-directional flow could provide useful insights on the behaviour of endothelial cells in truly disturbed flow. Cuffs similar to the one introduced by Cheng et al. (2005) could be used to generate more idealised flow conditions *in vivo*.

7.3.3 The relation between blood flow and atherosclerosis

In a more general scope, detailed longitudinal studies in animal models as well as in humans will be crucial for the investigation of the relation between blood flow and atherosclerosis. These should combine qualitative techniques with proper quantitative tools to compare disease distributions with maps of flow-related metrics, as illustrated in the work presented here.

References

S. A. Ahmed and D. P. Giddens. Pulsatile poststenotic flow studies with laser Doppler anemometry. *J Biomech*, 17(9):695–705, 1984.

J. Alastruey, S. R. Nagel, B. A. Nier, A. A. Hunt, P. D. Weinberg, and J. Peiro. Modelling pulse wave propagation in the rabbit systemic circulation to assess the effects of altered nitric oxide synthesis. *J Biomech*, 42:2116–2123, 2009.

J. Alastruey, J. H. Siggers, V. Peiffer, D. J. Doorly, and S. J. Sherwin. Reducing the data: Analysis of the role of vascular geometry on blood flow patterns in curved vessels. *Phys of Fluids*, 24:031902, 2012.

N.N. Anitschkow. *Arteriosclerosis: A Survey of the Problem (Ed. E.V. Cowdry)*, chapter Experimental atherosclerosis in animals, pages 271–322. Macmillan, New York, 1933.

L. Antiga. The Vascular Modeling Toolkit. http://www.vmtk.org, 2010.

L. Antiga and D. A. Steinman. Robust and objective decomposition and mapping of bifurcating vessels. *IEEE Trans Med Imaging*, 23:704–713, 2004.

L. Antiga, B. Ene-Iordache, and A. Remuzzi. Computational geometry for patient-specific reconstruction and meshing of blood vessels from MR and CT angiography. *IEEE Trans Med Imaging*, 22(5):674–684, 2003.

T. Asakura and T. Karino. Flow patterns and spatial distribution of atherosclerotic lesions in human coronary arteries. *Circ. Res.*, 66:1045–1066, 1990.

A. D. Augst, B. Ariff, S. A. McG Thom, X. Y. Xu, and A. D. Hughes. Analysis of complex flow and the relationship between blood pressure, wall shear stress, and intima-media thickness in the human carotid artery. *Am. J. Physiol. Heart Circ. Physiol.*, 293(2):H1031–1037, 2007.

A. P. Avolio, M. F O'Rourke, K. Mang, P. T. Bason, and B. S. Gow. A comparative study of pulsatile arterial hemodynamics in rabbit and guinea pigs. *Am. J. Physiol.*, 230(4):868–875, 1976.

F. M. Baldwin. Notes on the branches of the aorta (arcus aortae) and the subclavian artery of the rabbit. *Anatomical Rec*, 19:173–183, 1920.

A. I. Barakat, T. Karino, and C. K. Colton. Microcinematographic studies of flow patterns in the excised rabbit aorta and its major branches. *Biorheology*, 34(3):195–221, 1997a.

A. I. Barakat, R. P. Marini, and C. K. Colton. Measurement of flow rates through aortic branches in the anesthetized rabbit. *Lab. Anim. Sci.*, 47:184–189, 1997b.

S. E. Barnes and P. D. Weinberg. Contrasting patterns of spontaneous aortic disease in young and old rabbits. *Arterioscler. Thromb. Vasc. Biol.*, 18:300–308, 1998.

S. E. Barnes and P. D. Weinberg. Two patterns of lipid deposition in the cholesterol-fed rabbit. *Arterioscler. Thromb. Vasc. Biol.*, 19:2376–2386, 1999.

S. E. Barnes and P. D. Weinberg. Strain-dependent differences in the pattern of aortic lipid deposition in cholesterol-fed rabbits. *Exp. Mol. Pathol.*, 71: 161–170, 2001.

M. Berger, C. Jean-Faucher, M. de Turckheim, G. Veyssiere, M. R. Blanc, J. C. Poirier, and C. Jean. Testosterone, luteinizing hormone (LH) and follicle stimulating hormone (FSH) in plasma of rabbit from birth to adulthood. Correlation with sexual and behavioural development. *Acta Endocrinol.*, 99 (3):459–465, 1982.

M. Bijl. Endothelial activation, endothelial dysfunction and premature atherosclerosis in systemic autoimmune diseases. *Neth J Med*, 61:273–277, 2003.

P. L. Blackshear, G. L. Blackshear, M. K. Newell, S. J. Kayser, and P. F. Emerson. The localization of transient subendothelial water-filled blisters in the in situ rabbit aorta as a result of reduction in pressure. In G. Schettler, R. M. Nerem, H. Schmid-Schonbein, H. Morl, and C. Diehm, editors, *Fluid dynamics as a localizing factor for atherosclerosis*, pages 116–128. Springer-Verlag, 1982.

A. R. Bond, S. Iftikhar, A. A. Bharath, and P. D. Weinberg. Morphological evidence for a change in the pattern of aortic wall shear stress with age. *Arterioscler. Thromb. Vasc. Biol.*, 31:543–550, 2011.

N. Bray. Notes on mesh smoothing. http://mgarland.org/class/geom04/ material/smoothing.pdf, 2004.

M. Brett, W. D. Penny, and S. Kiebel. An introduction to random field theory. In *Human Brain Function II*. Academic Press, London, 2003.

J. R. Buchanan, C. Kleinstreuer, G. A. Truskey, and M. Lei. Relation between non-uniform hemodynamics and sites of altered permeability and lesion growth at the rabbit aorto-celiac junction. *Atherosclerosis*, 143(1):27–40, 1999.

J. R. Buchanan, C. Kleinstreuer, S. Hyun, and G. A. Truskey. Hemodynamics simulation and identification of susceptible sites of atherosclerotic lesion formation in a model abdominal aorta. *J Biomech*, 36(8):1185–1196, 2003.

Q. T. Bui, M. Prempeh, and R. L. Wilensky. Atherosclerotic plaque development. *Int. J. Biochem. Cell Biol.*, 41:2109–2113, 2009.

C. G. Caro, J. M. Fitz-Gerald, and R. C. Schroter. Arterial wall shear and distribution of early atheroma in man. *Nature*, 223:1159–1160, 1969.

C. G. Caro, J. M. Fitz-Gerald, and R. C. Schroter. Atheroma and arterial wall shear. Observation, correlation and proposal of a shear dependent mass transfer mechanism for atherogenesis. *Proc. R. Soc. Lond., B, Biol. Sci.*, 177: 109–159, 1971.

C. Casteleyn, B. Trachet, D. Van Loo, D. G. Devos, W. Van den Broeck, P. Simoens, and P. Cornillie. Validation of the murine aortic arch as a model to study human vascular diseases. *J. Anat.*, 216:563–571, 2010.

E. Cecchi, C. Giglioli, S. Valente, C. Lazzeri, G. F. Gensini, R. Abbate, and L. Mannini. Role of hemodynamic shear stress in cardiovascular disease. *Atherosclerosis*, 214:249–256, 2011.

A. Chakraborty, S. Chakraborty, V. R. Jala, B. Haribabu, M. K. Sharp, and R. E. Berson. Effects of biaxial oscillatory shear stress on endothelial cell proliferation and morphology. *Biotechnol. Bioeng.*, 109(3):695–707, 2012.

Y. S. Chatzizisis, M. Jonas, A. U. Coskun, R. Beigel, B. V. Stone, C. Maynard, R. G. Gerrity, W. Daley, C. Rogers, E. R. Edelman, C. L. Feldman, and P. H. Stone. Prediction of the localization of high-risk coronary atherosclerotic plaques on the basis of low endothelial shear stress: an intravascular ultrasound and histopathology natural history study. *Circulation*, 117:993–1002, 2008.

Y. S. Chatzizisis, A. B. Baker, G. K. Sukhova, K. C. Koskinas, M. I. Papafaklis, R. Beigel, M. Jonas, A. U. Coskun, B. V. Stone, C. Maynard, G. P. Shi, P. Libby, C. L. Feldman, E. R. Edelman, and P. H. Stone. Augmented expression and activity of extracellular matrix-degrading enzymes in regions of low endothelial shear stress colocalize with coronary atheromata with thin fibrous caps in pigs. *Circulation*, 123:621–630, 2011.

A. Y. Cheer, H. A. Dwyer, A. I. Barakat, E. Sy, and M. Bice. Computational study of the effect of geometric and flow parameters on the steady flow field at the rabbit aorto-celiac bifurcation. *Biorheology*, 35:415–435, 1998.

C. Cheng, R. van Haperen, M. de Waard, L. C. van Damme, D. Tempel, L. Hanemaaijer, G. W. van Cappellen, J. Bos, C. J. Slager, D. J. Duncker, A. F. van der Steen, R. de Crom, and R. Krams. Shear stress affects the intracellular distribution of eNOS: direct demonstration by a novel in vivo technique. *Blood*, 106:3691–3698, 2005.

C. Cheng, D. Tempel, R. van Haperen, A. van der Baan, F. Grosveld, M. J. Daemen, R. Krams, and R. de Crom. Atherosclerotic lesion size and vulnerability are determined by patterns of fluid shear stress. *Circulation*, 113: 2744–2753, 2006.

S. Chien. Effects of disturbed flow on endothelial cells. *Ann Biomed Eng*, 36 (4):554–562, 2008.

D. E. Conway, M. R. Williams, S. G. Eskin, and L. V. McIntire. Endothelial cell responses to atheroprone flow are driven by two separate flow components: low time-average shear stress and fluid flow reversal. *Am. J. Physiol. Heart Circ. Physiol.*, 298:H367–374, 2010.

G. Coppola and C. Caro. Oxygen mass transfer in a model three-dimensional artery. *J R Soc Interface*, 5(26):1067–1075, Sep 2008.

J. F. Cornhill and M. R. Roach. A quantitative study of the localization of atherosclerotic lesions in the rabbit aorta. *Atherosclerosis*, 23(3):489–501, 1976.

J. F. Cornhill, W. A. Barrett, E. E. Herderick, R. W. Mahley, and D. L. Fry. Topographic study of sudanophilic lesions in cholesterol-fed minipigs by image analysis. *Arteriosclerosis*, 5(5):415–426, 1985.

J. F. Cornhill, E. E. Herderick, and H. C. Stary. Topography of human aortic sudanophilic lesions. *Monogr Atheroscler.*, 15:13–19, 1990.

R. H. Cox. Comparison of carotid artery mechanics in the rat, rabbit, and dog. *Am. J. Physiol.*, 234(3):H280–288, Mar 1978.

S. G. Cremers, S. J. Wolffram, and P. D. Weinberg. Atheroprotective effects of dietary l-arginine increase with age in cholesterol-fed rabbits. *Br. J. Nutrition*, 105(10):1439–1447, 2011.

G. De Santis, P. Mortier, M. De Beule, P. Segers, P. Verdonck, and B. Verhegghe. Patient-specific computational fluid dynamics: structured mesh generation from coronary angiography. *Med Biol Eng Comput*, 48(4):371–380, 2010.

D. De Syo. Radiogrametric analysis of carotid bifurcation: hemodynamic-atherogenetic repercussions on surgical patients. In D. Liepsch, editor, *Biofluid Mechanics. Blood flow in large vessels. Proceedings of the 2nd International Symposium, Biofluid Mechanics and Biorheology*. Springer-Verlag Berlin, Heidelberg, 1990.

D. De Syo, B. D. Franjic, I. Lovricevic, M. Vukelic, and H. Palenkic. Carotid bifurcation position and branching angle in patients with atherosclerotic carotid disease. *Coll Antropol*, 29(2):627–632, 2005.

W. R. Dean. Note on the motion of fluid in a curved pipe. *Philosophical Magazine*, 20:208–223, 1927.

W. R. Dean. The stream-line motion of fluid in a curved pipe. *Philos Mag S*, 5(30):673–695, 1928.

D. J. Doorly and S. J. Sherwin. Geometry and flow. In L. Formaggia, A. Quarteroni, and A. Veneziani, editors, *Cardiovascular Mathematics*. Springer, 2009.

B. A. Ewins, J. Majewicz, T. J. Staughton, and P. D. Weinberg. Two-dimensional maps of short-term albumin uptake by the immature and mature rabbit aortic wall around branch points. *J Biomech Eng*, 124:684–690, 2002.

C. L. Feldman, A. U. Coskun, Y. Yeghiazarians, S. Kinlay, A. Wahle, M. E. Olszewski, J. D. Rossen, M. Sonka, J. J. Popma, J. Orav, R. E. Kuntz, and

P. H. Stone. Remodeling characteristics of minimally diseased coronary arteries are consistent along the length of the artery. *Am. J. Cardiol.*, 97(1):13–16, Jan 2006.

J. H. Ferziger and M. Peric. *Computational Methods for Fluid Dynamics*. Springer, 3rd edition, 2002.

C. A. Figueroa, I. E. Vignon-Clementel, K. E. Jansen, T. J. Hughes, and C. A. Taylor. A coupled momentum method for modeling blood flow in three-dimensional deformable arteries. *Comput Methods Appl Mech Engrg*, 195: 5685–5706, 2006.

J. T. Flaherty, J. E. Pierce, V. J. Ferrans, D. J. Patel, W. K. Tucker, and D. L. Fry. Endothelial nuclear patterns in the canine arterial tree with particular reference to hemodynamic events. *Circ. Res.*, 30:23–33, 1972.

B. A. Forster and P. D. Weinberg. Changes with age in the influence of endogenous nitric oxide on transport properties of the rabbit aortic wall near branches. *Arterioscler. Thromb. Vasc. Biol.*, 17:1361–1368, 1997.

B. A. Forster, Q. Javed, D. S. Leake, and P. D. Weinberg. High-resolution mapping of the frequency of lipid deposits in thoracic aortae from cholesterol-fed and heritable hyperlipidaemic rabbits. *Atherosclerosis*, 120:249–253, 1996.

F. Frenet. Sur les courbes à double courbure. *J. de Math.*, 17, 1852.

M. H. Friedman, V. O'Brien, and L. W. Ehrlich. Calculations of pulsatile flow through a branch: implications for the hemodynamics of atherogenesis. *Circ. Res.*, 36(2):277–285, 1975.

M. H. Friedman, G. M. Hutchins, C. B. Bargeron, O. J. Deters, and F. F. Mark. Correlation between intimal thickness and fluid shear in human arteries. *Atherosclerosis*, 39(3):425–436, Jun 1981.

D. L. Fry. Acute vascular endothelial changes associated with increased blood velocity gradients. *Circ. Res.*, 22(2):165–197, 1968.

D. L. Fry. Certain histological and chemical responses of the vascular interface to acutely induced mechanical stress in the aorta of the dog. *Circ. Res.*, 24 (1):93–108, 1969.

D. Gallo, D. A. Steinman, P. B. Bijari, and U. Morbiducci. Helical flow in carotid bifurcation as a surrogate marker of exposure to disturbed shear. *J Biomech*, 45(14):2398–2404, 2012.

M. Germano. On the effect of torsion on a helical pipe flow. *J Fluid Mech*, 152:1–8, 1982.

G. S. Getz and C. A. Reardon. Animal models of atherosclerosis. *Arterioscler. Thromb. Vasc. Biol.*, 32(5):1104–1115, 2012.

F. J. Gijsen, J. J. Wentzel, A. Thury, B. Lamers, J. C. Schuurbiers, P. W. Serruys, and A. F. van der Steen. A new imaging technique to study 3-D plaque and shear stress distribution in human coronary artery bifurcations in vivo. *J Biomech*, 40:2349–2357, 2007.

S. Giordana. *Geometrical reconstruction from medical images, classification and modelling of arterial by-pass grafts.* PhD thesis, Imperial College London, 2004.

L. Goubergrits, K. Affeld, J. Fernandez-Britto, and L. Falcon. Atherosclerosis and flow in carotid arteries with authentic geometries. *Biorheology*, 39:519–524, 2002.

L. Grinberg, D. Pekurovsky, S. J. Sherwin, and G. E. Karniadakis. Parallel performance of the coarse space linear vertex solver and low energy basis preconditioner for spectral/hp elements. *Parallel Computing*, 35:284–304, 2009.

J. R. Halliwill and C. T. Minson. Retrograde shear: backwards into the future? *Am. J. Physiol. Heart Circ. Physiol.*, 298:H1126–1127, 2010.

G. Hamel. Spiralfömrige bewegungen zäher flüssigheiten. *Jahresbericht der Deutschen Mathematiker-Vereinigung*, 25:34–60, 1916.

G. K. Hansson, A. K. Robertson, and C. Soderberg-Naucler. Inflammation and atherosclerosis. *Annu Rev Pathol*, 1:297–329, 2006.

J. G. Hanstede and P. O. Gerrits. A new plastic for morphometric investigation of blood vessels, especially in large organs such as the human liver. *Anat. Rec.*, 203(2):307–315, 1982.

X. He and D. N. Ku. Pulsatile flow in the human left coronary artery bifurcation: average conditions. *J Biomech Eng*, 118:74–82, 1996.

G. Helmlinger, R. V. Geiger, S. Schreck, and R. M. Nerem. Effects of pulsatile flow on cultured vascular endothelial cell morphology. *J Biomech Eng*, 113 (2):123–131, 1991.

R. A. Herrmann, R. A. Malinauskas, and G. A. Truskey. Characterization of sites with elevated LDL permeability at intercostal, celiac, and iliac branches of the normal rabbit aorta. *Arterioscler. Thromb.*, 14(2):313–323, 1994.

H. A. Himburg and M. H. Friedman. Correspondence of low mean shear and high harmonic content in the porcine iliac arteries. *J Biomech Eng*, 128(6): 852–856, 2006.

H. A. Himburg, D. M. Grzybowski, A. L. Hazel, J. A. LaMack, X. M. Li, and M. H. Friedman. Spatial comparison between wall shear stress measures and porcine arterial endothelial permeability. *Am. J. Physiol. Heart Circ. Physiol.*, 286:H1916–1922, 2004.

Y. Hoi, Y. Q. Zhou, X. Zhang, R. M. Henkelman, and D. A. Steinman. Correlation between local hemodynamics and lesion distribution in a novel aortic regurgitation murine model of atherosclerosis. *Ann Biomed Eng*, 39:1414–1422, 2011.

C. Irace, C. Carallo, M. S. De Franceschi, F. Scicchitano, M. Milano, C. Tripolino, F. Scavelli, and A. Gnasso. Human common carotid wall shear stress as a function of age and gender: a 12-year follow-up study. *Age (Dordr)*, 2011.

G. B. Jeffery. The two-dimensional steady motion of a viscous fluid. *Philos Mag*, 29:455–465, 1915.

J. Jeong and F. Hussain. On the identification of a vortex. *J Fluid Mech*, 285: 69–94, 1995.

B. M. Johnston, P. R. Johnston, S. Corney, and D. Kilpatrick. Non-Newtonian blood flow in human right coronary arteries: steady state simulations. *J Biomech*, 37:709–720, 2004.

B. M. Johnston, P. R. Johnston, S. Corney, and D. Kilpatrick. Non-Newtonian blood flow in human right coronary arteries: transient simulations. *J Biomech*, 39:1116–1128, 2006.

C. J. Jones, M. J. Lever, Y. Ogasawara, K. H. Parker, K. Tsujioka, O. Hiramatsu, K. Mito, C. G. Caro, and F. Kajiya. Blood velocity distributions within intact canine arterial bifurcations. *Am. J. Physiol.*, 262(5 Pt 2):H1592–1599, 1992.

A. K. Joshi, R. L. Leask, J. G. Myers, M. Ojha, J. Butany, and C. R. Ethier. Intimal thickness is not associated with wall shear stress patterns in the human right coronary artery. *Arterioscler. Thromb. Vasc. Biol.*, 24:2408–2413, 2004.

G. E. Karniadakis and S. J. Sherwin. *Spectral/hp Element Methods for Computational Fluid Dynamics*. Oxford Science Publications, 2 edition, 2005.

A. Kazakidi, S. J. Sherwin, and P. D. Weinberg. Effect of Reynolds number and flow division on patterns of haemodynamic wall shear stress near branch points in the descending thoracic aorta. *J R Soc Interface*, 6:539–548, 2009.

A. Kazakidi, A. M. Plata, S. J. Sherwin, and P. D. Weinberg. Effect of reverse flow on the pattern of wall shear stress near arterial branches. *J R Soc Interface*, 8(64):1594–1603, 2011.

T. Kenner, H. Leopold, and H. Hinghofer-Szalkay. The continuous high-precision measurement of the density of flowing blood. *Pflugers Arch.*, 370 (1):25–29, 1977.

J. Knight, U. Olgac, S. C. Saur, D. Poulikakos, W. Marshall, P. C. Cattin, H. Alkadhi, and V. Kurtcuoglu. Choosing the optimal wall shear parameter for the prediction of plaque location-A patient-specific computational study in human right coronary arteries. *Atherosclerosis*, 211:445–450, 2010.

K. C. Koskinas, C. L. Feldman, Y. S. Chatzizisis, A. U. Coskun, M. Jonas, C. Maynard, A. B. Baker, M. I. Papafaklis, E. R. Edelman, and P. H. Stone. Natural history of experimental coronary atherosclerosis and vascular remodeling in relation to endothelial shear stress: a serial, in vivo intravascular ultrasound study. *Circulation*, 121:2092–2101, 2010.

T. Koyanagi, N. Kawaharada, Y. Kurimoto, T. Ito, T. Baba, M. Nakamura, A. Watanebe, and T. Higami. Examination of intercostal arteries with transthoracic doppler sonography. *Echocardiography*, pages 17–20, 2009.

R. Krams, J. J. Wentzel, J. A. Oomen, R. Vinke, J. C. Schuurbiers, P. J. de Feyter, P. W. Serruys, and C. J. Slager. Evaluation of endothelial shear stress and 3D geometry as factors determining the development of atherosclerosis and remodeling in human coronary arteries in vivo. Combining 3D reconstruction from angiography and IVUS (ANGUS) with computational fluid dynamics. *Arterioscler. Thromb. Vasc. Biol.*, 17(10):2061–2065, 1997.

R. G. Kratky and M. R. Roach. Shrinkage of Batson's and its relevance to vascular casting. *Atherosclerosis*, 51:339–341, 1984.

R. G. Kratky, C. M. Zeindler, D.K.C. Lo, and M. R. Roach. Quantitative measurement from vascular casts. *Scann Microscop*, 3(3):937–943, 1989.

D. N. Ku, D. P. Giddens, C. K. Zarins, and S. Glagov. Pulsatile flow and atherosclerosis in the human carotid bifurcation. Positive correlation between

plaque location and low oscillating shear stress. *Arteriosclerosis*, 5:293–302, 1985.

J. A. LaMack, H. A. Himburg, J. Zhang, and M. H. Friedman. Endothelial gene expression in regions of defined shear exposure in the porcine iliac arteries. *Ann Biomed Eng*, 38:2252–2262, 2010.

S. W. Lee, L. Antiga, and D. A. Steinman. Correlations among indicators of disturbed flow at the normal carotid bifurcation. *J Biomech Eng*, 131:061013, 2009.

M. Lei, C. Kleinstreuer, and G. A. Truskey. Numerical investigation and prediction of atherogenic sites in branching arteries. *J Biomech Eng*, 117: 350–357, 1995.

R. Leiser, C. Krebs, B. Ebert, and V. Dantzer. Placental vascular corrosion cast studies: a comparison between ruminants and humans. *Microsc. Res. Tech.*, 38(1-2):76–87, 1997.

M. J. Levesque and R. M. Nerem. The elongation and orientation of cultured endothelial cells in response to shear stress. *J Biomech Eng*, 107(4):341–347, 1985.

M. J. Levesque, J. F. Cornhill, and R. M. Nerem. Vascular casting. A new method for the study of the arterial endothelium. *Atherosclerosis*, 34:457–467, 1979.

W. E. Lorensen and H. E. Cline. Marching cubes: a high resolution 3d surface construction algorithm. *Computer Graphics*, 21(4):163–169, 1987.

Z. Lou and W. J. Yang. Biofluid dynamics at arterial bifurcations. *Crit Rev Biomed Eng*, 19(6):455–493, 1992.

V. M. Lukasik and R. J. Gillies. Animal anaesthesia for in vivo magnetic resonance. *NMR Biomed*, 16:459–467, 2003.

P. Ma, X. Li, and D. N. Ku. Convective mass transfer at the carotid bifurcation. *J Biomech*, 30:565–571, 1997.

N. Maeda, L. Johnson, S. Kim, J. Hagaman, M. Friedman, and R. Reddick. Anatomical differences and atherosclerosis in apolipoprotein E-deficient mice with 129/SvEv and C57BL/6 genetic backgrounds. *Atherosclerosis*, 195:75–82, 2007.

F. Maes, A. Collignon, D. Vandermeulen, G. Marchal, and P. Suetens. Multimodality image registration by maximization of mutual information. *IEEE Trans Med Imaging*, 16(2):187–198, 1997.

R. A. Malinauskas, R. A. Herrmann, and G. A. Truskey. The distribution of intimal white blood cells in the normal rabbit aorta. *Atherosclerosis*, 115(2): 147–163, 1995.

A. Mantha, C. Karmonik, G. Benndorf, C. Strother, and R. Metcalfe. Hemodynamics in a cerebral artery before and after the formation of an aneurysm. *AJNR Am J Neuroradiol*, 27(5):1113–1118, May 2006.

C. J. McGillicuddy, M. J. Carrier, and P. D. Weinberg. Distribution of lipid deposits around aortic branches of mice lacking LDL receptors and apolipoprotein E. *Arterioscler. Thromb. Vasc. Biol.*, 21:1220–1225, 2001.

D. E. McMillan. Blood flow and the localization of atherosclerotic plaques. *Stroke*, 16(4):582–587, 1985.

J. R. A. Mitchell and C. J. Schwartz. *Arterial Disease*, page 52. Blackwell, Oxford, 1965.

J. A. Moore, B. K. Rutt, S. J. Karlik, K. Yin, and C. R. Ethier. Computational blood flow modeling based on in vivo measurements. *Ann Biomed Eng*, 27: 627–640, 1999.

P. A. P. Moran. Notes on continuous stochastic phenomena. *Biometrika*, 37 (1):17–23, 1950.

C. D. Murray. The physiological principle of minimum work applied to the angle of branching of arteries. *J. Gen. Physiol.*, 9:835–841, 1926.

Y. Nakashima, A. S. Plump, E. W. Raines, J. L. Breslow, and R. Ross. ApoE-deficient mice develop lesions of all phases of atherosclerosis throughout the arterial tree. *Arterioscler. Thromb.*, 14(1):133–140, 1994.

T. E. Nichols and A. P. Holmes. Nonparametric permutation tests for functional neuroimaging: a primer with examples. *Hum Brain Mapp*, 15(1):1–25, Jan 2002.

U. Olgac, V. Kurtcuoglu, S. C. Saur, and D. Poulikakos. Identification of atherosclerotic lesion-prone sites through patient-specific simulation of low-density lipoprotein accumulation. *Med Image Comput Comput Assist Interv*, 11(Pt 2):774–781, 2008.

U. Olgac, D. Poulikakos, S. C. Saur, H. Alkadhi, and V. Kurtcuoglu. Patient-specific three-dimensional simulation of LDL accumulation in a human left coronary artery in its healthy and atherosclerotic states. *Am. J. Physiol. Heart Circ. Physiol.*, 296:H1969–1982, 2009.

U. Olgac, J. Knight, D. Poulikakos, S. C. Saur, H. Alkadhi, L. M. Desbiolles, P. C. Cattin, and V. Kurtcuoglu. Computed high concentrations of low-density lipoprotein correlate with plaque locations in human coronary arteries. *J Biomech*, 44:2466–2471, 2011.

T. L. Owen. Effect of age on blood pressure and small vessel reactivity in male rabbits. *Blood Vessels*, 23:271–278, 1986.

K. H. Parker and C. G. Caro. *Magnetic Resonance Angiography, Concepts and Applications*, chapter Flow in the macrocirculation: basic concepts from fluid mechanics. Mosby, St. Louis, 1993.

K. Perktold and M. Resch. Numerical flow studies in human carotid artery bifurcations: basic discussion of the geometric factor in atherogenesis. *J Biomed Eng*, 12(2):111–123, 1990.

K. Perktold, R. O. Peter, M. Resch, and G. Langs. Pulsatile non-Newtonian blood flow in three-dimensional carotid bifurcation models: a numerical study of flow phenomena under different bifurcation angles. *J Biomed Eng*, 13:507–515, 1991.

A. M. Plata. *A Computational Study of Blood Flow and Vascular Nitric Oxide A computational study of blood flow and vascular nitric oxide transport.* PhD thesis, Imperial College London, 2010.

A. M. Plata, S. J. Sherwin, J. Stiller, and J. Peiro. High-order mesh generation using spherigon patches. Submitted to J. Numeric. Methods Fluids.

C. Poelma, R. M. E. van der Mijle, J. M. Mari, M.-X. Tang, P. D. Weinberg, and J. Westerweel. Ultrasound imaging velocimetry: towards reliable wall shear stress measurements. *Eur J Mech-B/Fluids*, 2012.

C. M. Potter, M. H. Lundberg, L. S. Harrington, C. M. Warboys, T. D. Warner, R. E. Berson, A. V. Moshkov, J. Gorelik, P. D. Weinberg, and J. A. Mitchell. Role of shear stress in endothelial cell morphology and expression of cyclooxygenase isoforms. *Arterioscler. Thromb. Vasc. Biol.*, 31(2):384–391, 2011.

C. M. Potter, S. Schobesberger, M. H. Lundberg, P. D. Weinberg, J. A. Mitchell, and J. Gorelik. Shape and compliance of endothelial cells after shear stress in vitro or from different aortic regions: scanning ion conductance microscopy study. *PLoS ONE*, 7(2):e31228, 2012.

R. Putz and R. Pabst, editors. *Atlas van de menselijke anatomi*, volume 2nd, page 114. Bohn Stafleu van Loghum, 3rd edition, 2006.

W. S. Rasband, 1997-2011. URL `http://rsbweb.nih.gov/ij/`.

A. Redaelli, F. Maisano, G. Ligorio, E. Cattaneo, F. M. Montevecchi, and O. Alfieri. Flow dynamics of the St Jude Medical Symmetry aortic connector vein graft anastomosis do not contribute to the risk of acute thrombosis. *J. Thorac. Cardiovasc. Surg.*, 128(1):117–123, 2004.

R. S. Reneman and A. P. Hoeks. Wall shear stress as measured in vivo: consequences for the design of the arterial system. *Med Biol Eng Comput*, 46 (5):499–507, 2008.

J. P. Richards and P. D. Weinberg. Distribution of disease around the aorto-coeliac branch of white carneau pigeons at different ages. *Exp. Mol. Pathol.*, 68:95–103, 2000.

F. Rikhtegar, J. A. Knight, U. Olgac, S. C. Saur, D. Poulikakos, W. Marshall, P. C. Cattin, H. Alkadhi, and V. Kurtcuoglu. Choosing the optimal wall shear parameter for the prediction of plaque location-A patient-specific computational study in human left coronary arteries. *Atherosclerosis*, 221(2):432–437, 2012.

M. R. Roach and J. Fletcher. Effect of unilateral nephrectomy of the localization of aortic sudanophilic lesions in cholesterol-fed rabbits. *Atherosclerosis*, 24(1-2):327–333, 1976.

H. Samady, P. Eshtehardi, M. C. McDaniel, J. Suo, S. S. Dhawan, C. Maynard, L. H. Timmins, A. A. Quyyumi, and D. P. Giddens. Coronary artery wall shear stress is associated with progression and transformation of atherosclerotic plaque and arterial remodeling in patients with coronary artery disease. *Circulation*, 124:779–788, 2011.

A. P. Sawchuk, J. L. Unthank, and M. C. Dalsing. Drag reducing polymers may decrease atherosclerosis by increasing shear in areas normally exposed to low shear stress. *J. Vasc. Surg.*, 30(4):761–764, 1999.

A. Sebkhi and P. D. Weinberg. Age-related variations in transport properties of the rabbit arterial wall near branches. *Atherosclerosis*, 106:1–8, 1994.

A. Sebkhi and P. D. Weinberg. Effect of age on the pattern of short-term albumin uptake by the rabbit aortic wall near intercostal branch ostia. *Arterioscler. Thromb. Vasc. Biol.*, 16:317–327, 1996.

J. A. Serret. "sur quelques formules relatives à la théorie des courbes à double courbure. *J. de Math.*, 16, 1851.

P. K. Shah. Inflammation and plaque vulnerability. *Cardiovasc Drugs Ther*, 23:31–40, 2009.

N. Shahcheraghi, H. A. Dwyer, A. Y. Cheer, A. I. Barakat, and T. Rutaganira. Unsteady and three-dimensional simulation of blood flow in the human aortic arch. *J Biomech Eng*, 124(4):378–387, 2002.

S. J. Sherwin. A substepping navier-stokes splitting scheme for spectral/hp element discretisations. In *International parallel computational fluid dynamics conference*, pages 43–52. Elsevier Science, 2003.

S. J. Sherwin and H. M. Blackburn. Three-dimensional instabilities and transition of steady and pulsatile axisymmetric stenotic flows. *J Fluid Mech*, 533: 297–327, 2005.

A. C. Simon and J. Levenson. Abnormal wall shear conditions in the brachial artery of hypertensive patients. *J. Hypertens.*, 8(2):109–114, 1990.

H. Sinzinger, K. Silberbauer, and W. Auerswald. Quantitative investigation of sudanophilic lesions around the aortic ostia of human fetuses, newborn and children. *Blood Vessels*, 17:44–52, 1980.

P. Siogkas, A. Sakellarios, T. Exarchos, L. Athanasiou, E. Karvounis, K. Stefanou, E. Fotiou, D. Fotiadis, K. Naka, L. Michalis, N. Filipovic, and O. Parodi. Multi-scale patient-specific artery and atherogenesis models. *IEEE Trans Biomed Eng*, 2011.

G. D. Sloop, R. S. Perret, J. S. Brahney, and M. Oalmann. A description of two morphologic patterns of aortic fatty streaks, and a hypothesis of their pathogenesis. *Atherosclerosis*, 141:153–160, 1998.

A. F. Stalder, M. F. Russe, A. Frydrychowicz, J. Bock, J. Hennig, and M. Markl. Quantitative 2D and 3D phase contrast MRI: optimized analysis

of blood flow and vessel wall parameters. *Magn Reson Med*, 60(5):1218–1231, 2008.

H. C. Stary. Composition and classification of human atherosclerotic lesions. *Virchows Arch A Pathol Anat Histopathol*, 421:277–290, 1992.

T. J. Staughton and P. D. Weinberg. Effect of time of day and rabbit strain on patterns of aortic wall permeability. *Exp. Physiol.*, 89:109–118, 2004.

D. A. Steinman. Image-based computational fluid dynamics: a new paradigm for monitoring hemodynamics and atherosclerosis. *Curr Drug Targets Cardiovasc Haematol Disord*, 4:183–197, 2004.

D. A. Steinman. Assumptions in modelling of large artery hemodynamics. In D. Ambrosi, A. Quarteroni, and G. Rozza, editors, *Modeling of physiological flows*, volume 5, chapter 1. Springer, 1 edition, 2011.

D. A. Steinman, J. B. Thomas, H. M. Ladak, J. S. Milner, B. K. Rutt, and J. D. Spence. Reconstruction of carotid bifurcation hemodynamics and wall thickness using computational fluid dynamics and MRI. *Magn Reson Med*, 47: 149–159, 2002.

P. H. Stone, A. U. Coskun, S. Kinlay, J. J. Popma, M. Sonka, A. Wahle, Y. Yeghiazarians, C. Maynard, R. E. Kuntz, and C. L. Feldman. Regions of low endothelial shear stress are the sites where coronary plaque progresses and vascular remodelling occurs in humans: an in vivo serial study. *Eur. Heart J.*, 28:705–710, 2007.

J. Suo, J. Oshinski, and D. P. Giddens. Effects of wall motion and compliance on flow patterns in the ascending aorta. *J Biomech Eng*, 125:347–354, 2003.

J. Suo, J. N. Oshinski, and D. P. Giddens. Blood flow patterns in the proximal human coronary arteries: relationship to atherosclerotic plaque occurrence. *Mol Cell Biomech*, 5:9–18, 2008.

A. Svindland. The localization of sudanophilic and fibrous plaques in the main left coronary bifurcation. *Atherosclerosis*, 48(2):139–145, 1983.

A. Svindland and L. Walløe. Distribution pattern of sudanophilic plaques in the descending thoracic and proximal abdominal human aorta. *Atherosclerosis*, 57(2-3):219–224, 1985.

C. A. Taylor, T. J. Hughes, and C. K. Zarins. Finite element modeling of three-dimensional pulsatile flow in the abdominal aorta: relevance to atherosclerosis. *Ann Biomed Eng*, 26:975–987, 1998.

M. Texon. The hemodynamic basis of atherosclerosis. Further observations: the linear lesion. *Bull N Y Acad Med*, 62(9):875–880, 1986.

M. Texon, A. M. Imparato, and M. Helpern. The role of vascular dynamics in the development of atherosclerosis. *JAMA*, 194(11):1226–1230, Dec 1965.

J. Theiler, S. Eubank, A. Longtin, B. Galdrikian, and J. D. Farmer. Testing for nonlinearity in time series: the method of surrogate data. *Physica D: Nonlinear Phenomena*, 58(1-4):77–94, 1992.

M. J. Thubrikar, S. K. Roskelley, and R. T. Eppink. Study of stress concentration in the walls of the bovine coronary arterial branch. *J Biomech*, 23(1): 15–26, 1990.

B. Trachet, J. Bols, G. De Santis, S. Vandenberghe, B. Loeys, and P. Segers. The impact of simplified boundary conditions and aortic arch inclusion on CFD simulations in the mouse aorta: a comparison with mouse-specific reference data. *J Biomech Eng*, 133(12):121006, 2011.

A. G. van der Giessen, M. Schaap, F. J. Gijsen, H. C. Groen, T. van Walsum, N. R. Mollet, J. Dijkstra, F. N. van de Vosse, W. J. Niessen, P. J. de Feyter, A. F. van der Steen, and J. J. Wentzel. 3D fusion of intravascular ultrasound and coronary computed tomography for in-vivo wall shear stress analysis: a feasibility study. *Int J Cardiovasc Imaging*, 26:781–796, 2010.

M. Van Doormaal. *Numerical modelling of cardiovascular flows: from in vitro systems to animal models*. PhD thesis, Imperial College London, Department of Bioengineering, 2010.

M. A. Van Doormaal and C. R. Ethier. Design optimization of a helical endothelial cell culture device. *Biomech Model Mechanobiol*, 9(5):523–531, Oct 2010.

B. Vandeghinste, B. Trachet, M. Renard, C. Casteleyn, S. Staelens, B. Loeys, P. Segers, and S. Vandenberghe. Replacing vascular corrosion casting by in vivo micro-CT imaging for building 3D cardiovascular models in mice. *Mol Imaging Biol*, 13:78–86, 2011.

P. E. Vincent, S. J. Sherwin, and P. D. Weinberg. The effect of a spatially heterogeneous transmural water flux on concentration polarization of low density lipoprotein in arteries. *Biophys. J.*, 96:3102–3115, 2009.

P. E. Vincent, S. J. Sherwin, and P. D. Weinberg. The effect of the endothelial glycocalyx layer on concentration polarisation of low density lipoprotein in arteries. *J. Theor. Biol.*, 265:1–17, 2010.

P. E. Vincent, A. M. Plata, A. A. Hunt, P. D. Weinberg, and S. J. Sherwin. Blood flow in the rabbit aortic arch and descending thoracic aorta. *J R Soc Interface*, 2011.

P. Volino and N. Magnenat Thalmann. The SPHERIGON: A simple polygon patch for smoothing quickly your polygonal meshes. In *CA '98: Proceedings of the Computer Animation*, page 72, Washington, DC, USA, 1998. IEEE Computer Society.

G. E. von Rindfleisch. *A text-book of pathological histology: An introduction to the study of pathological anatomy*. Lindsay and Blakiston (Philadelphia), 1872.

T. Weiger, A. Lametschwandtner, and P. Stockmayer. Technical parameters of plastics (Mercox CL-2B and various methylmethacrylates) used in scanning

electron microscopy of vascular corrosion casts. *Scan Electron Microsc*, 1: 243–252, 1986.

P. D. Weinberg. Disease patterns at arterial branches and their relation to flow. *Biorheology*, 39:533–537, 2002.

P. D. Weinberg. Rate-limiting steps in the development of atherosclerosis: the response-to-influx theory. *J. Vasc. Res.*, 41:1–17, 2004.

P. D. Weinberg and C. R. Ethier. Twenty-fold difference in hemodynamic wall shear stress between murine and human aortas. *J Biomech*, 40:1594–1598, 2007.

J. J. Wentzel, E. Janssen, J. Vos, J. C. Schuurbiers, R. Krams, P. W. Serruys, P. J. de Feyter, and C. J. Slager. Extension of increased atherosclerotic wall thickness into high shear stress regions is associated with loss of compensatory remodeling. *Circulation*, 108:17–23, 2003.

J. J. Wentzel, F. J. Gijsen, J. C. Schuurbiers, R. Krams, P. W. Serruys, P. J. De Feyter, and C. J. Slager. Geometry guided data averaging enables the interpretation of shear stress related plaque development in human coronary arteries. *J Biomech*, 38:1551–1555, 2005.

S. A. Wesolowski, C. C. Fries, A. M. Sabini, and P. N. Sawyer. The significance of turbulence in hemic systems and in the distribution of the atherosclerotic lesion. *Surgery*, 57:155–162, 1965.

WHO. Cardiovascular diseases, fact sheet n° 317, 2011.

U. Windberger, A. Bartholovitsch, R. Plasenzotti, K. J. Korak, and G. Heinze. Whole blood viscosity, plasma viscosity and erythrocyte aggregation in nine mammalian species: reference values and comparison of data. *Exp. Physiol.*, 88(3):431–440, 2003.

J. R. Womersley. Method for the calculation of velocity, rate of flow and viscous

drag in arteries when the pressure gradient is known. *J. Physiol. (Lond.)*, 127: 553–563, 1955.

G. Xiong, C. A. Figueroa, N. Xiao, and C. A. Taylor. Simulation of blood flow in deformable vessels using subject-specific geometry and spatially varying wall properties. *Int j numer method biomed eng*, 27(7):1000–1016, 2011.

S. C. Yap, A. Nemes, F. J. Meijboom, T. W. Galema, M. L. Geleijnse, F. J. ten Cate, M. L. Simoons, and J. W. Roos-Hesselink. Abnormal aortic elastic properties in adults with congenital valvular aortic stenosis. *Int. J. Cardiol.*, 128:336–341, 2008.

C. K. Zarins, M. A. Zatina, D. P. Giddens, D. N. Ku, and S. Glagov. Shear stress regulation of artery lumen diameter in experimental atherogenesis. *J. Vasc. Surg.*, 5(3):413–420, Mar 1987.

C. M. Zeindler, R. G. Kratky, and M. R. Roach. Quantitative measurements of early atherosclerotic lesions on rabbit aortae from vascular casts. *Atherosclerosis*, 76:245–255, 1989.

C. Zhang, S. Xie, S. Li, F. Pu, X. Deng, Y. Fan, and D. Li. Flow patterns and wall shear stress distribution in human internal carotid arteries: the geometric effect on the risk for stenoses. *J Biomech*, 45(1):83–89, 2012.

S. Zhao, A. Suciu, T. Ziegler, J. E. Moore, E. Burki, J. J. Meister, and H. R. Brunner. Synergistic effects of fluid shear stress and cyclic circumferential stretch on vascular endothelial cell morphology and cytoskeleton. *Arterioscler. Thromb. Vasc. Biol.*, 15(10):1781–1786, 1995.

Y. Q. Zhou, S. N. Zhu, F. S. Foster, M. I. Cybulsky, and R. M. Henkelman. Aortic regurgitation dramatically alters the distribution of atherosclerotic lesions and enhances atherogenesis in mice. *Arterioscler. Thromb. Vasc. Biol.*, 30:1181–1188, 2010.

H. Zhu, J. Zhang, J. Shih, F. Lopez-Bertoni, J. R. Hagaman, N. Maeda, and M. H. Friedman. Differences in aortic arch geometry, hemodynamics, and

plaque patterns between C57BL/6 and 129/SvEv mice. *J Biomech Eng*, 131: 121005, 2009.

Appendix A

From Cartesian to Germano coordinates

A.1 Momentum balances

The unit vectors parallel to the axes of the Germano coordinate system (s, r, θ) are defined as:

$$\mathbf{a}_s = \mathbf{T}, \qquad \mathbf{a}_r = \cos(\theta+\phi)\mathbf{B} - \sin(\theta+\phi)\mathbf{N}, \qquad \mathbf{a}_\theta = -\sin(\theta+\phi)\mathbf{B} - \cos(\theta+\phi)\mathbf{N}.$$

Angles and axes are shown in figure 4.15. The continuity and Navier-Stokes equations (1.3)-(1.4) can be expressed in the Germano coordinate system as:

$$\frac{1}{h}\frac{\partial u}{\partial s} + \frac{\partial v}{\partial r} + \frac{1}{r}\frac{\partial w}{\partial \theta} + \frac{v}{r} + \frac{\kappa}{h}\left[v\sin(\theta+\phi) + w\cos(\theta+\phi)\right] = 0, \tag{A.1}$$

$$\mathrm{CA}_s = \mathrm{Co} + \mathrm{PG}_s + \mathrm{VF}_s, \tag{A.2}$$

$$\mathrm{CA}_r = \mathrm{CF}_r + \mathrm{PG}_r + \mathrm{VF}_r, \tag{A.3}$$

$$\mathrm{CA}_\theta = \mathrm{CF}_\theta + \mathrm{PG}_\theta + \mathrm{VF}_\theta, \tag{A.4}$$

where u, v and w represent the velocity components in the Germano coordinate directions, $h = 1 + r\kappa\sin(\theta+\phi)$ ($h\kappa^{-1}$ is the distance from the local centre of curvature C of the vessel centreline to the projection of the point into the plane

spanned by $\mathbf{T}$ and $\mathbf{N}$), and

$$\mathrm{CA}_s = \mathcal{D}u, \qquad \mathrm{Co} = -\frac{\kappa u}{h}\left[v\sin(\theta+\phi) + w\cos(\theta+\phi)\right], \qquad \mathrm{PG}_s = -\frac{1}{\rho h}\frac{\partial p}{\partial s},$$

$$\mathrm{VF}_s = \nu\left\{\frac{\partial^2 u}{\partial r^2} + \frac{1}{r^2}\frac{\partial^2 u}{\partial \theta^2} + \frac{1}{r}\frac{\partial u}{\partial r} + \frac{\kappa}{h}\left[\frac{\partial u}{\partial r} - \frac{u}{h}\frac{\partial h}{\partial r}\right]\sin(\theta+\phi)\right.$$
$$\left. + \frac{\kappa}{hr}\left[\frac{\partial u}{\partial \theta} - \frac{u}{h}\frac{\partial h}{\partial \theta}\right]\cos(\theta+\phi) + \frac{1}{h^2}\left[\frac{\partial h}{\partial r}\frac{\partial v}{\partial s} + \frac{1}{r}\frac{\partial h}{\partial \theta}\frac{\partial w}{\partial s}\right] - \frac{1}{h}\left[\frac{\partial^2 v}{\partial s \partial r} + \frac{1}{r}\frac{\partial v}{\partial s} + \frac{1}{r}\frac{\partial^2 w}{\partial s \partial \theta}\right]\right\},$$

$$\mathrm{CA}_r = \mathcal{D}v - \frac{w^2}{r}, \qquad \mathrm{CF}_r = \frac{\kappa}{h}u^2\sin(\theta+\phi), \qquad \mathrm{PG}_r = -\frac{1}{\rho}\frac{\partial p}{\partial r},$$

$$\mathrm{VF}_r = \nu\left\{\frac{1}{h^2}\left[\frac{\kappa u}{h}\frac{\partial h}{\partial s} - \frac{\mathrm{d}\kappa}{\mathrm{d}s}u - \kappa\frac{\partial u}{\partial s}\right]\sin(\theta+\phi) + \frac{\tau\kappa}{h^2}u\cos(\theta+\phi)\right.$$
$$-\frac{\kappa}{h}\left[\frac{\partial w}{\partial r} + \frac{w}{r} - \frac{1}{r}\frac{\partial v}{\partial \theta}\right]\cos(\theta+\phi) - \frac{1}{h}\left[\frac{\partial^2 u}{\partial r \partial s} - \frac{1}{h}\frac{\partial^2 v}{\partial s^2} + \frac{1}{h^2}\frac{\partial h}{\partial s}\frac{\partial v}{\partial s}\right]$$
$$\left. -\frac{1}{r}\left[\frac{\partial^2 w}{\partial r \partial \theta} + \frac{1}{r}\frac{\partial w}{\partial \theta} - \frac{1}{r}\frac{\partial^2 v}{\partial \theta^2}\right]\right\},$$

$$\mathrm{CA}_\theta = \mathcal{D}w + \frac{vw}{r}, \qquad \mathrm{CF}_\theta = \frac{\kappa}{h}u^2\cos(\theta+\phi), \qquad \mathrm{PG}_\theta = -\frac{1}{\rho r}\frac{\partial p}{\partial \theta},$$

$$\mathrm{VF}_\theta = \nu\left\{\frac{1}{h^2}\left[\frac{\kappa u}{h}\frac{\partial h}{\partial s} - \frac{\mathrm{d}\kappa}{\mathrm{d}s}u - \kappa\frac{\partial u}{\partial s}\right]\cos(\theta+\phi) - \frac{\tau\kappa}{h^2}u\sin(\theta+\phi)\right.$$
$$+\frac{\kappa}{h}\left[\frac{\partial w}{\partial r} + \frac{w}{r} - \frac{1}{r}\frac{\partial v}{\partial \theta}\right]\sin(\theta+\phi) - \frac{1}{h}\left[\frac{1}{r}\frac{\partial^2 u}{\partial \theta \partial s} - \frac{1}{h}\frac{\partial^2 w}{\partial s^2} + \frac{1}{h^2}\frac{\partial h}{\partial s}\frac{\partial w}{\partial s}\right]$$
$$\left. -\frac{1}{r}\left[\frac{\partial^2 v}{\partial r \partial \theta} - \frac{1}{r}\frac{\partial v}{\partial \theta} - \frac{\partial w}{\partial r} + \frac{w}{r}\right] + \frac{\partial^2 w}{\partial r^2}\right\},$$

and

$$\mathcal{D} = \frac{u}{h}\frac{\partial}{\partial s} + v\frac{\partial}{\partial r} + \frac{w}{r}\frac{\partial}{\partial \theta}.$$

Since $\mathbf{a}_s = \mathbf{T}$ (equation (A.1)), equations (A.2) and (4.18) are equivalent. The centrifugal and torsional forces are obtained by projecting the quantities appearing in equations (A.3)-(A.4) onto $\mathbf{N}$ and $\mathbf{B}$. This results in the following set of expressions:

$$\mathrm{CA}_N = \frac{u}{h}\left(\frac{\partial V_N}{\partial s} - \tau V_B\right) + V_N\frac{\partial V_N}{\partial n} + V_B\frac{\partial V_N}{\partial b}, \tag{A.5}$$

$$\mathrm{CA}_B = \frac{u}{h}\left(\frac{\partial V_B}{\partial s} + \tau V_N\right) + V_B\frac{\partial V_B}{\partial b} + V_N\frac{\partial V_B}{\partial n}, \tag{A.6}$$

$$\mathrm{CF}_N = -\frac{\kappa u^2}{h}, \quad \mathrm{CF}_B = 0, \tag{A.7}$$

$$\mathrm{PG}_N = -\frac{1}{\rho}\frac{\partial p}{\partial n}, \quad \mathrm{PG}_B = -\frac{1}{\rho}\frac{\partial p}{\partial b}, \tag{A.8}$$

Definition of the local torsional force components as:

$$\mathrm{TF}_N = \frac{\tau u}{h} V_B, \quad \mathrm{TF}_B = -\frac{\tau u}{h} V_N, \tag{A.9}$$

leads to the modified convective accelerations CA'_N and CA'_B:

$$\mathrm{CA}'_N = \frac{u}{h}\frac{\partial V_N}{\partial s} + V_N\frac{\partial V_N}{\partial n} + V_B\frac{\partial V_N}{\partial b}, \tag{A.10}$$

$$\mathrm{CA}'_B = \frac{u}{h}\frac{\partial V_B}{\partial s} + V_B\frac{\partial V_B}{\partial b} + V_N\frac{\partial V_B}{\partial n}, \tag{A.11}$$

and eventually results in equations (4.19)-(4.20).

A.2 Velocity and pressure gradients

Given the velocity vector $\tilde{\mathbf{V}} = (\tilde{u}, \tilde{v}, \tilde{w})$ in Cartesian coordinates (x, y, z), $\mathbf{V} = (u, v, w)$ can be determined by projection onto the directions $\mathbf{a}_s$, $\mathbf{a}_r$ and $\mathbf{a}_\theta$. Using the Frenet-Serret formulae (Frenet, 1852; Serret, 1851) the following expressions can be obtained for the first partial derivatives of u, v, w in Germano coordinates from the corresponding derivatives in Cartesian coordinates:

$$\frac{\partial u}{\partial s} = \frac{\partial \tilde{\mathbf{V}}}{\partial s}\cdot\mathbf{T} + \kappa\tilde{\mathbf{V}}\cdot\mathbf{N}, \qquad \frac{\partial u}{\partial r} = \frac{\partial \tilde{\mathbf{V}}}{\partial r}\cdot\mathbf{T}, \qquad \frac{\partial u}{\partial \theta} = \frac{\partial \tilde{\mathbf{V}}}{\partial \theta}\cdot\mathbf{T},$$

$$\frac{\partial v}{\partial s} = \frac{\partial \tilde{\mathbf{V}}}{\partial s}\cdot\mathbf{a}_r + \kappa\sin(\theta+\phi)\tilde{\mathbf{V}}\cdot\mathbf{T}, \qquad \frac{\partial v}{\partial r} = \frac{\partial \tilde{\mathbf{V}}}{\partial r}\cdot\mathbf{a}_r, \qquad \frac{\partial v}{\partial \theta} = \frac{\partial \tilde{\mathbf{V}}}{\partial \theta}\cdot\mathbf{a}_r + \tilde{\mathbf{V}}\cdot\mathbf{a}_\theta,$$

$$\frac{\partial w}{\partial s} = \frac{\partial \tilde{\mathbf{V}}}{\partial s}\cdot\mathbf{a}_\theta + \kappa\cos(\theta+\phi)\tilde{\mathbf{V}}\cdot\mathbf{T}, \qquad \frac{\partial w}{\partial r} = \frac{\partial \tilde{\mathbf{V}}}{\partial r}\cdot\mathbf{a}_\theta, \qquad \frac{\partial w}{\partial \theta} = \frac{\partial \tilde{\mathbf{V}}}{\partial \theta}\cdot\mathbf{a}_\theta - \tilde{\mathbf{V}}\cdot\mathbf{a}_r,$$

where $\frac{\partial \tilde{\mathbf{V}}}{\partial s}$, $\frac{\partial \tilde{\mathbf{V}}}{\partial r}$ and $\frac{\partial \tilde{\mathbf{V}}}{\partial \theta}$ are related to the Cartesian partial derivatives of $\tilde{u}$, $\tilde{v}$ and $\tilde{w}$ through the chain rule; i.e.

$$\frac{\partial \tilde{\mathbf{V}}}{\partial s} = \mathbf{J}\frac{\partial \mathbf{x}}{\partial s}, \qquad \frac{\partial \tilde{\mathbf{V}}}{\partial r} = \mathbf{J}\frac{\partial \mathbf{x}}{\partial r}, \qquad \frac{\partial \tilde{\mathbf{V}}}{\partial \theta} = \mathbf{J}\frac{\partial \mathbf{x}}{\partial \theta},$$

with

$$\frac{\partial \mathbf{x}}{\partial s} = h\mathbf{T}, \qquad \frac{\partial \mathbf{x}}{\partial r} = \mathbf{a}_r, \qquad \frac{\partial \mathbf{x}}{\partial \theta} = r\mathbf{a}_\theta, \qquad \mathbf{J} = \begin{bmatrix} \frac{\partial \tilde{u}}{\partial x} & \frac{\partial \tilde{u}}{\partial y} & \frac{\partial \tilde{u}}{\partial z} \\ \frac{\partial \tilde{v}}{\partial x} & \frac{\partial \tilde{v}}{\partial y} & \frac{\partial \tilde{v}}{\partial z} \\ \frac{\partial \tilde{w}}{\partial x} & \frac{\partial \tilde{w}}{\partial y} & \frac{\partial \tilde{w}}{\partial z} \end{bmatrix} = \begin{bmatrix} \mathbf{J}_{\tilde{\mathbf{u}}} \\ \mathbf{J}_{\tilde{\mathbf{v}}} \\ \mathbf{J}_{\tilde{\mathbf{w}}} \end{bmatrix}. \tag{A.12}$$

The second partial derivatives take the form

$$\frac{\partial^2 u}{\partial s^2} = \frac{\partial^2 \tilde{\mathbf{V}}}{\partial s^2} \cdot \mathbf{T} + 2\kappa \frac{\partial \tilde{\mathbf{V}}}{\partial s} \cdot \mathbf{N} + \kappa \tilde{\mathbf{V}} \cdot (\tau \mathbf{B} - \kappa \mathbf{T}) + \frac{\mathrm{d}\kappa}{\mathrm{d}s} \tilde{\mathbf{V}} \cdot \mathbf{N},$$

$$\frac{\partial^2 u}{\partial r^2} = \frac{\partial^2 \tilde{\mathbf{V}}}{\partial r^2} \cdot \mathbf{T}, \qquad \frac{\partial^2 u}{\partial \theta^2} = \frac{\partial^2 \tilde{\mathbf{V}}}{\partial \theta^2} \cdot \mathbf{T},$$

$$\frac{\partial^2 u}{\partial s \partial r} = \frac{\partial^2 \tilde{\mathbf{V}}}{\partial s \partial r} \cdot \mathbf{T} + \kappa \frac{\partial \tilde{\mathbf{V}}}{\partial r} \cdot \mathbf{N}, \qquad \frac{\partial^2 u}{\partial r \partial \theta} = \frac{\partial^2 \tilde{\mathbf{V}}}{\partial r \partial \theta} \cdot \mathbf{T},$$

$$\frac{\partial^2 u}{\partial \theta \partial s} = \frac{\partial^2 \tilde{\mathbf{V}}}{\partial \theta \partial s} \cdot \mathbf{T} + \kappa \frac{\partial \tilde{\mathbf{V}}}{\partial \theta} \cdot \mathbf{N},$$

$$\frac{\partial^2 v}{\partial s^2} = \frac{\partial^2 \tilde{\mathbf{V}}}{\partial s^2} \cdot \mathbf{a}_r + 2\kappa \sin(\theta + \phi) \frac{\partial \tilde{\mathbf{V}}}{\partial s} \cdot \mathbf{T} + \left[\frac{\mathrm{d}\kappa}{\mathrm{d}s} \sin(\theta + \phi) - \tau\kappa \cos(\theta + \phi) \right] \tilde{\mathbf{V}} \cdot \mathbf{T} + \kappa^2 \sin(\theta + \phi) \tilde{\mathbf{V}} \cdot \mathbf{N},$$

$$\frac{\partial^2 v}{\partial r^2} = \frac{\partial^2 \tilde{\mathbf{V}}}{\partial r^2} \cdot \mathbf{a}_r, \qquad \frac{\partial^2 v}{\partial \theta^2} = \frac{\partial^2 \tilde{\mathbf{V}}}{\partial \theta^2} \cdot \mathbf{a}_r + 2\frac{\partial \tilde{\mathbf{V}}}{\partial \theta} \cdot \mathbf{a}_\theta - \tilde{\mathbf{V}} \cdot \mathbf{a}_r,$$

$$\frac{\partial^2 v}{\partial s \partial r} = \frac{\partial^2 \tilde{\mathbf{V}}}{\partial s \partial r} \cdot \mathbf{a}_r + \kappa \sin(\theta + \phi) \frac{\partial \tilde{\mathbf{V}}}{\partial r} \cdot \mathbf{T}, \quad \frac{\partial^2 v}{\partial r \partial \theta} = \frac{\partial^2 \tilde{\mathbf{V}}}{\partial r \partial \theta} \cdot \mathbf{a}_r + \frac{\partial \tilde{\mathbf{V}}}{\partial r} \cdot \mathbf{a}_\theta,$$

$$\frac{\partial^2 v}{\partial \theta \partial s} = \frac{\partial^2 \tilde{\mathbf{V}}}{\partial \theta \partial s} \cdot \mathbf{a}_r + \frac{\partial \tilde{\mathbf{V}}}{\partial s} \cdot \mathbf{a}_\theta + \kappa \left[\cos(\theta + \phi) \tilde{\mathbf{V}} + \sin(\theta + \phi) \frac{\partial \tilde{\mathbf{V}}}{\partial \theta} \right] \cdot \mathbf{T},$$

$$\frac{\partial^2 w}{\partial s^2} = \frac{\partial^2 \tilde{\mathbf{V}}}{\partial s^2} \cdot \mathbf{a}_\theta + 2\kappa \cos(\theta + \phi) \frac{\partial \tilde{\mathbf{V}}}{\partial s} \cdot \mathbf{T} + \left[\frac{\mathrm{d}\kappa}{\mathrm{d}s} \cos(\theta + \phi) + \tau\kappa \sin(\theta + \phi) \right] \tilde{\mathbf{V}} \cdot \mathbf{T} + \kappa^2 \cos(\theta + \phi) \tilde{\mathbf{V}} \cdot \mathbf{N},$$

$$\frac{\partial^2 w}{\partial r^2} = \frac{\partial^2 \tilde{\mathbf{V}}}{\partial r^2} \cdot \mathbf{a}_\theta, \qquad \frac{\partial^2 w}{\partial \theta^2} = \frac{\partial^2 \tilde{\mathbf{V}}}{\partial \theta^2} \cdot \mathbf{a}_\theta - 2\frac{\partial \tilde{\mathbf{V}}}{\partial \theta} \cdot \mathbf{a}_r - \tilde{\mathbf{V}} \cdot \mathbf{a}_\theta,$$

$$\frac{\partial^2 w}{\partial s \partial r} = \frac{\partial^2 \tilde{\mathbf{V}}}{\partial s \partial r} \cdot \mathbf{a}_\theta + \kappa \cos(\theta + \phi) \frac{\partial \tilde{\mathbf{V}}}{\partial r} \cdot \mathbf{T}, \qquad \frac{\partial^2 w}{\partial r \partial \theta} = \frac{\partial^2 \tilde{\mathbf{V}}}{\partial r \partial \theta} \cdot \mathbf{a}_\theta - \frac{\partial \tilde{\mathbf{V}}}{\partial r} \cdot \mathbf{a}_r,$$

$$\frac{\partial^2 w}{\partial \theta \partial s} = \frac{\partial^2 \tilde{\mathbf{V}}}{\partial \theta \partial s} \cdot \mathbf{a}_\theta - \frac{\partial \tilde{\mathbf{V}}}{\partial s} \cdot \mathbf{a}_r + \kappa \left[-\sin(\theta + \phi) \tilde{\mathbf{V}} + \cos(\theta + \phi) \frac{\partial \tilde{\mathbf{V}}}{\partial \theta} \right] \cdot \mathbf{T},$$

where the second partial derivatives of $\tilde{\mathbf{V}}$ in local coordinates are related to the Cartesian first and second partial derivatives of $\tilde{u}$, $\tilde{v}$ and $\tilde{w}$ through the chain rule;

i.e.

$$\frac{\partial^2 \tilde{u}}{\partial i \partial j} = \left[\frac{\partial \mathbf{x}}{\partial i}\right]^{\mathrm{T}} \mathbf{H}_{\tilde{u}} \frac{\partial \mathbf{x}}{\partial j} + \mathbf{J}_{\tilde{\mathbf{u}}} \frac{\partial^2 \mathbf{x}}{\partial i \partial j}, \qquad \frac{\partial^2 \tilde{v}}{\partial i \partial j} = \left[\frac{\partial \mathbf{x}}{\partial i}\right]^{\mathrm{T}} \mathbf{H}_{\tilde{v}} \frac{\partial \mathbf{x}}{\partial j} + \mathbf{J}_{\tilde{\mathbf{v}}} \frac{\partial^2 \mathbf{x}}{\partial i \partial j},$$

$$\frac{\partial^2 \tilde{w}}{\partial i \partial j} = \left[\frac{\partial \mathbf{x}}{\partial i}\right]^{\mathrm{T}} \mathbf{H}_{\tilde{w}} \frac{\partial \mathbf{x}}{\partial j} + \mathbf{J}_{\tilde{\mathbf{w}}} \frac{\partial^2 \mathbf{x}}{\partial i \partial j}, \qquad i, j = s, r, \theta,$$

with

$$\frac{\partial^2 \mathbf{x}}{\partial s^2} = \left[\frac{\mathrm{d}\kappa}{\mathrm{d}s} r \sin(\theta + \phi) - \tau\kappa r \cos(\theta + \phi)\right] \mathbf{T} + h\kappa \mathbf{N}, \qquad \frac{\partial^2 \mathbf{x}}{\partial r^2} = \mathbf{0}, \qquad \frac{\partial^2 \mathbf{x}}{\partial \theta^2} = -r\mathbf{a}_r,$$

$$\frac{\partial^2 \mathbf{x}}{\partial s \partial r} = \kappa \sin(\theta + \phi)\mathbf{T}, \qquad \frac{\partial^2 \mathbf{x}}{\partial r \partial \theta} = \mathbf{a}_\theta, \qquad \frac{\partial^2 \mathbf{x}}{\partial \theta \partial s} = \kappa r \cos(\theta + \phi)\mathbf{T},$$

$$\mathbf{H}_{\tilde{u}} = \begin{bmatrix} \frac{\partial^2 \tilde{u}}{\partial x^2} & \frac{\partial^2 \tilde{u}}{\partial x \partial y} & \frac{\partial^2 \tilde{u}}{\partial x \partial z} \\ \frac{\partial^2 \tilde{u}}{\partial y \partial x} & \frac{\partial^2 \tilde{u}}{\partial y^2} & \frac{\partial^2 \tilde{u}}{\partial y \partial z} \\ \frac{\partial^2 \tilde{u}}{\partial z \partial x} & \frac{\partial^2 \tilde{u}}{\partial z \partial y} & \frac{\partial^2 \tilde{u}}{\partial z^2} \end{bmatrix}, \quad \mathbf{H}_{\tilde{v}} = \begin{bmatrix} \frac{\partial^2 \tilde{v}}{\partial x^2} & \frac{\partial^2 \tilde{v}}{\partial x \partial y} & \frac{\partial^2 \tilde{v}}{\partial x \partial z} \\ \frac{\partial^2 \tilde{v}}{\partial y \partial x} & \frac{\partial^2 \tilde{v}}{\partial y^2} & \frac{\partial^2 \tilde{v}}{\partial y \partial z} \\ \frac{\partial^2 \tilde{v}}{\partial z \partial x} & \frac{\partial^2 \tilde{v}}{\partial z \partial y} & \frac{\partial^2 \tilde{v}}{\partial z^2} \end{bmatrix},$$

$$\mathbf{H}_{\tilde{w}} = \begin{bmatrix} \frac{\partial^2 \tilde{w}}{\partial x^2} & \frac{\partial^2 \tilde{w}}{\partial x \partial y} & \frac{\partial^2 \tilde{w}}{\partial x \partial z} \\ \frac{\partial^2 \tilde{w}}{\partial y \partial x} & \frac{\partial^2 \tilde{w}}{\partial y^2} & \frac{\partial^2 \tilde{w}}{\partial y \partial z} \\ \frac{\partial^2 \tilde{w}}{\partial z \partial x} & \frac{\partial^2 \tilde{w}}{\partial z \partial y} & \frac{\partial^2 \tilde{w}}{\partial z^2} \end{bmatrix},$$

and $\mathbf{J}_{\tilde{\mathbf{u}}}$, $\mathbf{J}_{\tilde{\mathbf{v}}}$ and $\mathbf{J}_{\tilde{\mathbf{w}}}$ as defined in equation (A.12).

Given the Cartesian pressure gradient $\boldsymbol{\nabla} p = \left(\frac{\partial p}{\partial x}, \frac{\partial p}{\partial y}, \frac{\partial p}{\partial z}\right)$ and using the chain rule, the components of the pressure gradient in local coordinates can be calculated as

$$\frac{\partial p}{\partial s} = \boldsymbol{\nabla} p \cdot \frac{\partial \mathbf{x}}{\partial s}, \qquad \frac{\partial p}{\partial r} = \boldsymbol{\nabla} p \cdot \frac{\partial \mathbf{x}}{\partial r}, \qquad \frac{\partial p}{\partial \theta} = \boldsymbol{\nabla} p \cdot \frac{\partial \mathbf{x}}{\partial \theta},$$

with $\frac{\partial \mathbf{x}}{\partial s}$, $\frac{\partial \mathbf{x}}{\partial r}$ and $\frac{\partial \mathbf{x}}{\partial \theta}$ given by equation (A.12).

Appendix B

Publications

Parts of the work presented here have been presented previously, in written or in oral form. An overview is provided here.

B.1 Journal articles

Effect of aortic taper on patterns of blood flow and wall shear stress in rabbits: association with age

V. Peiffer, E. M. Rowland, S. G. Cremers, P. D. Weinberg, S. J. Sherwin

Atherosclerosis, 223/1:114-121 (2012)

Reducing the data: Analysis of the role of vascular geometry on blood flow patterns in curved vessels

J. Alastruey, J. H. Siggers, V. Peiffer, D. J. Doorly, S. J. Sherwin

Physics of Fluids, 24:031902 (2012)

B.2 Conference contributions

The presenting author is denoted by an asterik.

Characterisation of multi-directional flow

V. Peiffer*, P. D. Weinberg, S. J. Sherwin

Oral presentation. Bioengineering 12, 6-7 September 2012, Said Business School, Oxford, United Kingdom

The wall shear stress vector: methods for characterising truly disturbed flow

V. Peiffer*, P. D. Weinberg, S. J. Sherwin

Oral presentation. ASME 2012 Summer Bioengineering Conference, 20 - 23 June 2012, Fajardo, Puerto Rico, U.S.A.

Age-related differences in haemodynamics of the rabbit aorta and comparison with average maps of atherosclerotic lesion prevalence

V. Peiffer*, E. M. Rowland, S. G. Cremers, P. D. Weinberg, S. J. Sherwin

Oral presentation. ASME 2012 Summer Bioengineering Conference, 20 - 23 June 2012, Fajardo, Puerto Rico, U.S.A.

CFD Challenge: Solutions using an in-house spectral element solver, Nεκταr

V. Peiffer*, S. J. Sherwin

Oral presentation. ASME 2012 Summer Bioengineering Conference, 20 - 23 June 2012, Fajardo, Puerto Rico, U.S.A.

Wall shear stress and atherosclerosis: Age-related variations in a study of rabbit aortas

V. Peiffer, P. D. Weinberg, S. J. Sherwin*

Oral presentation. Computational Fluid Dynamics (CFD) in Medicine and Biology in conjunction with the 7$^{\text{th}}$ International Biofluid Mechanics Symposium, 25-30 March 2012, Dead Sea, Israel

Reducing the data: Analysis of the role of vascular geometry on blood flow patterns in curved vessels

J. Alastruey*, J. H. Siggers, V. Peiffer, D. J. Doorly, S. J. Sherwin

Poster presentation. Computational Fluid Dynamics (CFD) in Medicine and Biology in conjunction with the 7$^{\text{th}}$ International Biofluid Mechanics Symposium, 25-30

March 2012, Dead Sea, Israel

Arterial blood flow and macromolecular transport phenomena across scales

P. D. Weinberg*, V. Peiffer, S. J. Sherwin

Oral presentation. Multiscale Methods and Validation in Medicine and Biology I: Biomechanics and Mechanobiology (USACM), 13-14 February 2012, San Fransico, California, U.S.A.

Effect of aortic taper on blood flow and wall shear stress in rabbits: association with age

V. Peiffer*, E. M. Rowland, S. G. Cremers, P. D. Weinberg, S. J. Sherwin

Poster presentation. 5th Cardiovascular Technology Network Symposium, 8 February 2012, London, United Kingdom

Age-related changes in geometry and blood flow in the rabbit aorta

V. Peiffer*, M. Rowland, P. D. Weinberg, S. J. Sherwin

Poster presentation. Bioengineering 11, 12-13 September 2011, Queen Mary, University of London, United Kingdom

Reducing the data: Analysis of the role of vascular geometry on blood flow patterns in curved vessels

J. Alastruey*, J. H. Siggers, V. Peiffer, D. J. Doorly, S. J. Sherwin

Oral presentation. Bioengineering 11, 12-13 September 2011, Queen Mary, University of London, United Kingdom

Comparison of flow features in an immature and a mature rabbit aorta

V. Peiffer*, A. M. Plata, P. E. Vincent, P. D. Weinberg, S. J. Sherwin

Oral presentation. Physiological Fluid Mechanics Conference, 14-15 July 2011, Brunel University, United Kingdom

Haemodynamic study of the rabbit aorta

V. Peiffer*, P. D. Weinberg, S. J. Sherwin

Oral presentation. International Society of Biomechanics 2011, 3-7 July 2011, Brussels, Belgium

Database of rabbit aortic geometries for use in computational flow studies

V. Peiffer*, M. Rowland, P. D. Weinberg, S. J. Sherwin

Oral presentation. ASME 2011 Summer Bioengineering Conference, 22 - 25 June 2011, Farmington, Pennsylvania, U.S.A.

Unraveling atherosclerosis: Characteristics of steady and pulsatile blood flow in the immature rabbit aorta

V. Peiffer*, P. D. Weinberg, S. J. Sherwin

Oral presentation. Transnational Access Meeting 2011, 8 - 9 June 2011, Barcelona, Spain

Arterial blood flow and macromolecular transport phenomena at the microscale

P. D. Weinberg*, V. Peiffer, S. J. Sherwin

Oral presentation. Workshop on Microscale Modeling in Biomechanics and Mechanobiology, 30 May - 1 June 2011, Ericeira, Portugal

Understanding flow features in an immature rabbit aorta

V. Peiffer*, P. D. Weinberg, S. J. Sherwin

Oral presentation. 23rd International Conference on Parallel Computational Fluid Dynamics 2011, 16 - 20 May 2011, Barcelona, Spain

Aortic geometry and haemodynamics in immature and mature rabbits

V. Peiffer*, M. Rowland, A. M. Plata, P. D. Weinberg, S. J. Sherwin

Oral presentation. BHF Centre of Research Excellence Postgraduate Student Symposium in Cardiovascular Research 2011, 7 April 2011, Imperial College London, United Kingdom

Geometric characterisation of immature and mature rabbit aortas for use in haemodynamic studies

V. Peiffer*, P. D. Weinberg, S. J. Sherwin

Poster presentation. BHF Mid-Term Review, 22 March 2011, Imperial College London, United Kingdom

High-fidelity representation of immature and mature rabbit aortas

V. Peiffer*, P. D. Weinberg, S. J. Sherwin

Oral presentation. Medical Physics and Engineering Conference/Bioengineering 10, 14-16 September 2010, Nottingham, United Kingdom

In silico reconstruction of the rabbit aorta: anatomical variability

V. Peiffer*, P. D. Weinberg, S. J. Sherwin

Poster presentation. 4^{th} Cardiovascular Technology Network Symposium, 8 July 2010, London, United Kingdom